X-ray Observations of Pulsar Wind Nebulae: The nature of pulsar winds and their environment

by

Benson Thomas Guest

A Thesis submitted to the Faculty of Graduate Studies of
The University of Manitoba
in partial fulfilment of the requirements of the degree of

Doctor of Philosophy

Department of Physics and Astronomy
University of Manitoba
Winnipeg

Abstract

Pulsar wind nebulae (PWNe) are non-thermal bubbles blown by the relativistic winds of rapidly rotating neutron stars. They are formed in the cavity evacuated by the explosion of a core collapse supernova, and depending on their evolutionary stage may appear as a region of hard X-ray emission within a shell of million degree gas, or be the only visible remains of the cataclysmic event. With deep observations and spatially resolved X-ray spectroscopy, we probe the environment surrounding PWNe of different ages to search for the missing emission predicted from shock heated gas. We examine the properties of the relativistic winds and compare our results with diffusion models and hydrodynamic simulations. In the process of creating consistent spectral maps of PWNe we discover variability in archival *Chandra* data, opening a new window for observations and theory to explore. We present the deepest *Chandra* study of G21.5–0.9, finding faint thermal emission embedded in the primarily non-thermal limb-brightened shell. In analysing the synchrotron emission from the PWN, we find an adequate fit with a spatially averaged diffusion model to describe the transport of the wind through the nebula. Unlike the limb-brightened shell previously revealed in G21.5–0.9 with sufficient observation time, the missing shell in CTB 87 remains hidden despite a deep *XMM-Newton* observation. We constrain the ambient density and favour expansion into a low density bubble. We attribute the morphology to an interaction of the wind

with a reverse shock due to the motion of the pulsar within a $\sim$ 20 kyr old remnant. We present the first X-ray spectral map of this remnant, and find a good agreement with a simulated map. While merging or simultaneously fitting observations separated by extended periods of time will improve statistics, it may also hide unknown variability. We discover significant spectral variability in G21.5–0.9, 3C58, and Kes 75, and marginal evidence of variability in G11.2-0.3 and G54.1+0.3 to be confirmed with future observations.

Acknowledgments

I acknowledge financial support for this research provided by a University of Manitoba Graduate Fellowship (UMGF), and through my advisor from the Natural Science and Engineering Research Council of Canada (NSERC) Discovery Grants and Canada Research Chair programs, and the Canadian Space Agency.

Throughout the course of this study I have benefited immensely from the support of those around me. Dr. Samar Safi-Harb provided encouragement, guidance, and patience which helped me grow as a researcher and an individual. Maiko Langelaar was enthusiastic in providing exceptional computer support. The Department of Physics and Astronomy office staff were incredibly helpful, especially Susan Beshta who always advocated on my behalf. My journey began long before I started my graduate studies. I owe a great deal to my undergraduate colleagues for helping me with coursework and concepts when outlooks were less than bleak. Later, they encouraged me to apply for a summer research position which led to the opportunity of working with Dr. Andreas Shalchi and my first experience with the research world. Thank you to all of my colleagues for enriching the university experience outside of research. Ian Cameron and Danielle Pahud introduced me to teaching and public outreach through the various astronomy labs and astronomy open houses. Michael Harder encouraged me to expand my horizons of outreach through creative demos which led to the eventual creation of our physics show. Chelsea

Braun and Erica Franzmann among others provided outlets from stress through enlightening conversations, walks for coffee, and proving that I was not alone in my uselessness. Kelvin Au put up with the encroachment of my office plants and showed me the wrong way to jump in a lake when we acted as the astronomy guides for a Nature Manitoba canoe trip. Thank you to all my friends who didn't let me disappear into my work and showed great interest whenever I explained a new project I had started.

Most of all, I need to thank my girlfriend Stephanie Allec who lightened even the most stressful moments, and my parents. It is impossible to express everything my parents have done for me. Their unwavering love and support helped me to grow to the man I am today. My Mom offered constant encouragement and was always supportive of my choice in direction. My Dad once told me he didnt know what he wanted to do, so he stayed in school as long as possible. I continue to follow in his footsteps.

For my parents

Contents

List of Tables

List of Figures

List of Abbreviations

ACIS	Advanced CCD Imaging Spectrometer
ARF	Auxiliary Response File
CCD	Charge-Coupled Device
CIAO	Chandra Interactive Analysis of Observations
CSA	Canadian Space Agency
CSM	Circumstellar Medium
CTB	California Institute of Technology List B (Catalogue of Radio Sources)
Dec	Declination
EPIC	European Photon Imaging Camera
ESA	European Space Agency
FITS	Flexible Image Transport System
HRC	High Resolution Camera
ISM	Interstellar Medium

JAXA Japan Aerospace Exploration Agency

KC84 Kennel & Coroniti (1984a,b)

Kes Kesteven (Catalogue of SNRs)

MCP Micro-Channel Plate

MHD Magnetohydrodynamics

MOS Metal Oxide Semiconductor

MSH Mills, Slee, Hill (Catalogue of Radio Sources)

NASA National Aeronautics and Space Administration

ObsID Observation Identification Number

PL Power-law

PSF Point Spread Function

PWN(e) Pulsar Wind Nebula(e)

RA Right Ascension

RMF Redistribution Matrix File

SAS Science Analysis System

SNR(s) Supernova Remnant(s)

TBABS Tuebingen-Boulder ISM Absorption model

Preface

Statement of Originality

This thesis contains work which has, or will be published in the following refereed journals.

Chapter 6 Guest, B., Safi-Harb, S., & Tang, X., *The Deepest Chandra Study of the Plerionic Supernova Remnant G21.5–0.9*, Monthly Notices of the Royal Astronomical Society, 842, 1, 2019.

Chapter 7 Guest, B., Safi-Harb, S., MacMaster, A., Kothes, R., Olmi, B., Amato, E., Bucciantini, N., & Arzoumanian, Z., *Deciphering the Nature of the Pulsar Wind Nebula CTB 87 with XMM-Newton*, Monthly Notices of the Royal Astronomical Society, 491, 2, 2020.

Chapter 8 Guest, B., & Safi-Harb, S., *Revealing Hidden Structure and Variability in PWNe with Photon Index Maps*, Monthly Notices of the Royal Astronomical Society. Under Revision.

I am a co-author on the following papers and provided comments on the manuscripts in addition to the contributions listed below

- Kothes, R., Reich, W., Safi-Harb, S., Guest, B., Reich, P., & Fürst, E. Submitted to MNRAS. A companion radio paper to the X-ray study of CTB 87 presented in Chapter 7. I contributed the X-ray map for correlation studies with radio.
- The Hitomi paper on G21.5-0.9 summarised in Section 9.1. I provided the *Chandra* model for the Hitomi broadband spectroscopy.
- The AXIS (Section 9.4.1) white paper on PWNe (Safi-Harb et al. (2019). I contributed simulations of PWNe with AXIS.

The results presented in this thesis have been presented at conferences including Sant Cugat Forum on Astrophysics in Spain 2016, Hitomi Science meeting at Goddard Space Flight Center in Greenbelt Maryland USA 2016, CASCA 2016 & 2018 in Winnipeg MB and Victoria BC Canada respectively, and Supernova Remnants II: An odyssey after stellar death in Chania Crete Greece 2019.

Contribution of Authors

Here I acknowledge the contributions of others which benefited immensely the manuscripts included in this thesis. Unless otherwise specified, the papers

included were written by myself with valuable editing, input, and guidance from my supervisor Samar Safi-Harb. She provided leadership for the teams collaborating on the publications listed below. All coauthors provided comments on the manuscripts.

Chapter 6

The X-ray processing and analysis was performed by myself with the software provided by the operating centre of the *Chandra X-ray Observatory*, and guidance from Samar Safi-Harb. Xiaping Tang provided the diffusion modelling and written discussion in section 6.5.2.

Chapter 7

Samar Safi-Harb is the principal investigator for the XMM-Newton Observation used in this analysis. The X-ray processing and fitting was performed by myself with assistance from Austin MacMaster in fitting the pulsar and PWN spectra listed in Table 7.1. The processing used the software provided by the operating centre of *XMM-Newton*. The contours in Figure 7.7 were generated from radio data provided by Roland Kothes who collaborates on the companion radio study. The numerical simulations and written discussion in Section 7.6 were provided by Barbara Olmi in collaboration with Elena Amoto & Niccolo Bucciantini. Zaven Arzoumanian provided comments on the manuscript and is a collaborator on planning future timing studies of the pulsar candidate.

Chapter 8

The X-ray Observations used in this analysis (Table 8.1) were obtained from the Chandra Data Archive[1].

[1] http://cxc.cfa.harvard.edu/cda/

Chapter 1

Introduction

A core-collapse supernova marks the end of the nuclear burning phase of a massive star's life. By this point, the star has built up an onion like structure where different elements are fused to release the energy required to support against the relentless pull of gravity. The fusion reactions progress through heavier elements until iron is produced in the core of the star. Once iron is formed, no further fusion reactions may occur to produce the necessary energy to continue to balance the inward pressure. The core begins to collapse forcing protons and electrons together to create neutrons and neutrinos. For a core mass of ~ 1.5 $M_\odot$ the collapse is halted by neutron degeneracy pressure. The precise limits for allowable core masses is unknown due to the incomplete knowledge of their equation of state, yet masses of $\sim 1 - 2$ $M_\odot$ have been measured (Özel & Freire (2016)). The outer layers of the star "bounce" off of the suddenly rigid core and drive the explosion. The core survives as a neutron star: a dense ball of neutrons spun up by conservation of angular momentum

and containing a strong magnetic field (Longair (2011)).

Neutron stars have been discovered at radio wavelengths as "Pulsars". Their emission is beamed along the magnetic axis of the star, which may not be aligned with its rotation axis. This emission sweeps out a cone, which if it intersects our line of sight appears as periodic pulses the same way a steady lighthouse lamp appears to flash as it rotates when observed from a distance. These pulses were first observed in 1967 by then graduate student Jocelyn Bell (Hewish et al. (1968)). As foreshadowing for our own discovery of new variability (Chapter 8) more than 50 years later, the discovery required a new way of looking at the data. Radio observations at the time generally smoothed out signals, and any variable emission was identified as likely interference from terrestrial sources. Using a detector constructed to study the variable signals due to interplanetary scintillation (the interference of light due to differences in the index of refraction in the ionized interplanetary gas of the solar system) Bell found "interference" originating from a fixed position in the coordinates of the sky suggesting its non-terrestrial origin. Closer analysis showed the regular period of the signal, and the field of pulsar astronomy was born.

A pulsar wind nebula (PWN) is a non-thermal bubble blown by the relativistic wind of a rapidly rotating neutron star. The strong magnetic field of these objects accelerates charged particles to high energies, which then radiate across the electromagnetic spectrum due to interactions with the magnetic field. The lifetime of synchrotron emitting electrons is less than the age of the

nebula, thus requiring continued injection. Rapidly rotating neutron stars are the accepted source which emit a relativistic magnetized wind of fields and particles (Gaensler & Slane (2006); Kargaltsev & Pavlov (2008); Safi-Harb (2012)).

1.1 Thesis Motivation

At the time of writing, there are 111 known Galactic PWNe (SNRcat[1] Ferrand & Safi-Harb (2012)) which display unique characteristics. This number includes PWN candidates, composite remnants with both a PWN and a shell, and confirmed PWNe. A consistent study of PWNe in different environments, line of sight alignments, and stages of development allows for distinct aspects to be examined. Determining which features are products of environment or intrinsic to the nature of supernova remnants (SNRs) and PWNe is important in developing an understanding of their behaviour and evolution.

One of the main questions regarding SNRs is the existence of a class known as "naked PWNe". These show a prominent PWN without the surrounding shell of emission expected from a supernova explosion. Roughly 10% of known PWNe belong to this class (Safi-Harb (2016)). With deep observations, we study the surrounding medium to search for the missing shells and place limits on the explosion energy. With this information we learn whether these isolated

[1] http://snrcat.physics.umanitoba.ca/

PWNe are a result of a special low energy supernova explosion, merely a result of expansion in a low density bubble, or both.

The deep observations to search for shell emission also allow for detailed spatially resolved spectroscopy of the PWNe. With this we study the pulsar wind. Despite more than 50 years passing since the initial discovery of pulsars, their relativistic wind propagation is not well understood. There are two main methods which have been used to gain a better understanding. A magnetohydrodynamic (MHD) approach to model the flow of the magnetic field in the nebula, and a diffusion approach to model how particles diffuse through the field. We extract radial profiles to compare the variation of the spectral index with distance from the pulsar to that predicted by the diffusion and basic 1-D MHD models, and compare spectral maps to those predicted by multi-dimensional MHD simulations.

Pulsar wind nebulae are considered to be remarkably stable in their emission and are used as calibration sources for each new X-ray mission. However, a new way of looking at these objects reveals there is much more lurking below the surface. Spectral maps reveal variability is common and provide a new avenue for theorists to explore on the way to explaining the theory of pulsar winds.

Chapters 2 – 5 introduce the basic theory and background of wind propagation and emission, SNR classification and evolution, and the basics of X-ray observations. In Chapter 6 we present a deep observation of G21.5–0.9, combining all available *Chandra* data taken over its 20 year operating lifetime. We

address the isolated PWN question through analysis of the emission from the faint X-ray shell, and the wind models through comparison of the radial profile with predictions from symmetric MHD and diffusion models.

In Chapter 7 we present an *XMM-Newton* observation of CTB 87. This remnant is more evolved than G21.5–0.9 and yet no shell emission has been found. We search for thermal emission from the missing shell and place limits on the density of the surrounding medium. We present the first X-ray spectral map and compare with the results of a numerical simulation.

Chapter 8 presents our spectral map analysis of a sample of PWNe. We revisit the PWN within G21.5–0.9 and discover variable emission. We compare this result with several other PWNe to determine if the result is particular to G21.5–0.9 or a more widespread phenomenon.

We summarize our findings in Chapter 9, placing the results in context with developments from the field, and identify opportunities for future work to build upon our results.

Chapter 2

Non-thermal and Thermal Emission Theory

Before we dive into observations, it is important to understand the relevant theory used to infer the physical properties of the systems studied. All of the information we receive from SNRs and PWNe comes in the form of light. We therefore begin with a summary of the basic physics, and continue through to the observable consequences and emission mechanisms.

2.1 Particle Motion in a Magnetic Field

A charged particle moving in a magnetic field will experience a force (eg. Jackson (1999)):

$$\frac{d}{dt}(\gamma m_0 \vec{v}) = q(\vec{v} \times \vec{B}). \tag{2.1}$$

Where m_0 is the particle rest mass, $\vec{v}$ is the velocity, q is the charge, $\vec{B}$ is the magnetic field, and the lorentz factor γ is given in terms of the velocity as a fraction of the speed of light, c:

$$\gamma = \left(1 - \frac{\vec{v} \cdot \vec{v}}{c^2}\right)^{-1/2}.$$

Expanding the left hand side of Equation 2.1 gives

$$m_0 \frac{d}{dt}(\gamma \vec{v}) = m_0 \gamma \frac{d\vec{v}}{dt} + m_0 \gamma^3 \vec{v} \left(\frac{\vec{v} \cdot \vec{a}}{c^2}\right).$$

In a magnetic field, the acceleration $\vec{a} = d\vec{v}/dt$ is always $\perp \vec{v}$ such that $\vec{v} \cdot \vec{a} = 0$ leaving

$$\gamma m_0 \frac{d\vec{v}}{dt} = q(\vec{v} \times \vec{B}). \tag{2.2}$$

Splitting this into components parallel and perpendicular to the magnetic field, the $\vec{v}_{\parallel}$ is constant while the perpendicular component follows

$$\gamma m_0 \frac{d\vec{v}}{dt} = q v_{\perp} |B| (\vec{i_v} \times \vec{i_B}) = q|v||B| \sin\theta (\vec{i_v} \times \vec{i_B}). \tag{2.3}$$

Where $\vec{i_v}, \vec{i_B}$ are unit vectors in the direction of $\vec{v}$ and $\vec{B}$ respectively, and θ is the angle between them also known as the pitch angle. A charged particle therefore traces a helical path following a field line with a gyroradius defined as

$$\frac{v_{\perp}^2}{r} = \frac{q|\vec{v}||\vec{B}| \sin\theta}{\gamma m_0}, \tag{2.4}$$

$$r = \frac{\gamma m_0 |\vec{v}| \sin\theta}{q|\vec{B}|}, \tag{2.5}$$

and a gyro frequency as

$$\begin{aligned} \omega_g &= \frac{v_\perp}{r} = \frac{q|\vec{B}|}{\gamma m_0}, \\ \nu_g &= \frac{\omega_g}{2\pi} = \frac{q|\vec{B}|}{2\pi\gamma m_0}. \end{aligned} \tag{2.6}$$

2.2 Synchrotron Non-thermal Radiation

Cyclotron radiation is the emission from a non-relativistic particle undergoing helical motion, while synchrotron radiation is the relativistic equivalent. Here we follow the analysis of Longair (2011) and quote the important results. For a more complete derivation of synchrotron radiation, see Pacholczyk (1970).

2.2.1 Spectrum of a single particle

A charged particle with accelerations $a_\perp$, $a_\parallel$ as measured in the lab frame radiates according to

$$-\left(\frac{dE}{dt}\right) = \frac{q^2\gamma^4}{6\pi\epsilon_0 c^3}(|a_\perp|^2 + \gamma^2|a_\parallel|^2). \tag{2.7}$$

As found previously, $a_{\parallel} = 0$ and $a_{\perp}$ is given by equation 2.4. Substituting this into the previous expression gives

$$-\left(\frac{dE}{dt}\right) = \left(\frac{q^4 B^2}{6\pi\epsilon_0 c m_0^2}\frac{v^2}{c^2}\right)\gamma^2 \sin^2\theta. \tag{2.8}$$

The $1/m^2$ dependence of the radiated power means that the radiation from electrons is much more significant than any emission from protons or heavy ions. We will therefore replace q and m_0 with e the electron charge, and m_e the electron mass throughout the rest of the discussion. We can rewrite this result as

$$-\left(\frac{dE}{dt}\right) = 2\sigma_T c U_{mag}\left(\frac{v^2}{c^2}\right)\gamma^2 \sin^2\theta \tag{2.9}$$

where $\sigma_T = \frac{e^4}{6\pi\epsilon_0^2 m_e^2 c^4}$ is the Thomson cross section, and $U_{mag} = \frac{B^2}{2\mu_0}$ is the magnetic energy density. The pitch angle α is expected to be randomized over a particles lifetime, so we average over an isotropic distribution of pitch angles $P(\alpha)d\alpha = \frac{\sin\alpha d\alpha}{2}$

$$-\left(\frac{dE}{dt}\right) = \frac{4}{3}\sigma_T c U_{mag}\left(\frac{v^2}{c^2}\right)\gamma^2. \tag{2.10}$$

From this it is also apparent that for ultra-relativistic particles, $v/c \sim 1$ and the time for a particle to radiate its energy $E/\frac{dE}{dt} \propto 1/E$. The higher energy a particle has, the more quickly it radiates away. The spectrum of synchrotron emission is more complicated. In the non-relativistic case a particle radiates

isotropically with frequency

$$\nu_g = \frac{eB}{2\pi m_e}. \tag{2.11}$$

In the relativistic case, beaming becomes important and the particle no longer radiates in an isotropic manner. The emission follows

$$j(\omega) = \frac{\sqrt{3}e^3 B \sin\alpha}{8\pi^2 \epsilon_0 c m_e} F(x), \tag{2.12}$$

where $x = \nu/\nu_c$, $\nu_c = \frac{3eB\gamma^2 \sin\alpha}{4\pi m_e} = \frac{3}{2}\gamma^2 \nu_g \sin\alpha$ and

$$F(x) = x \int_x^\infty K_{5/3}(z) dz. \tag{2.13}$$

Here $K_{5/3}$ is a modified Bessel function of order 5/3. A plot is shown in Figure 2.1. The spectrum is peaked near the critical frequency and has asymptotic limits at low and high frequency of

$$\begin{gathered} x \ll 1 \\ F(x) \rightarrow \frac{4\pi}{\sqrt{3}\Gamma(\frac{1}{3})} \left(\frac{x}{2}\right)^{\frac{1}{3}}, \\ x \gg 1 \\ F(x) \rightarrow \left(\frac{\pi}{2}\right)^{\frac{1}{2}} x^{\frac{1}{2}} e^{-x}. \end{gathered} \tag{2.14}$$

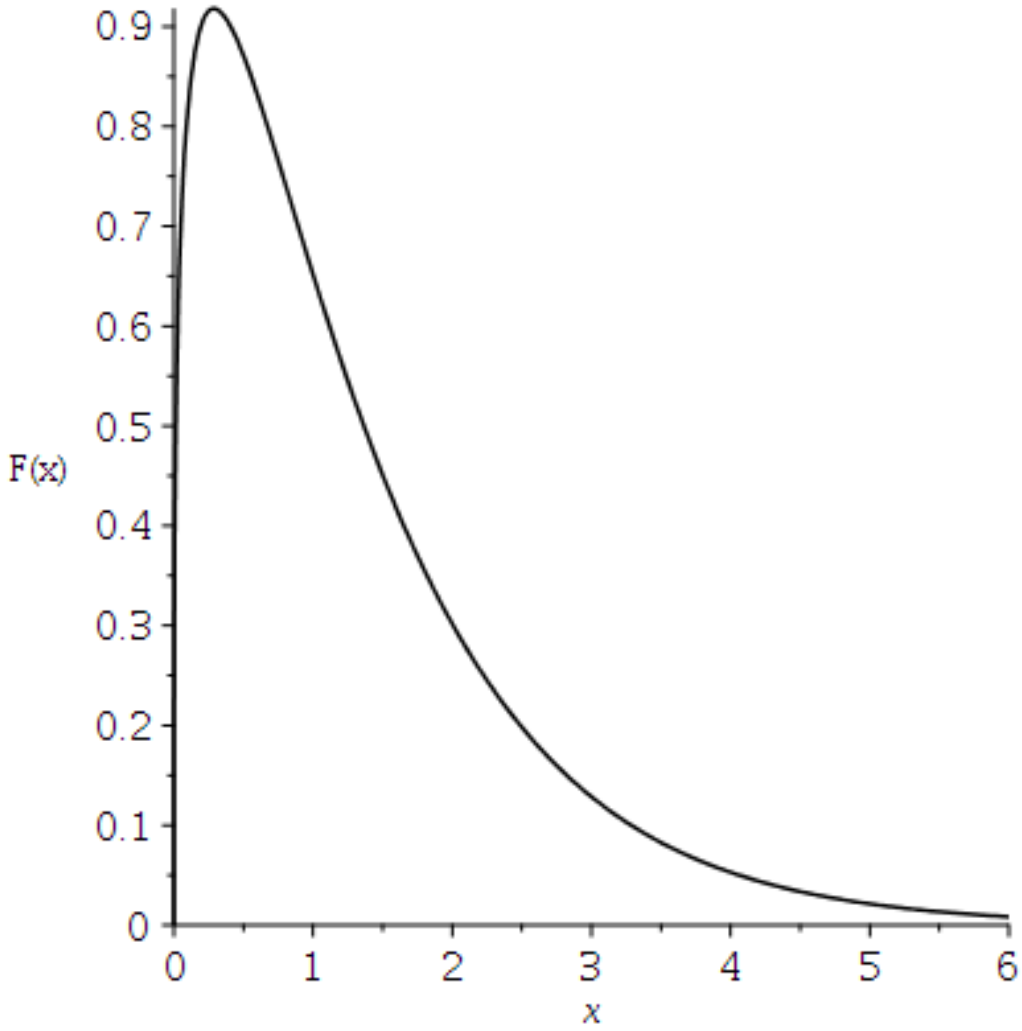

Figure 2.1: Function describing the power spectrum of synchrotron radiation from a single electron. $x = \omega/\omega_c$. The function peaks at $x \sim 0.29$.

2.2.2 Power-law distribution of electron energies

Next let us make a simplified physical argument for the spectrum of a power-law distribution of particle energies, again following the analysis presented in Longair (2011). Assuming a distribution given by

$$N(E)dE = kE^{-p}dE \tag{2.15}$$

where $N(E)dE$ is the number density of electrons in the energy range $E \rightarrow E + dE$, and k is a constant. The spectrum of synchrotron emission is sharply peaked (more so at least than the electron energy spectrum), we therefore assume that an electron of energy E radiates away its energy at the critical frequency ν_c

$$\nu \approx \nu_c = \gamma^2 \nu_g = \frac{E^2}{(m_e c^2)^2} \nu_g. \tag{2.16}$$

The energy radiated in the frequency range $\nu \rightarrow \nu + d\nu$ can then be attributed to electrons with energies in the range $E \rightarrow E + dE$ leading to

$$j(\nu)d\nu = -\left(\frac{dE}{dt}\right) N(E)dE. \tag{2.17}$$

Substituting in the result from Equation 2.10, and rearranging the expression for ν_c to find $dE = \frac{m_e c^2}{2\nu_g^{1/2}} \nu^{1/2} d\nu$ we arrive at:

$$j(\nu) \propto \nu^{\frac{-(p-1)}{2}} B^{\frac{(P+1)}{2}}. \tag{2.18}$$

A power-law spectrum with $j(\nu) \propto \nu^{-\alpha}$ is related to the particle energy spectrum by

$$\alpha = \frac{p-1}{2}. \tag{2.19}$$

Therefore, by observing synchrotron emission we can identify the presence and relative abundance of electrons with a given energy.

2.3 Thermal Emission Models

While the emission from PWNe is primarily non-thermal, SNRs emit abundant thermal X-ray emission. Here we briefly describe the emitting mechanisms and direct the interested reader to detailed derivations from e.g. Rybicki & Lightman (1986); Longair (2011). The appearance of the spectrum of each of the following thermal models and the non-thermal synchrotron model of the previous section is displayed in Figure 5.3.

2.3.1 Thermal Bremsstrahlung

When a free electron passes near a positive ion, it experiences the electric field and is accelerated. For a hot ionized optically thin gas (e.g. the plasma in young SNRs) this leads to thermal bremsstrahlung radiation. This is also known as free-free emission since the electron remains unbound through the process. The intensity of the emission is given by

$$I(E,T) = AG(E,T)Z^2 n_e n_i (kT)^{1/2} e^{-E/kT}. \quad (2.20)$$

Where A is a normalization constant, G is the Gaunt factor, Z is the charge of the positive ions, k is the Boltzmann constant, T is the temperature of the plasma, and n_e and n_i are the number density of the electrons and ions (Seward & Charles (2010)).

2.3.2 Line Emission

Collisions of atoms in a hot gas may excite bound electrons to higher energy levels. When the atom decays to a lower energy state it emits a photon characterised by the difference in energy. This appears as spectral lines which are used to determine the elemental composition of the emitting gas. The specific lines associated with individual elemental transitions may be found in the AtomDB[1] database.

2.3.3 Blackbody Radiation

The most familiar of thermal emission models is blackbody radiation. This is the mechanism by which a heated object will start to glow. Within a SNR, it may be seen from the surface of a neutron star. The colour depends on the temperature of the object (a stove-top element will glow with a red colour while

[1] http://www.atomdb.org/

an incandescent light bulb will glow with a yellow/white colour). The higher the temperature, the more energetic photons it will emit, and the peak shifts to shorter wavelengths. For young neutron stars with characteristic temperatures of $\sim 10^7$ K the peak wavelength is in the X-ray band. The spectrum is given by

$$I(E,T) = \frac{2E^3}{h^2c^2(e^{E/kT}-1)}, \tag{2.21}$$

where h is Planck's constant.

Chapter 3

SNR Morphology and Evolution

3.1 SNR Classification

Supernova remnants are traditionally classified based on their radio morphology. This has been recently complemented with X-ray observations. They fall into three main types: Shell, filled-centre, and composite. Shell type remnants appear as ring like structures and emit thermal X-ray emission (Section 2.3) and non-thermal radio emission due to the gas compressed and heated by the expanding shock. Filled-centre types have been called Crab-like or plerionic (derived from the ancient Greek word pleres - $\pi\lambda\eta\rho\eta s$ meaning "full"; Weiler & Panagia (1978)) and display non-thermal emission (Section 2.2) powered by a rapidly rotating neutron star. Composite remnants may be either thermal composites which display a shell with a filled centre containing thermal X-ray emission, or plerionic composites which appear as a shell filled with non-thermal emission.

3.2 Supernova Blast Wave and Ejecta

Following the supernova explosion the blast wave expands freely into the circumstellar medium, sweeping up material as it travels. The size (r) during this phase may be written in terms of the expansion velocity (v) and time (t) since the explosion:

$$r = vt. \tag{3.1}$$

Once the shell has swept up an amount of material comparable to the ejecta mass, the expansion velocity may no longer be approximated as constant. The expansion moves into the Sedov-Taylor phase. Here the energy in the shell remains approximately constant as the energy radiated is negligible compared to its internal energy. The theory was developed during the 2nd world war with applications for atomic bombs and was later declassified (Taylor (1950a,b)). The dependence of shell radius on time can be found from dimensional analysis (eg. Longair (2003)) to yield:

$$r \propto (E/\rho_0)^{1/5} t^{2/5}. \tag{3.2}$$

Where E is the explosion energy and ρ_0 is the density of the surrounding medium.

The Sedov-Taylor phase continues until the material in the shell cools to $\sim 10^6$ K. The energy lost to line emission becomes important, and the adiabatic

approximation no longer holds. The shell continues to expand, sweeping up matter and can be described using the conservation of momentum such that $M(t)v(t) = \text{Constant}$. The shell then expands as

$$r \propto t^{1/4}. \tag{3.3}$$

The expansion slows until the shell merges into the ISM and fades away; the elemental enrichment being the only evidence remaining of the explosive event.

3.3 Pulsar Wind Nebula Evolution

Pulsar wind nebulae begin their lives within the expanding supernova remnant shell. Their evolution is therefore tied to the evolution of the shell. The basic picture is explained in the review paper by Gaensler & Slane (2006). Initially, the pulsar wind expands freely into the low density environment behind the shock. As the shell sweeps up mass and enters the Sedov-Taylor phase, the shock develops a complex structure consisting of the forward shock where the ambient medium is compressed and heated, and a reverse shock where the unshocked ejecta are slowed. The reverse shock moves outward to start, but eventually moves inwards due to the build up of thermal pressure in the shell. The reverse shock compresses the PWN which responds with an increase in pressure leading to expansion, and the system reverberates with a timescale of several thousand years. The interaction of the reverse shock and the PWN causes Rayleigh-Taylor instabilities, mixing thermal material into the PWN.

In practice, the evolution is more complicated. The ambient medium is often asymmetric such that the reverse shock moves inwards faster in some directions than others leading to a complicated three-dimensional morphology. The pulsar may receive a "kick" during the supernova due to an asymmetric explosion and move away from the centre of the remnant with a velocity of $\sim 400 - 500$ km/s. As the pulsar moves it continues to generate a smaller PWN that shines in X-rays around its current position. The original wind bubble survives as a relic nebula visible in radio with a bridge of radio and X-ray emission trailing along the path taken by the pulsar (van der Swaluw et al. (2004)). Near the edge of the SNR, the local sound speed in the ejecta drops and the pulsars motion becomes supersonic and it drives a bow shock. The ram pressure confines the PWN which resembles a cometary appearance in X-ray. Eventually, the pulsar leaves the SNR and races out into the ISM. Here the motion is highly supersonic and the bow shock may be visible in Hα emission in the case where the propagation is through neutral gas, and synchrotron radiation lighting a bright head and cometary tail in radio and X-ray.

3.4 Pulsar Wind Nebula Morphology

The relativistic wind of the pulsar expands freely until it is confined by the ambient pressure in the SNR interior. The wind slows to meet the boundary condition, forming a wind termination shock where the ram pressure of the

wind matches the pressure in the nebula, and located at a radius of:

$$r_w = \sqrt{\frac{\dot{E}}{4\pi\omega c P_{\rm PWN}}}. \tag{3.4}$$

Here $\dot{E}$ is the energy output of the pulsar, ω is the equivalent filling factor for an isotropic wind, c is the speed of light, and P_{PWN} is the pressure in the nebula. Typical values yield termination shock radii of ~ 0.1 pc (Gaensler & Slane (2006)). This feature is observed as a ring or torrus feature in X-ray observations, while there is also collimated flow along the rotation axis leading to jet like morphology. The physics of this shock is further discussed in Section 4.2.

3.5 Pulsar Evolution

The energy powering a PWN comes from the rotational energy loss of the pulsar. A rotating object has energy given by

$$E = \frac{1}{2} I \Omega^2, \tag{3.5}$$

where I is the moment of inertia of the object and Ω is its angular velocity. Taking the time derivative of this leads to

$$\dot{E} = \frac{1}{2} I \Omega \dot{\Omega}. \tag{3.6}$$

The dot notation refers to the time derivative ($\frac{d}{dt}$). The object slows according to

$$\dot{\Omega} = k\Omega^n \tag{3.7}$$

where k is a constant and n is the braking index. A rotating magnetic dipole radiates according to

$$-\dot{E} = \frac{\mu_0 \Omega^4 p_{m0}^2 \sin^2 \alpha}{6\pi c^3} \tag{3.8}$$

where p_{m0} is the magnetic dipole moment, α is the angle between the magnetic axis and the rotation axis, and μ_0 is the magnetic permeability of free space (Longair (2011)). At the neutron star surface, a dipole field has a strength of $B = \mu_0 p_{m0}/4\pi R^3$. Substituting this into the previous equation and assuming $\alpha = \pi/2$ we find

$$\dot{\Omega} = \frac{\mu_0 \Omega^3}{6\pi c^3 I}\left(\frac{4\pi R^3 B}{\mu_0}\right)^2 = \frac{8\pi \Omega^3 R^6 B^2}{3\mu_0 c^3 I}. \tag{3.9}$$

A uniform sphere has moment of inertia $I = 2MR^2/5$, so solving for the magnetic field gives:

$$B = \left(\frac{3\mu_0 c^3 M \dot{\Omega}}{20\pi\Omega^3 R^4}\right)^{1/2} = \left(\frac{3\mu_0 c^3 M}{80\pi^3 R^4}\right)(P\dot{P})^{1/2}. \tag{3.10}$$

Canonical values of $R = 10$km, $M = 1.4M_\odot$ leads to:

$$B = 3 \times 10^{19}(P\dot{P})^{1/2} G. \tag{3.11}$$

If the braking index is constant through the lifetime of the pulsar, the age can be derived by integrating Eq. 3.7 leading to:

$$\frac{1}{(n-1)}\left[\Omega^{-(n-1)} - \Omega_0^{-(n-1)}\right] = k\tau, \tag{3.12}$$

where Ω_0 is the initial angular velocity and τ is the age of the pulsar. For $n > 1$ and assuming the initial rotation rate was much larger than the current value, τ reduces to:

$$\tau = \frac{\Omega^{-(n-1)}}{k(n-1)} = -\frac{\Omega}{(n-1)\dot{\Omega}} = \frac{P}{(n-1)\dot{P}}, \tag{3.13}$$

where P is the rotation period.

Assuming magnetic dipole radiation is the only form of energy loss leads to the braking index $n = 3$ and the characteristic age $\tau = P/2\dot{P}$.

If the second time derivative of the period can be measured, the braking index can be calculated through:

$$n = \frac{\Omega\ddot{\Omega}}{\dot{\Omega}^2}. \tag{3.14}$$

For the few pulsars which have had their braking indices measured the values are in the range $0 < n < 7$ (Marshall et al. (2016); Ferdman et al. (2018)). However the magnetic dipole radiation ($n = 3$) and the canonical values are still widely used by the community (Gaensler & Slane (2006)).

Chapter 4

Wind Models

Prior to the observation of pulsations leading to the discovery of rotating neutron stars, astronomers had problems explaining the features observed in PWNe such as the Crab nebula (Figure 4.3). In the 1950s the emission was concluded to be non-thermal synchrotron emission (Section 2.2) by Shklovskii (1953) (Dogel' et al. (2012)). The magnetic energy requirements of the nebula were then problematic. Among interesting suggestions for the source of the magnetic energy was from nuclear reactions in the central star powering the nebula (e.g. Piddington (1957)). Following the discovery of pulsars, the wind theory progressed rapidly. While understanding the general morphology (Chapter 3) was relatively straightforward, replicating the observed spatially dependent spectra proved to be more challenging. The lifetime of synchrotron emitting electrons is energy dependent (Section 2.2). Therefore, to reproduce the observed spectra, the way the particles in the wind move from injection at the pulsar to the outer nebula must be modelled precisely. Here we summarize the

early work which led to the current understanding of the pulsar magnetosphere, and follow the progression of models for the pulsar wind through the symmetric 1-D MHD to 3-D MHD and diffusion models on which our X-ray analysis in Chapters 6 and 7 relies.

4.1 Wind Formation and Basic Structure

Goldreich & Julian (1969) proposed an aligned rotating dipole model for the magnetosphere of a pulsar, showing that such a system cannot exist in vacuum. The force from the induced electric field is many orders of magnitude larger than the gravitational force resulting in charges ripped from the surface to fill the magnetosphere. The general picture they proposed is as follows. Near the surface of the neutron star the magnetic field lines are closed and the particles attached rotate like a rigid body. This must fail at some radius before $R_l \sin\theta = c/\Omega$ defining the light cylinder, otherwise particles would be required to travel faster than light. Magnetic field lines which pass through the light cylinder must then be open and charges stream out along them forming the pulsar wind. A schematic is shown in Figure 4.1. Particle pair production occurs along the open polar field lines (Sturrock (1971); Ruderman & Sutherland (1975)). Electron-positron pairs are created at a rate measured in terms of the pair multiplicity, κ, which describes the number of pairs created by a single primary particle. The value of κ varies between models, with values ranging from a few to more than thousands (Kirk et al. (2009)). The primary

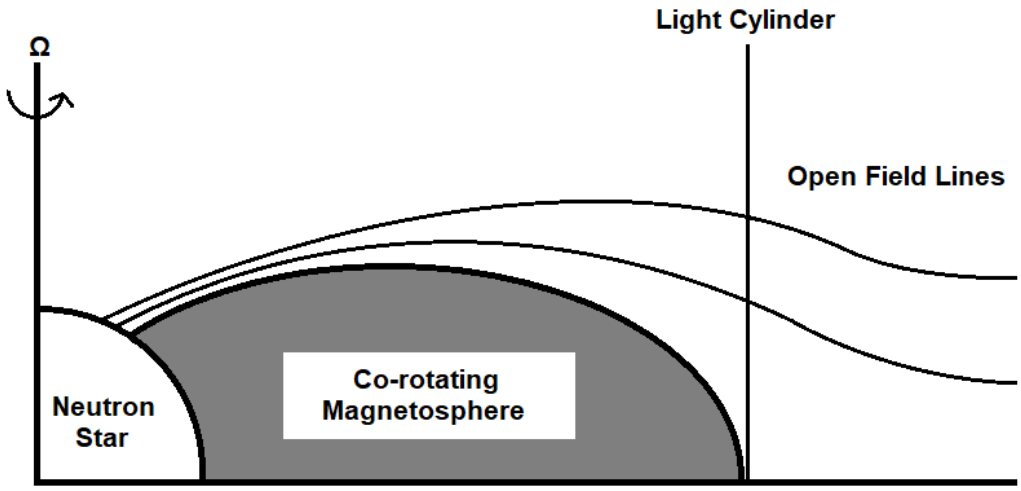

Figure 4.1: Schematic diagram of a pulsar magnetosphere extending past the light cylinder into the wind zone. Based on Figure 1 from Goldreich & Julian (1969).

beams consist of particles of a single charge, and the charge density of the flow is expected to be close to the Goldreich-Julian density. This is defined in terms of the charge required to screen the induced electric field:

$$n_{GJ} = | \left(\frac{\Omega \cdot B}{2\pi ec} \right) |. \tag{4.1}$$

Rees & Gunn (1974) expanded on this model in order to describe the field structure throughout the nebula. Within a radius R_s an energy flux $|I\Omega\dot{\Omega}|$ flows out in the form of a toroidal magnetic field and electromagnetic waves of frequency Ω. Here Ω is the angular velocity of the neutron star, $\dot{\Omega}$ is the change of this angular velocity with time, and I is the moment of inertia of the

neutron star. The ratio of the energy carried by the field to that carried by particles is given in terms of the magnetization σ:

$$\sigma = \frac{B^2}{4\pi n u \gamma m_e c^2}. \tag{4.2}$$

Where n is the particle number density, and $u = \gamma v/c$ is an expression of the relativistic speed of the radial flow of the wind. There is a shock discontinuity at R_s where the pressure of the wind is balanced by the pressure of the nebula. First consider if the energy from the pulsar is entirely in the form of an ultra relativistic wind. The outward velocity just outside R_s is slightly less than $c/\sqrt{3}$, the sound speed is $\sim c/\sqrt{3} \gg \dot{R}_{neb}$ where $\dot{R}_{neb}$ is the expansion velocity of the edge of the nebula. The pressure will be roughly uniform throughout the nebula, and the outward velocity decreases smoothly from $\sim c/\sqrt{3}$ at R_s to $\dot{R}_{neb}$ at the edge of the nebula, varying as r^{-2}. Next add a toroidal field, weak such that magnetic stresses are not significant. At the shock, there is a discontinuous increase by a factor $\sim \sqrt{3}$ corresponding to the sudden decrease in the outward velocity from the Rankine-Hugoniot jump conditions (e.g. Longair (2011)). The field then increases as $B \propto r$ as the $1/r$ dependence is outweighed by the $1/r^2$ dependence of the velocity. The field may be thought of as a series of winding lines which are compressed in the outer nebula due to the slowing expansion velocity.

4.2 Termination shock and Ideal MHD

Shocks correspond to a sudden change in the properties of a gas across some boundary. In PWNe a shock is formed where the pressure of the wind is balanced by the internal pressure of the nebula. This occurs at the termination shock (Section 3.4, Figure 4.2). The physical quantities on either side of the shock are related by conservation laws also known as the Rankine-Hugonoit conditions. The conservation of mass, momentum, and energy are as follows (Longair (2011)):

$$\rho_1 v_1 = \rho_2 v_2, \tag{4.3}$$

$$P_1 + \rho_1 v_1^2 = P_2 + \rho_2 v_2^2, \tag{4.4}$$

and

$$\rho_1 v_1 \left(\frac{v_1^2}{2} + w_1 \right) = \rho_2 v_2 \left(\frac{v_2^2}{2} + w_2 \right). \tag{4.5}$$

Where ρ is density, P is pressure, and $w = \varepsilon_m + P/\rho$ is the enthalpy per unit mass with ε_m the internal energy per unit mass. These can be extended using Maxwell's equations to arrive at the relativistic MHD equations in conservative form (Del Zanna & Olmi (2017)):

$$\frac{\partial}{\partial t}(\rho\gamma) + \nabla \cdot (\rho\gamma \mathbf{v}) = 0, \tag{4.6}$$

$$\frac{\partial}{\partial t}\left(\frac{w}{c^2}\gamma^2 \mathbf{v} + \frac{\mathbf{E}\times\mathbf{B}}{4\pi c}\right) + \nabla\cdot\left[\frac{w}{c^2}\gamma^2 \mathbf{v}\mathbf{v} - \frac{\mathbf{E}\mathbf{E}+\mathbf{B}\mathbf{B}}{4\pi} + \left(P + \frac{E^2+B^2}{8\pi}\right)\mathbf{I}\right] = 0, \tag{4.7}$$

and

$$\frac{\partial}{\partial t}\left(w\gamma^2 - P + \frac{E^2+B^2}{8\pi}\right) + \nabla\cdot\left[w\gamma^2\mathbf{v} + \frac{c}{4\pi}(\mathbf{E}\times\mathbf{B})\right] = 0. \tag{4.8}$$

Where ρ is the rest mass density of the fluid, P is the pressure in the local rest frame, $\mathbf{v}$ is the bulk flow velocity, $w = \rho c^2 + 4P$ is the relativistic enthalphy, E, B, are the electric and magnetic field as measured in the lab frame, and $\mathbf{I}$ is the identity tensor. The fluid and fields are coupled through Ohm's law:

$$\mathbf{E} + \frac{\mathbf{v}}{c}\times\mathbf{B} = \frac{\mathbf{J}}{\sigma_c}. \tag{4.9}$$

Where σ_c is the plasma electric conductivity which in the ideal MHD limit, $\sigma_c \to \infty$.

4.3 Magnetohydrodynamics and the KC84 Model

Kennel & Coroniti (1984a,b), hereafter KC84, outlined a few problems with the simple model proposed by Rees & Gunn (1974). For the hydrodynamic model to be consistent, equipartition where the field and particle pressures are balanced should not occur closer than the edge of the nebula R_n. Furthermore, the brightness profile across the nebula does not agree with a linearly increasing magnetic field all the way to R_n. KC84 begin by solving the Rankine-Hugoniot equations for a strong shock, relating the upstream (pre-shocked wind, denoted with subscript 1) conditions to those downstream (post-shock, subscript 2) in

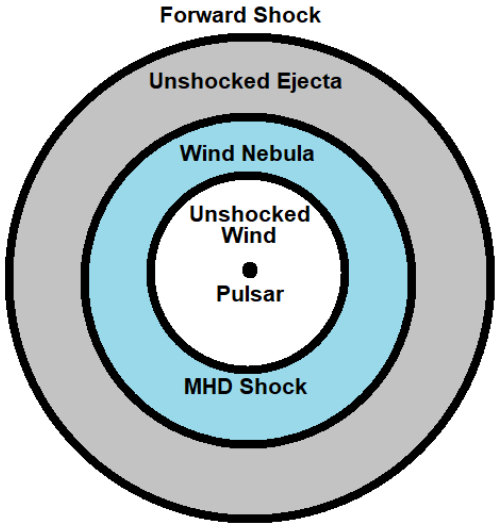

Figure 4.2: Schematic figure of a PWN within an expanding SNR shell. The centre point marks the pulsar and magnetosphere where a plasma wind is initially created. The wind expands in the wind zone which is bounded by a strong MHD shock (the termination shock). The nebula extends from the MHD shock to the outer edge where it is confined by the SNR shell.

terms of the magnetization σ. If the upstream flow is highly relativistic such that $u_1 \approx \gamma_1$, and the downstream pressure is relativistically large ($P_2/n_2 m_e c^2 \gg 1$) such that the adiabatic index $\Gamma_2 = 4/3$, the strong shock relations reduce to

$$u_2^2 = \frac{8\sigma^2 + 10\sigma + 1}{16(\sigma+1)} + \frac{1}{16(\sigma+1)}\left[64\sigma^2(\sigma+1)^2 + 20\sigma(\sigma+1) + 1\right]^{\frac{1}{2}}, \quad (4.10)$$

$$\frac{B_2}{B_1} = \frac{N_2}{N_1} = \frac{\gamma_2}{u_2}, \quad (4.11)$$

and

$$\frac{P_2}{n_2 m_e c^2 u_1^2} = \frac{1}{4u_2\gamma_2}\left[1 + \sigma\left(1 - \frac{\gamma_2}{u_2}\right)\right]. \quad (4.12)$$

Where $N = \gamma n$ is the shock frame number density. For the limit of small $\sigma \ll 1$ where the flow is particle dominated these give

$$u_2^2 \approx \frac{1+9\sigma}{8},\ \gamma_2^2 \approx \frac{9+9\sigma}{8},\ \beta_2 = \frac{u_2}{\gamma_2} \approx \frac{1}{3}(1+4\sigma), \quad (4.13)$$

$$\frac{B_2}{B_1} = \frac{N_2}{N_1} \approx 3(1-4\sigma), \quad (4.14)$$

and

$$\frac{P_2}{n_1 m_e c^2 u_1^2} \approx \frac{2}{3}(1-7\sigma). \quad (4.15)$$

While for large $\sigma \gg 1$ where the field is dominant the equations become

$$u_2^2 \approx \sigma + \frac{1}{8} + \frac{1}{64\sigma}, \quad (4.16)$$

$$\gamma_2^2 \approx \sigma + \frac{9}{8} + \frac{1}{64\sigma}, \tag{4.17}$$

and

$$\frac{B_2}{B1} = \frac{N_2}{N_1} \approx 1 + \frac{1}{2\sigma}. \tag{4.18}$$

The flow rate and conditions in the nebula can then be found in the steady state, toroidal field approximation from the conservation of number flux:

$$\frac{d}{dr}(cnur^2) = 0, \tag{4.19}$$

magnetic flux conservation in the MHD approximation:

$$\nabla \times \left(\frac{u \times B}{\gamma}\right) = 0 \rightarrow \frac{d}{dr}\left(\frac{ruB}{\gamma}\right) = 0, \tag{4.20}$$

propagation of internal energy:

$$\frac{d}{dr}(nur^2 e) + P\frac{d}{dr}(r^2 u) = 0, \tag{4.21}$$

where e is the relativistic internal energy per particle, and the conservation of total energy:

$$u\frac{d}{dr}(\gamma\varepsilon) \equiv \frac{d}{dr}\big[nur^2\left(\gamma u + \frac{B^2}{4\pi n\gamma}\right)\big]. \tag{4.22}$$

Where ε is the total electromagnetic plus particle energy per particle in the proper frame:

$$\varepsilon = \mu + \frac{B^2}{4\pi n\gamma^2}, \tag{4.23}$$

and $\mu = e + P$ is the specific enthalpy.

A small value of σ produces a nonrelativistic flow speed at the edge of the nebula which may match the flow speed of an expanding stellar envelope. This is in agreement with observations of the Crab nebula. Changing to normalized distance, $z = r/r_s$, and velocity, $u = u_2 v$, where $v = 1$ at the shock, and assuming adiabatic flow, the density and magnetic field are given by:

$$n(z) = n_2 (v z^2)^{-1} \tag{4.24}$$

and

$$B(z) = \frac{B_2 z}{(v z^2)}. \tag{4.25}$$

The plasma pressure dominates the flow dynamics for $z < \bar{z} \approx 1/(3\sigma)^{-1/2}$ where vz^2 is roughly constant, and the magnetic field increases linearly with z. Past $\bar{z}$ the magnetic pressure dominates, v is roughly constant, the density drops as $1/z^2$, and the magnetic field as $1/z$. In general for the small σ limit:

$$v(z) \approx \frac{1}{1+\Delta}\left[1 + \left(\frac{\bar{z}}{z}\right)^{2/3}\right] \tag{4.26}$$

where

$$\Delta = \frac{(u_2^2/\sigma) - 1/2}{(u_2^2 + 1/4)}. \tag{4.27}$$

4.3.1 KC84 Emission model

In their second paper, Kennel & Coroniti (1984b) calculate the synchrotron continuum expected based on their 1-D spherically symmetric steady state MHD model. With $\epsilon = E/m_e c^2$, the normalized electron energy, the distribution function f_2 is assumed to follow a power law in energy between the bounds $\epsilon_2' < \epsilon_2''$:

$$f_2(\epsilon, \theta, \phi) = \frac{A}{4\pi}\epsilon_2^{-(2\alpha+1)}. \tag{4.28}$$

f_2 is independent of pitch angle θ, Larmor phase angle ϕ, and is zero outside the energy range $\epsilon_2' \leq \epsilon_2 \leq \epsilon_2''$. This energy range determines the local synchrotron bandwidth, and the frequency spectrum depends on the energy distribution injected at the shock as well as the spatial evolution of the particle distribution function and magnetic field with radius. The maximum emitted frequency corresponds to substituting ϵ_2'' into equation 2.16 They found radially dependent analytic expressions for the upper frequency emission limit:

$$\nu_c''(z) = \frac{3eB_2}{2m_e c}\frac{(5\epsilon_c)^2}{z^9}, \tag{4.29}$$

and lower frequency limit:

$$\nu_c'(z) = \frac{9}{32\pi}\left(\frac{2\alpha-1}{\alpha}\right)^2\left(\frac{L\sigma}{cr_s^2}\right)^{1/2}\frac{z}{(vz^2)^{5/3}}u_1^2. \tag{4.30}$$

Where $\epsilon_c = (8\sqrt{2}\frac{e^4}{m_e^3 c^7})^{-1}\frac{r_s}{\sigma L}$ is a scale energy which measures the importance of synchrotron burn off and L is the luminosity of the pulsar wind ($L =$

$4\pi n_1 \gamma_1 u_1 m_e c^3 r_s^2 (1+\sigma))$. This can be inverted to give the largest radius at which a given frequency will be emitted:

$$z''_\nu = (\bar{\nu}/\nu)^{\frac{1}{9}}, \tag{4.31}$$

where $\bar{\nu} = \frac{3eB_2}{2m_e c}(5\epsilon_c)^2$. The spectral distribution is given by:

$$\nu L_\nu = \alpha L(\alpha) \left(\frac{3eB_2}{2\nu m_e c}\right)^{\alpha-1} \left[I_2(z_{max}) - I_2(z_{min})\right]. \tag{4.32}$$

$L(\alpha)$ is a normalizing factor which depends on the energy bounds of the injected particle spectrum. z_{min} and z_{max} depend on the emission limits where $z_{max} = \min(z_N, z''_\nu)$, $z_{min} = \max(1, z'_\nu)$ and

$$I_2(\alpha, z) = \int_1^z dz' \frac{(z')^{3+\alpha}}{(vz'^2)^{2+(5\alpha/3)}}. \tag{4.33}$$

For comparison to observation, the volume emissivity where

$$j_\nu \propto \frac{1}{\nu^{\alpha-2}} \frac{z^{1+\alpha}}{(vz^2)^{2+5\alpha/3}} \tag{4.34}$$

is integrated along the line of sight to give:

$$i_\nu(z_\perp) = 2\int_{z^*}^{z_N} dz \frac{j_\nu(z) z}{\sqrt{z^2 - z_\perp^2}} \tag{4.35}$$

with $z^* = \max(1, z_\perp)$. As σ gets smaller, the emitting region becomes more broad while the cutoff where synchrotron burn off occurs becomes sharper.

The spectral index may then be calculated from

$$\alpha(\nu_1, \nu_2, z) = \frac{-\log\left[I_\nu(\nu_2, z)/I_\nu(\nu_1, z))\right]}{\log\left(\nu_2/\nu_1\right)} \tag{4.36}$$

The broad emission profile followed by a sharp cut off at ν'' leads to a relatively flat followed by suddenly rapidly rising spectral index. This does not agree with high resolution X-ray observations (e.g. Guest et al. (2019), Chapter 6) which finds the spectral index rises linearly with distance from the pulsar and flattens towards the outer boundary.

4.3.2 KC84 Summary

The spherically symmetric model presented displays frequency dependent size, an under-luminous region near the pulsar, and finds a small value of $\sigma \approx 0.003$ required to match boundary conditions in the outer nebula. The model is unable to explain the radial change in spectral index from high resolution X-ray observations (e.g. Guest et al. (2019)) or the jet/torus morphology observed in many PWNe (e.g. Gaensler & Slane (2006)).

4.3.3 2-D MHD

Progress in numerical relativistic fluid dynamics and MHD in the early 2000s allowed Del Zanna et al. (2004) to perform simulations of PWNe based on 2-D

axisymmetric wind models. Assuming a latitude dependence of the energy flux:

$$\gamma(\theta) = \gamma_0 \left[\delta + (1-\delta)\sin^2\theta\right], \tag{4.37}$$

and toroidal magnetic field:

$$B(r,\theta) = B_0 \frac{r_0}{r}\sin\theta. \tag{4.38}$$

The subscript 0 indicates values in the equatorial plane, and δ controls the ratio between the Lorentz factor at the pole to that at the equator. They find that a low magnetization leads to the formation of a torus and jet features. This work was extended by Del Zanna et al. (2006) to add a striped wind form for the magnetic field and include simulated synchrotron emission. When the magnetic and rotation axis of the pulsar are not aligned, there may exist a striped region along the equatorial plane where dissipation from opposing current sheets may form an unmagnetized region. This was modelled as:

$$B(r,\theta) = B_0 \frac{r_0}{r}\sin\theta \tanh\left[b\left(\frac{\pi}{2}\right) - \theta\right], \tag{4.39}$$

where b controls the angular size of the lower magnetization central region.

In common with the 1-D KC84 result, 2-D simulations require small values of the magnetization σ to match the expansion of the outer nebula. This is at odds with theory describing the pulsar magnetosphere (Arons (2012)) which predicts σ in excess of a few hundred at the light cylinder.

4.3.4 3-D MHD

Porth et al. (2013, 2014) performed 3-D relativistic MHD simulations and addressed the σ problem. Simulations with $\sigma = 1 - 3$ found the inner torus structure relatively unchanged from the 2-D results with a 1000 times smaller σ. Randomization of the magnetic field allowed by 3-dimensions paired with magnetic dissipation in the striped wind lead to the PWN being gas pressure dominated and mimicking the 1 and 2-dimension results. Hoop stresses from the regular field of freshly injected plasma lead to axial compression near the termination shock and drive polar outflows. They were found to be moderate compared to those derived from 2-D simulations suggesting the strong polar outflows found previously are artefacts of the imposed axial symmetry where the field is able to pile up along the axis. A limitation of this 3-dimensional simulation is that it has not been run until a self-similar expansion phase has been reached.

Olmi et al. (2016) used adaptive mesh refinement in their 3D simulations and evolved a simulated PWN to a self-similar stage. They find the field was mainly toroidal in the inner nebula and radial farther out. In the first ~ 100 years of the simulation, the average nebular field was found to decrease through magnetic dissipation until a minimum of $\sim 100\mu$G was reached after which it remained fairly constant. The trend indicates that magnetic dissipation progressively becomes less important, allowing the magnetic field to saturate to the equipartition value at some point.

4.4 Diffusion

In the MHD discussion, it is assumed that particles are frozen into the field such that a particles motion through the nebula is completely determined by the flow of the magnetic field. Here we examine the role of diffusion. In the analytic Bohm diffusion limit which scales linearly with temperature and inversely with the magnetic field, the characteristic mean free path for particles to cross the magnetic field is limited to the particle gyroradius (de Jager & Djannati-Atai (2009)):

$$\lambda = 10^{-4} \left(\frac{E}{100TeV} \right) \left(\frac{B}{100\mu G} \right)^{-1} pc. \tag{4.40}$$

The escape time from a region of size R is then:

$$t_{esc} \approx 16,000 \left(\frac{R}{2pc} \right)^{2} \left(\frac{E}{100TeV} \right)^{-1} \left(\frac{B}{100\mu G} \right) yr. \tag{4.41}$$

This is much longer than the ages of the PWNe commonly used for comparison (Crab, G21.5–0.9, 3C58), especially for particles radiating below X-ray energy. Therefore cross field diffusion is expected to be negligible if the field is purely toroidal as assumed in KC84. X-ray and radio polarization observations support the view that while there is toroidal structure where the pulsar wind impacts the nebula, the flow is more radial in the outer nebula, suggesting diffusion is important in describing the outer regions (Tang & Chevalier (2012)).

4.4.1 Diffusion Energy Loss Equation

Following the analysis of Longair (2011), consider a box in coordinate space with sides energy and distance. Particles move in the x-direction by diffusion and the y-direction by energy gain or loss. The number of particles in dx and within E to $E + dE$ is $N(E, x, t)dEdx$. The rate of change of particle density in the box is then:

$$\begin{aligned}\frac{d}{dt}N(E,x,t)dEdx &= \big[\Phi_x(E,x,t) - \Phi_{x+dx}(E,x+dx,t)\big]dE \\ &+\big[\Phi_E(E,x,t) - \Phi_{E+dE}(E+dE,x,t)\big]dx + Q(E,x,t)dEdx,\end{aligned} \tag{4.42}$$

where $Q(E, x, t)$ is the rate of injection of particles per unit volume of coordinate space. Simplifying the notation leads to:

$$\frac{d}{dt}N = -\frac{\partial \Phi_x}{\partial x} - \frac{\partial \Phi_E}{\partial E} + Q. \tag{4.43}$$

Φ_x is the flux of particles through the energy interval dE at the point x such that

$$\Phi_x = -D\frac{\partial N}{\partial x} \tag{4.44}$$

where D is the diffusion coefficient. Φ_E is the flux of particles through dx with energy $E \to E + dE$. If $b(E)$ is the energy loss rate then

$$N(E)\frac{dE}{dt} = \Phi_E = -b(E)N(E). \tag{4.45}$$

Therefore, extending equation 4.43 to 3-D, we obtain:

$$\frac{dN}{dt} = D\nabla^2 N + \frac{\partial}{\partial E}\big[b(E)N(E)\big] + Q(E) \tag{4.46}$$

which is the diffusion equation.

4.4.2 Point source diffusion

Gratton (1972) developed a diffusion model with synchrotron losses and Wilson (1972) applied it to the Crab nebula. This was later extended by Tang & Chevalier (2012) to include advection, and examine the effect of permeable or reflecting boundaries. The Gratton model assumes a point source injects particles with a power-law spectrum (Eq.4.28, $p = 2\alpha + 1$) into an infinite space with constant magnetic field. The diffusion does not depend on energy and the only source of energy loss is synchrotron radiation ($dE/dt = -QE^2$ and $Q = 2.37 \times 10^{-3} B_\perp^2$ erg s^{-1}, $B_\perp^2 = (2/3)B^2$).

We summarize their results based on the observable impact on the spectral index distribution as presented by Tang & Chevalier (2012). The resulting spectral index profile varies in relation to the critical frequency ν_R where the ratio of diffusion distance to nebula radius η is $\approx (4Dt)^{1/2}/R = (4D/QER^2)^{1/2} = 1$.

$$\nu_R = 1 \times 10^{17} \left(\frac{D}{10^{27}\mathrm{cm^2 s^{-1}}}\right)^2 \left(\frac{1\mathrm{pc}}{R}\right)^4 \left(\frac{100\mu G}{B}\right)^3 \mathrm{Hz} \tag{4.47}$$

When $\nu \ll \nu_R$, $\eta \gg 1$, the diffusion distance d is much larger than the nebula radius R and the particles are well mixed resulting in a flat spectral index

profile. When $\nu \approx \nu_R$, $\eta \approx 1$, the photon index profile transitions to a power-law. When $\nu \gg \nu_R$, $\eta \ll 1$, the particle density drops quickly in the radial direction due to the short cooling time and the spectral index profile follows an exponential form. The size of a PWN is also determined by ν_R and η. When $\nu < \nu_R$, $\eta > 1$ in the steady state case, the nebula size remains the same due to the boundary condition of negligible magnetic field outside the boundary of the nebula to produce synchrotron emission. Thus when a particle diffuses through the outer boundary, it is no longer counted in the distribution of emitting particle energies. When $\nu > \nu_R$, $\eta < 1$, the size will shrink as the cooling time of particles is less than the diffusion time. This can be seen in observations of the Crab nebula (Figure 4.3) where the size observed in radio wavelengths is significantly larger than that seen in X-ray. Alternatively, G21.5-0.9 (Chapter 6, Figure 6.1) displays a consistent size between radio and X-ray observations.

4.4.3 Diffusion and advection

Tang & Chevalier (2012) examined the effect of advection using Monte Carlo simulations. Particles were injected at an inner shell representing the termination shock with motions given by:

$$\Delta S_{\rm tot} = V_{\rm adv}\Delta t \mathbf{r}_0 \pm (2D_x\Delta t)^{1/2}x_0 \pm (2D_y\Delta t)^{1/2}\mathbf{y}_0 \pm (2D_z\Delta t)^{1/2}\mathbf{z}_0, \quad (4.48)$$

where $\mathbf{x}_0, \mathbf{y}_0, \mathbf{z}_0, \mathbf{r}_0$ are unit vectors in the x,y,z, and radial directions, and $v_{\rm adv}$ is the flow velocity. The first term describes the advection flow and the later terms,

Figure 4.3: Multi-wavelength image of the Crab nebula. The size of the nebula decreases with the wavelength of observation (Section 4.4.2). X-ray (violet): NASA/CXC/SAO; Optical (green): NASA/STScI; Infrared (yellow): NASA/JPL/Caltech; Radio (red): NSF/NRAO/VLA; Ultraviolet (blue): ESA/XMM-Newton

the diffusion component. For spherical symmetry, $D_x = D_y = D_z$. Boundary conditions of reflection at the termination shock and nebula radius were added to represent the minimal cross-field line diffusion and preventing particles from escaping the nebula. The addition of advection does not significantly change the derived results due to the low ratio of diffusion time to advection time. The main difference is the addition of a reflecting outer boundary which leads to a flattening of the spectral index profile near the edge of the nebula.

Chapter 5

Observing X-ray Emission

The light we see with our eyes is only a small fraction of the electromagnetic spectrum. Low energy, long wavelength radio waves mark one end of the spectrum while high energy, short wavelength gamma rays (γ-rays) are at the other extreme. In this work we focus on X-ray observations. Due to the absorption of X-rays by Earths atmosphere, observations need to be taken from space based observatories. The two primary satellites used are the European space agency's *XMM-Newton*, and NASA's *Chandra X-ray Observatory*. Both are sensitive to the range $\sim$ 0.1–10 keV and have distinct advantages.

5.1 Chandra X-ray Observatory

Chandra was launched in 1999. Its structure consists of 4 nested mirrors with shallow reflection angles and an effective area of 800 cm^2 at 0.25 keV allowing for sub arc second imaging resolution. The mirrors focus incident X-rays

onto the focal plane which hosts two detectors: the advanced CCD imaging spectrometer (ACIS) and the high resolution camera (HRC). ACIS (See Figure 5.1) consists of a set of 10 charge-coupled device (CCD) chips with energy resolution of 95 eV at 1.5 keV. When an X-ray hits the CCD detector, it ionises atoms releasing free electrons. These are then collected to measure the charge. The more energetic the incoming photon, the more charge will be measured. The HRC consists of a micro-channel plate (MCP). This is a large number of channel electron multipliers. When an incident X-ray strikes the inside of one of the multiplier tubes, the generated free electrons are accelerated by an applied voltage and cascade down the tube knocking free additional electrons from the tube wall on their way. This process can amplify the initial charge by a factor of 10^4 (Seward & Charles (2010)).

5.2 XMM-Newton

The European X-ray multi-mirror Mission (*XMM-Newton*) was launched in 1999. Hosting 3 telescopes each with 58 nested mirrors and a total collecting area of 4650 cm^2 at 1 keV, it provides more sensitivity than *Chandra* with the trade off of less imaging resolution (¿6" full width half maximum). Each telescope focuses to a CCD detector (Figure 5.2) provided by the European Photon Imaging Camera Consortium (EPIC). Two of the detectors are metal-oxide semiconductor CCDs while the third is a pn-CCD (Seward & Charles (2010)). The two types of CCD detectors achieve a spectral resolution of 70

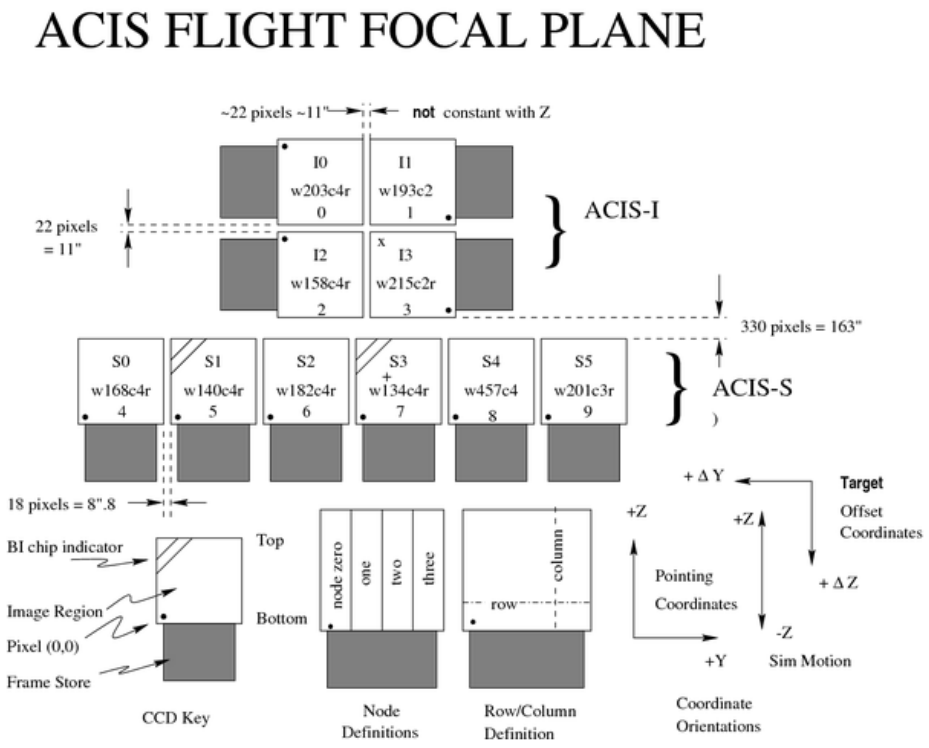

Figure 5.1: Schematic layout of the ACIS-I and ACIS-S CCD Chips onboard the *Chandra X-ray Observatory*. Image from Chandra IPI Teams (2018).

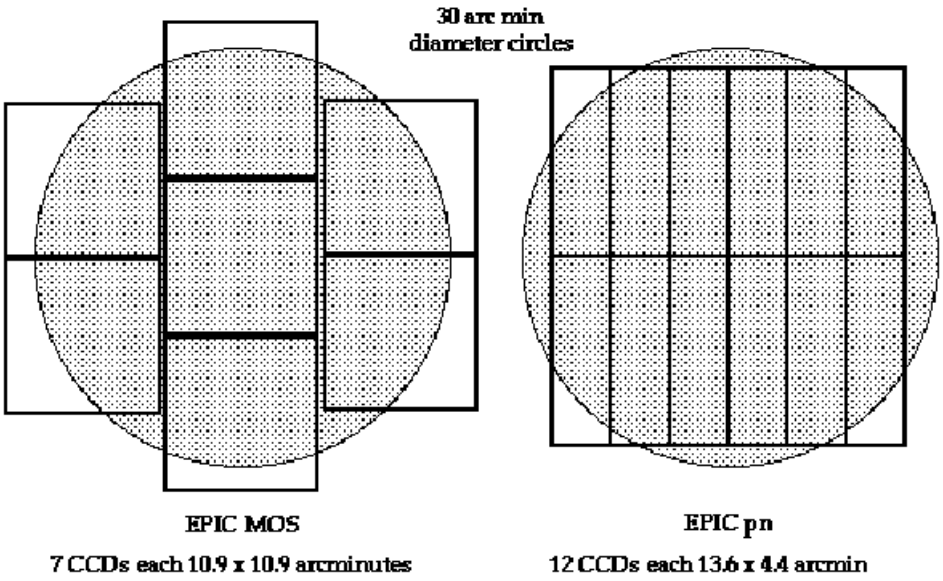

Figure 5.2: Schematic layout of the CCD chips in the MOS and PN detectors of *XMM-Newton*. Image from ESA: XMM-Newton SOC (2019).

and 80 eV and timing resolution of 1.75 ms and 0.03 ms respectively (ESA: XMM-Newton SOC (2019)).

5.3 Data Analysis

Data acquired from a major X-ray observing satellite has generally been pre-processed and stored in Flexible Image Transport System (FITS) format (Pence et al. (2010)). This includes a header which lists details covering observation information and file history, followed by multi-dimensional arrays containing the data. FITS files may be manipulated with the HEASARC

FTOOLS[1] (Blackburn (1995)). Prior to data analysis, the observations need to be reprocessed with the latest calibration files to filter for good time intervals and remove bad pixels. *Chandra* has dedicated processing software: The Chandra Interactive Analysis of Observations[2] (CIAO) (Fruscione et al. (2006)). *XMM-Newton* likewise has the Science Analysis System[3] (SAS).

5.3.1 Image Representation

Data tables in FITS files may be displayed as images using visualization software such as SAOImageDS9 (Joye & Mandel (2003)). Images are created by displaying the number of photons detected per pixel when the data is listed in sky coordinates. These are different from detector coordinates since during the course of an observation the pointing of the telescope will move slightly in random directions. This motion is known as "dithering". Several observations may be "stacked" to create a merged image in order to reveal faint features. Flux images attempt to correct for varying detector response with position and photon energy, and correct effective exposure for chip gaps or varying detector orientations and spatial coverage in stacked observations.

[1] https://heasarc.gsfc.nasa.gov/ftools/
[2] http://cxc.harvard.edu/ciao/
[3] https://www.cosmos.esa.int/web/xmm-newton/sas

5.3.2 Spectra Extraction

Once an image is created, spectra may be extracted from a region of interest. The observation data table is filtered into energy channels to create a histogram. Not all of the photon counts will be from the source target however, so a background region is specified and filtered similarly. Additional files are needed to interpret the spectra. A perfect source with singular energy will appear spread out over the detectors energy resolution. This is modelled by the redistribution matrix file (RMF). The auxiliary response file (ARF) contains the combined telescope/detector effective area and quantum efficiency as a function of energy. For spatially extended sources, the effective area and efficiency may vary with position on the detector. Weighted ARFs are calculated using the corresponding observatory software. The final output spectra is obtained by subtracting the background spectrum (normalized in exposure time and area to the source region) from the source spectrum.

5.4 Spectral Fitting

The observed spectrum consists of counts within detector channels C_I and is related to the true source spectrum $f(E)$ through:

$$C(I) = \int f(E)R(I,E)dE. \tag{5.1}$$

$R(I, E)$ is the detector response which is related to the probability that a photon with a given energy will be detected in channel I. A model of the source spectrum $f(E)$ is selected based on physical arguments and used to generate the predicted counts in each channel $C_p(I)$. The goodness of fit is measured by the fitting statistic. The most common choice is χ^2 defined as:

$$\chi^2 = \sum \frac{(C(I) - (C_p))^2}{\sigma(I)}, \tag{5.2}$$

where $\sigma(I)$ is the error in the number of counts in channel I and is usually estimated as $\sqrt{C(I)}$. The parameters describing $f(E)$ are modified by an optimisation algorithm to minimize the χ^2 statistic (Arnaud, K. and Gordon, C. and Dorman, B. (2018)). The reduced χ^2 given by $\frac{\chi^2}{\nu}$ where ν is the number of degrees of freedom (number of channels – number of model parameters) should approach 1 for a good fit while a value much less than 1 indicates that the errors have been overestimated (Bevington & Robinson (2003)). The final judgement must be made by scientific reasoning as depending on the quality of the data, many models may be fit adequately to a given spectrum.

5.5 XSPEC

The standard X-ray spectral fitting software used by the astronomical community is XSPEC[4] (Arnaud (1996)). It is detector independent and requires

[4] https://heasarc.gsfc.nasa.gov/xanadu/xspec/

the input and background spectra, and associated RMF and ARF detector response files. The optimization method used is a modified Levenberg-Marquardt algorithm based on CURFIT from Bevington (1969). Confidence intervals are calculated by fitting the remaining parameters with the parameter of interest frozen. The value of the parameter is then varied until the χ^2 statistic exceeds a critical value (dependent on the number of free parameters and the error level desired)

5.5.1 XSPEC Models

The XSPEC models for the various emission mechanisms used in this work (and introduced in Section 2.3) are detailed below, with examples of each shown in figure 5.3.

Power-law

The spectrum of non-thermal synchrotron radiation (Section 2.2) follows a power-law:

$$A(E) = KE^{-\alpha} \tag{5.3}$$

where K is the normalization in units of photons/keV/cm^2/s at 1 keV, E is the photon energy, and α is the dimensionless photon index.

Blackbody

The emission from a hot dense object follows the blackbody (Section 2.3.3)

spectrum:

$$A(E) = K\frac{8.0525E^2dE}{(kT)^4(e^{E/kT}-1)} \tag{5.4}$$

where K is the normalization given by L_{39}/D_{10} (the luminosity of the source in units of 10^{39} erg/s at a distance of 10 kpc), kT is the temperature in keV (Arnaud, K. and Gordon, C. and Dorman, B. (2018)).

VPSHOCK

Plane-parallel shocked plasma model from Borkowski et al. (2001) which includes thermal bremsstrahlung (Section 2.3.1) and line emission (Section 2.3.2) components. The free parameters are the plasma temperature kT (keV), elemental abundances of He, C, N, O, Ne, Mg, Si, S, Ar, Ca, Fe, and Ni with respect to solar, the upper limit on the ionization timescale (s/cm^3), and normalization in units of $(10^{-14}/D^2)\int n_e n_H dv$ where D is the distance (cm), n_e and n_H are the electron and hydrogen number density (cm^{-3}).

Tuebingen-Boulder ISM absorption model (tbabs)

The incredibly sparse interstellar medium (ISM) can not be neglected when analyzing X-ray data. While the density averages only $\sim 1/\text{cm}^3$, this is enough to noticeably absorb or scatter soft X-rays. The transmission of the ISM follows $e^{[-\sigma N_H]}$, where σ is the photoelectric absorption coefficient, and N_H is the number of H atoms in the 1cm^2 column along the line of sight to the source. The cross-section varies roughly as $\sim Z^3/E^3$ such that the effect is much larger

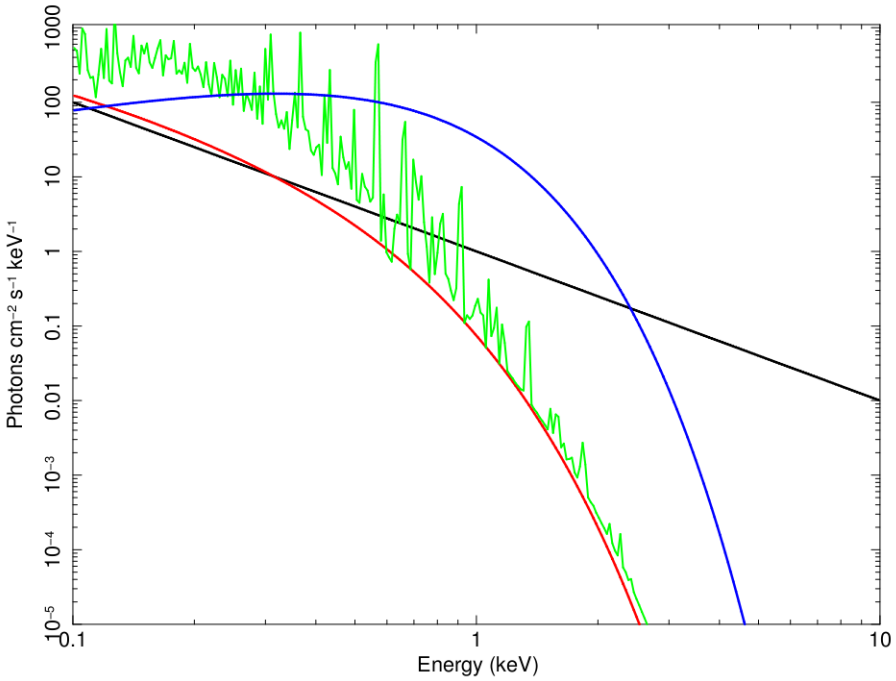

Figure 5.3: Examples of the common emission models introduced in Section 2.3. Power-law with $\alpha = 2$ (Black), Thermal bremsstrahlung with kT=0.2 keV (Red), PSHOCK with kT=0.2 keV and $n_e t = 10^{11}\text{cm}^{-3}\text{s}$ (Green), and Blackbody with kT=0.2 keV (Blue).

at low energies. Individual elemental species contribute different absorption profiles. Modelling the abundances of the ISM is therefore an important aspect to understanding the total absorption profile. For this work we assume the abundances from Wilms et al. (2000a) and model the absorption using the Tuebingen-Boulder ISM absorption model (tbabs). This model has one free parameter N_H, the column density, and is described in units of 10^{22} atoms/cm^2. The effect of different column density values is shown in Figure 5.4.

5.6 Spectral Maps

Traditional imaging techniques such as RGB images where X-ray observations are filtered into soft, medium, and hard energy bands and coloured as red, green, and blue respectively, are useful for identifying regions of thermal emission such as SNR shells. Non-thermal emission which does not decline rapidly at higher energies (see Figure 5.3) will not show significant detail with this technique. Consider a stove-top element which has cooled to the point where it is no longer glowing red. While a traditional colour image hides the fact that contact with the element would still result in burns, the image from a thermal imaging camera which displays temperature instead of brightness will tell a different story. It is similarly enlightening to visualize the change in photon index across a PWN. To do this, we use an adaptive binning algorithm to generate regions which are then coloured to reflect the best fit parameter values.

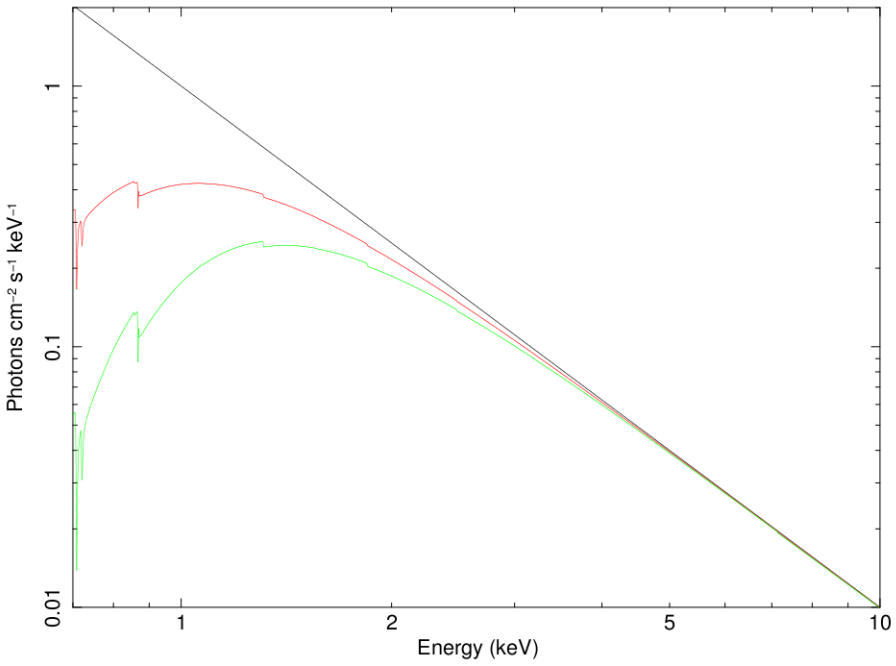

Figure 5.4: Effect of the interstellar medium along the line of sight. All 3 models are power-laws with photon index $\alpha = 2$ and different column density values: 0 (black), 0.5 (red), and 1 (green) with units of 10^{22}cm^{-2}.

5.6.1 Contbin

Contbin[5] is an adaptive binning routine developed by Sanders (2006). This algorithm follows the surface brightness of an input image and generates puzzle like pieces which fit together to cover the image, while individually meeting some specified signal limit. The routine begins by selecting the brightest unbinned pixel in the image and iterating over the neighbouring pixels, adding in the next brightest unbinned pixels counts until either the desired threshold is reached, no free neighbours remain, or additional constraints such as a maximum region length is exceeded. After this first pass, many regions exist which do not meet the desired statistic. The edge pixels of these regions are redistributed to the neighbouring bin whose own edge pixels brightness are closest in value. This process repeats until no bins with less than the desired number of counts remain. Spectra are then extracted from each region and fit with the desired model. Maps are then generated where the regions are each coloured with the best fit value of the chosen parameter. Figure 5.5 shows an example of this process applied to a *Chandra* X-ray observation of the supernova remnant G54.1+0.3 to generate a map of the photon index called a spectral map.

[5] https://www-xray.ast.cam.ac.uk/papers/contbin/

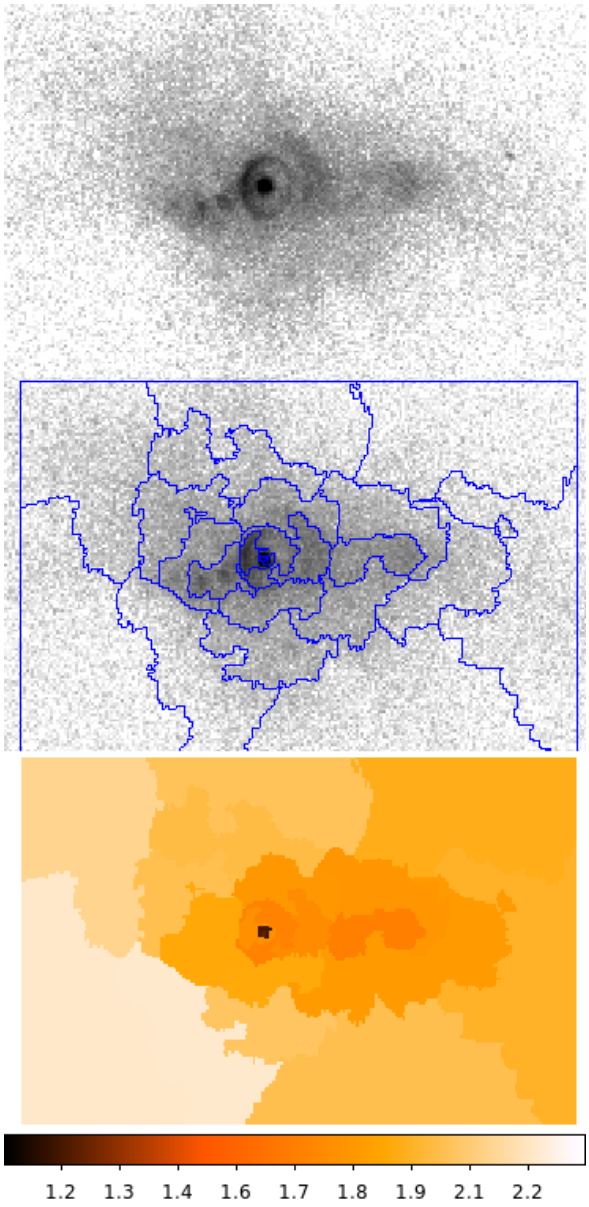

Figure 5.5: Top: *Chandra* X-ray observation of G54.1+0.3 displayed as a counts image. Middle: Regions generated by *Contbin* (Section 5.6.1). Bottom: Spectral map showing the best fit value of the photon index for each of the generated regions.

Chapter 6

G21.5–0.9

The first remnant we study is G21.5–0.9. This is a young nearly circular remnant which for many years was identified as a member of the naked PWN class in that while the PWN was visible in radio and X-ray, the surrounding shell of material predicted from a supernova explosion was not observed at any wavelength. The bright PWN has been used as a calibration target for many X-ray missions and as a result has been observed often through the lifetime of the *Chandra X-ray Observatory*. This wealth of observations allowed for detailed studies which revealed limb-brightening of the shell (Matheson & Safi-Harb (2010)). This confirmed the extended emission as a SNR shell opposed to purely a dust scattering halo effect (Bocchino et al. (2005)). In analysing the spectrum of the shell, they were unable to identify its nature as thermal or non-thermal.

With the addition of new released data we identify the nature of the limb-brightened emission as requiring a two component thermal and non-thermal

model. We are then able to estimate the density of the surrounding medium, and through this derive the predicted explosion energy.

We constrain the abundances in the northern knot of thermal emission, finding enhanced abundances relative to solar indicating its ejecta origin, and fit the radial profile of the PWN spectrum with a diffusion model of the wind. The following contains text and images published in Guest, B., Safi-Harb, S., & Tang, X., *The Deepest Chandra Study of the Plerionic Supernova Remnant G21.5–0.9*, Monthly Notices of the Royal Astronomical Society, 842, 1, 2019.

6.1 Introduction

G21.5−0.9 is a composite, young plerionic SNR which displays a limb-brightened shell (Matheson & Safi-Harb (2005)) and a central PWN. The PWN is significantly brighter than the surrounding shell and has been well studied at radio wavelengths. The initial mapping was done in the 1970's. Becker & Kundu (1976) and Wilson & Weiler (1976) found a flat spectral index with $S_\nu \propto \nu^{-\alpha}, \alpha \sim 0.1$ and a strongly polarized elliptical brightness distribution which is peaked near the geometric centre, similar to the Crab Nebula and 3C 58. The first X-ray observations were taken with the Einstein Observatory. Becker & Szymkowiak (1981) found the X-ray emitting region is comparable to the radio size. Furst et al. (1988) suggested a symmetric double cone outflow structure, based on 22.3 GHz observations.

The launch of *Chandra* and *XMM-Newton* in 1999 revealed X-ray structure beyond the PWN. A 150" radius halo was observed surrounding the PWN with knots of enhanced emission to the north (Slane et al. (2000); Safi-Harb et al. (2001); Warwick et al. (2001)). The X-ray halo was found to have a non-thermal spectrum and was interpreted as either an extension of the PWN or a dust scattering halo (Safi-Harb et al. (2001); Bocchino et al. (2005)). There were problems with both of these interpretations. The X-ray PWN exceeding that seen in radio did not fit with evolutionary models and dust scattering alone could not account for the excess emission from the knots. Bandiera & Bocchino (2004) achieved a good fit to the diffuse emission with a dust scattering model and found evidence of a thermal component in the northern knot. Matheson & Safi-Harb (2005) combined available *Chandra* observations to reveal a candidate shell with limb-brightening observed at the eastern edge of the halo. The power-law photon index increased from the centre of the PWN to the edge, then remained flat within the halo out to a radius of 150″. Bocchino et al. (2005) analysed *Chandra* and *XMM-Newton* data and interpreted the diffuse halo as a result of scattering off foreground dust and the northern knot as shock-heated ejecta. Matheson & Safi-Harb (2010) extended their previous work with additional *Chandra* observations and found the knot required a thermal component supporting the ejecta assumption, while the limb was equally fit with non-thermal and thermal models. The non-thermal interpretation of the limb implied particle acceleration at the shock out to

TeV energies. Matheson & Safi-Harb (2010) also found the first evidence of variability in the PWN and weak thermal X-ray emission from the neutron star.

Radio pulsations from PSR J1833-1034 were detected independently by Gupta et al. (2005) and Camilo et al. (2006) who found a period of 62 ms, $\dot{P} = 2.0 \times 10^{13}$, surface magnetic field of $B = 3.6 \times 10^{12}$ G, characteristic age of 4.8 kyr, and spin-down luminosity of $\dot{E} = 3.3 \times 10^{37}$ erg s^{-1}. Bietenholz & Bartel (2008) combined Very Large Array (VLA) observations from 1991 and 2006 to estimate a PWN expansion age of 870^{+200}_{-150} yr[1], which makes the remnant one of the youngest Galactic PWNe behind G29.7-0.3 with age estimates of about 400 years (Gelfand et al. (2014); Reynolds et al. (2018)). The shell remains undetected at radio wavelengths (Bietenholz et al. (2011)).

At higher energies, G21.5−0.9 has been detected by INTEGRAL in the soft γ-ray band 17-200 keV (Terrier et al., 2004; de Rosa et al., 2009), who found the PWN was dominant in the hard X-ray band, while H.E.S.S. observations showed the PSR J1833–1034 was the main source in the γ-ray band, with a 1–10 TeV flux of 2% that of the Crab. Abdo et al. (2013) detected γ-ray pulsations with the Fermi Large Area Telescope (LAT). Tsujimoto et al. (2011) used G21.5−0.9 data to conduct a cross-calibration study of the instruments onboard *Chandra*, *Suzaku*, *Swift*, *XMM-Newton*, *INTEGRAL* and *RXTE*. Nynka et al. (2014) used NuSTAR observations up to 40 keV and found evidence of the knot

[1]This age estimate neglects the expected acceleration that could increase the age by 20–25%.

and limb features indicating non-thermal emission processes, with a break at 9 keV in the PWN spectrum. This break was most recently refined to 7.1 keV using *Hitomi*'s broadband coverage (Aharonian et al. (2018)).

The distance to the SNR has been estimated by several authors to be in the 4.3–5.1 kpc range (e.g., Safi-Harb et al. (2001); Camilo et al. (2006); Bietenholz & Bartel (2008); Kilpatrick et al. (2016)). A kinematic distance of 4.8 kpc was also proposed by Tian & Leahy (2008). In this paper we adopt a distance of 5 kpc and refer to D_5 as the distance in units of 5 kpc.

6.2 Observations

As a calibration target for the *Chandra* X-ray observatory, G21.5–0.9 was observed regularly by both the Advanced CCD Imaging Spectrometer (ACIS) and the High Resolution Camera (HRC). Recently, Matheson & Safi-Harb (2010) analyzed 578.6 ks (1999-2006) of ACIS observations to study limb-brightening in the eastern limb and search for thermal emission. In this work, we extend this study utilizing 86 ACIS observations totaling of 786.1ks (1999-2014) and 17 HRC observations with totalling of 306.1ks. Data processing was performed using the *Chandra* Interactive Analysis of Observations (CIAO) software package (Fruscione et al. (2006)), while spectral analysis made use of the X-ray Spectral fitting package XSPEC version 12.9.1 (Arnaud (1996)).

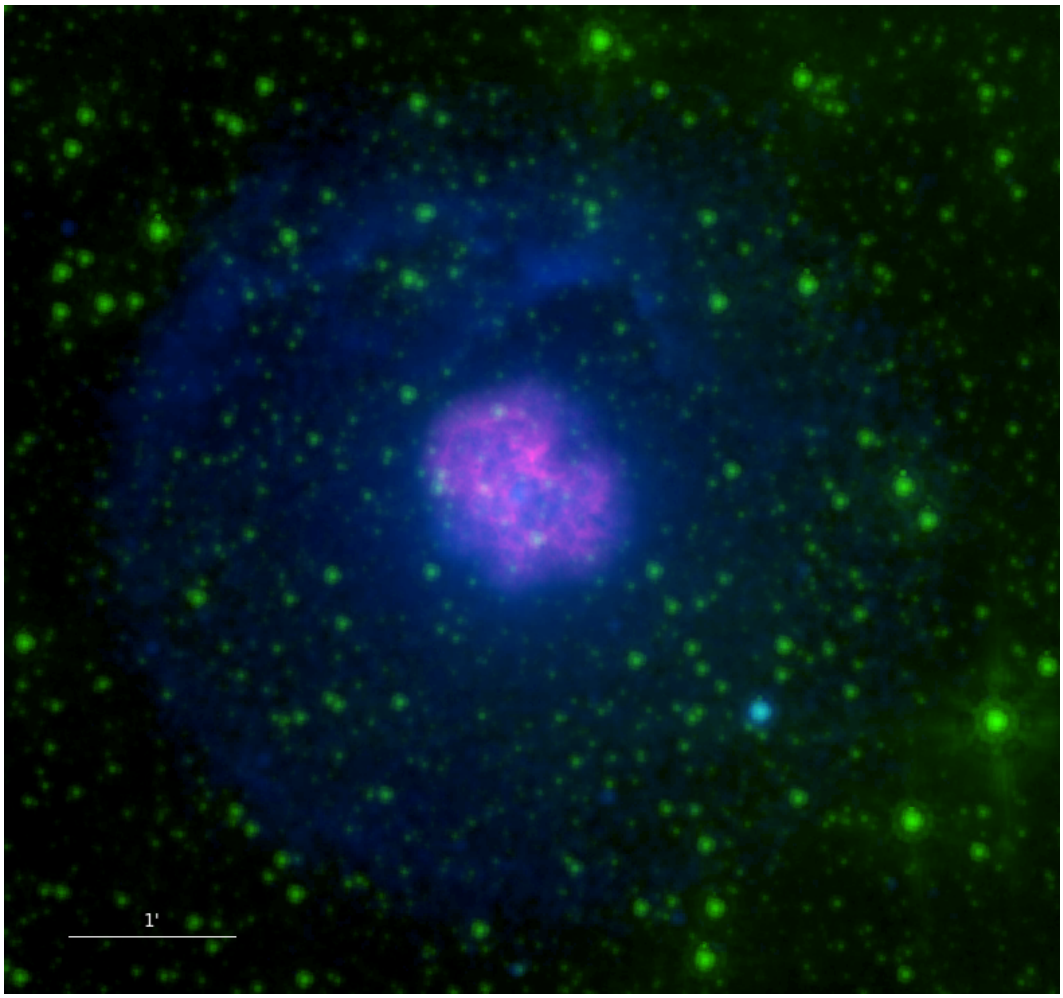

Figure 6.1: Multi-wavelength image of G21.5−0.9. From *Chandra*: 0.5–10 keV (Blue), VLA: 4.75 GHz (Pink) from Bietenholz & Bartel (2008), Spitzer: 5.8 microns (Green) Zajczyk et al. (2012). Note the 4.75 GHz data covers only the central PWN.

6.2.1 Structure

A multi-wavelength image is shown in Figure 6.1. The remnant G21.5−0.9 is dominated by a bright PWN (visible from radio (pink) through x-ray (blue)), which is 40″ in radius, centered at $\alpha(2000) = 18^h33^m33.37^s$, $\delta(2000) = -10^o34'06".25$ and powered by the central pulsar PSR J1833–1034. The diffuse emission is only revealed by deep x-ray observations, extends to a radius of 150″ and displays a limb-brightened eastern edge. Knots with enhanced soft x-ray emission appear to the north and merge with the limb-brightened edge to the east. The diffuse emission fills a circle coincident with the geometry of the limb-brightened eastern edge, but the additional ∼ 200ks of ACIS data still do not reveal limb-brightening to the west. The diffuse emission merely blends with the background level. Point source SS 397 is located to the south west within the extended shell. Zajczyk et al. (2012) found infrared emission (green) from the inner 4″ but no extended emission at larger scales with the dominant contribution from field stars.

6.2.2 Brightness Profile

The presence of a dust scattering halo complicates analysis of the faint outer regions identified as the supernova shell. We use the wealth of observations to update the surface brightness profiles of Bocchino et al. (2005) and Matheson & Safi-Harb (2005). Profiles were extracted from quadrants of the merged event file and filtered into 4 energy bands: 0.3–1.5, 1.5–3, 3–5, and 5–8 keV. The results are shown in Figure 6.2. The bottom left quadrant shows the limb brightened edge revealed by Matheson & Safi-Harb (2005), the brightest knot is clearly visible in the top right profile. The

top left shows the contribution from the fainter knot structures and the bottom right which displays no limb brightening smoothly declines to the background level.

6.3 Spectroscopy

6.3.1 Processing

Weighted spectra were extracted for each observation using the CIAO routine specextract. Each spectrum has an associated background which is extracted from the same CCD chip, but outside the shell and is not overlapping with any regions listed in the *Chandra* Source Catalogue. The observations were processed with the CIAO 4.7 Chandra-repro script and is fitted simultaneously without merging the individual spectra as recommended by the *Chandra* X-ray Center. The fitting was performed with the X-ray Spectral analysis software XSPEC v12.9.1 over the range 0.5–8 keV.

6.3.2 Detector Contamination

Since the observational data are taken many years apart, we checked if the changing response affected our results. The build up of contaminants has a stronger effect on low energy emission (Marshall et al., 2004), which is likely to affect the derived column density. To explore a systematic change in this parameter, we extract spectra from the PWN, group them by year of observation and fit individually to an absorbed power-law. We adopt the Tuebingen-Boulder ISM absorption model (TBABS in XSPEC), which calculates the cross-section for X-ray absorption. The required ISM

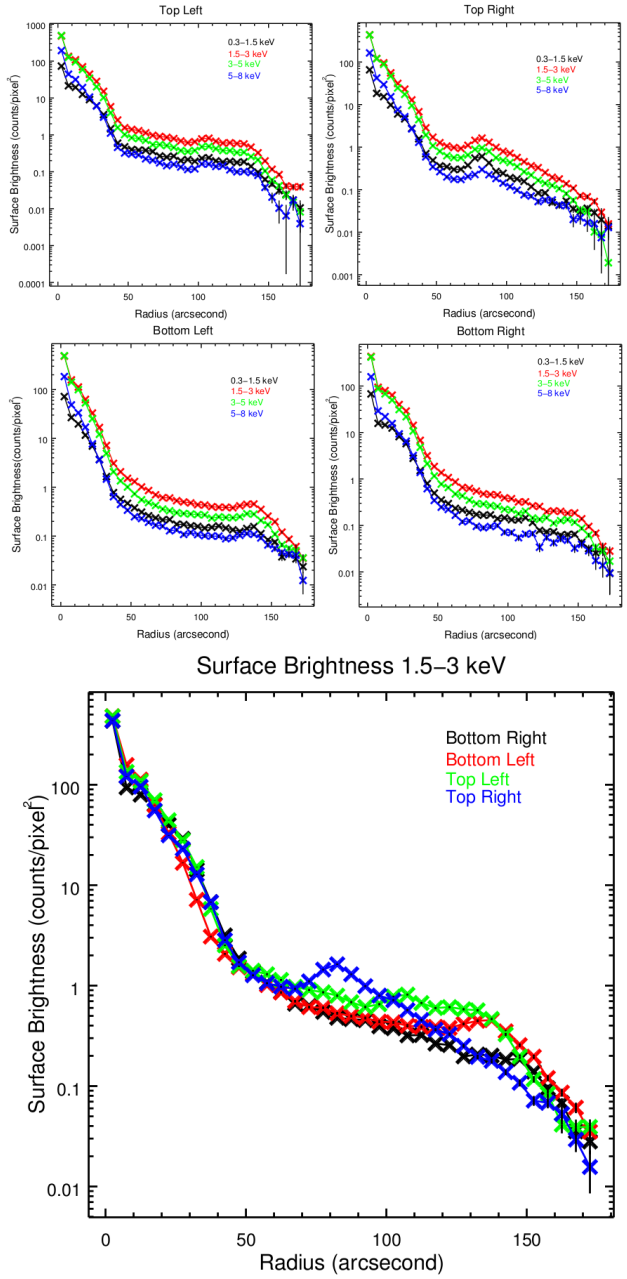

Figure 6.2: Upper panel: Surface brightness profiles of four quadrants of G21.5-0.9 at four different energy bands. Bottom panel: Overlay of the profile of each quadrant in the 1.5–3 keV band.

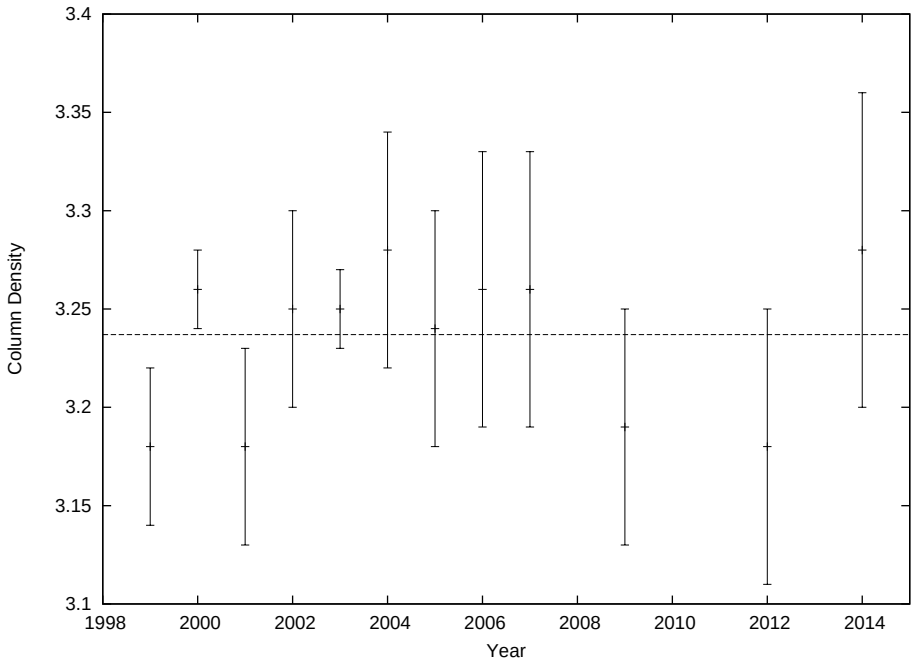

Figure 6.3: Fitting observations of the PWN grouped by year to an absorbed power-law. The column density has units of 10^{22} atoms cm^{-2}. The dotted line marks the best fit value for all observations fit simultaneously. See §3.3 for details.

abundances were set to those from Wilms et al. (2000a). The results of this analysis are presented in Fig.6.3. No general trend with increasing column density is found. Therefore, in what follows, we use the single best-fit value estimated with the total simultaneous fit in section 6.3.3.

Table 6.1: Spectral-fitting results for the pulsar wind nebula[a]

$N_H(10^{22}$ atoms cm$^{-2})$	3.237 (3.225 - 3.250)
Γ	1.841 (1.835 - 1.847)
Norm $(10^{-2})^b$	1.886 (1.869 - 1.903)
$\chi^2_\nu(\nu)$	1.114 (26369)
Absorbed Flux (10^{-11} erg cm^{-2} s^{-1})	4.555 $\pm$ 0.005
Luminosity(10^{35} erg s^{-1})^c	2.822 $\pm$ 0.003
Effective Exposure	590.3 ks

[a] All confidence ranges are 90%. Models were fit over the range 0.5-8 keV.
[b] Units are photons keV^{-1} cm^{-2} s^{-1}
[c] Unabsorbed, assuming a distance of 5 kpc to G21.5−0.9

6.3.3 Pulsar Wind Nebula

In order to properly account for the absorption along the line of sight, spectra from the PWN were extracted from a 40″ circle centered at $\alpha(2000) = 18^h33^m33.37^s$, $\delta(2000) = -10^o34'06".25$. This was fit with an absorbed power-law with the absorption given by the TBABS model in XSPEC (see Table 1). The best fit parameter for the column density was frozen in subsequent region analysis to 3.237 $\times 10^{22}$ cm^{-2} (see section 6.3.5 for further discussion).

6.3.4 Spectral Map

To generate a photon index map, we applied the contour binning software contbin[2] (Sanders, 2006), which produces adaptive bin size following the surface brightness of an input image, such that each bin meets a given signal limit. The exposure corrected merged flux counts image spanning the range 0.5–10 keV was used as input

[2]http://www-xray.ast.cam.ac.uk/papers/contbin/

with a signal limit of 150. This corresponds to a limit of a few hundred counts in the resulting spectra for a single observation of each generated region. The spectra were fitted with an absorbed power-law and the absorption coefficient is frozen to the best fit value derived for the PWN (see section 6.3.3). The generated regions were coloured with their best fit value of the photon index, which is illustrated in Fig. 6.4. A zoomed in view of the small scale in the PWN is presented in Figure 6.5 with details. The non-symmetric nature of the emission is clearly shown in the figure, where the hardest emission is offset from the location of the PSR (marked with a cross) with a bubble of higher energy emission extending to the north.

6.3.5 Radial Profile

Spectra were extracted from rings centered on the pulsar, and fit with an absorbed power-law. The column density is found to be $3.237 \times 10^{22}\, cm^{-2}$ for the external background region selection and $3.222 \times 10^{22}\, cm^{-2}$ for the internal background selection. As shown in Fig. 6.6, the photon index is shown to increase to the edge of the PWN at $40''$, which is consistent with previous studies (e.g. Matheson & Safi-Harb 2005). However, a higher column density is derived comparing with previous work (Slane et al. 2000, Safi-Harb et al. 2001, Warwick et al. 2001, Bocchino et al. 2005, Matheson & Safi-Harb 2010) , which is likely because we apply the TBABS model with *wilm* abundances. We verify this by fitting the PWN spectra with the previously used WABS model for photoelectric absorption which uses the Wisconsin cross-sections (Morrison & McCammon (1983)) and find a smaller value of $2.37 \pm 0.01 \times 10^{22}\mathrm{cm}^{-2}$ which is consistent with previously published results. To

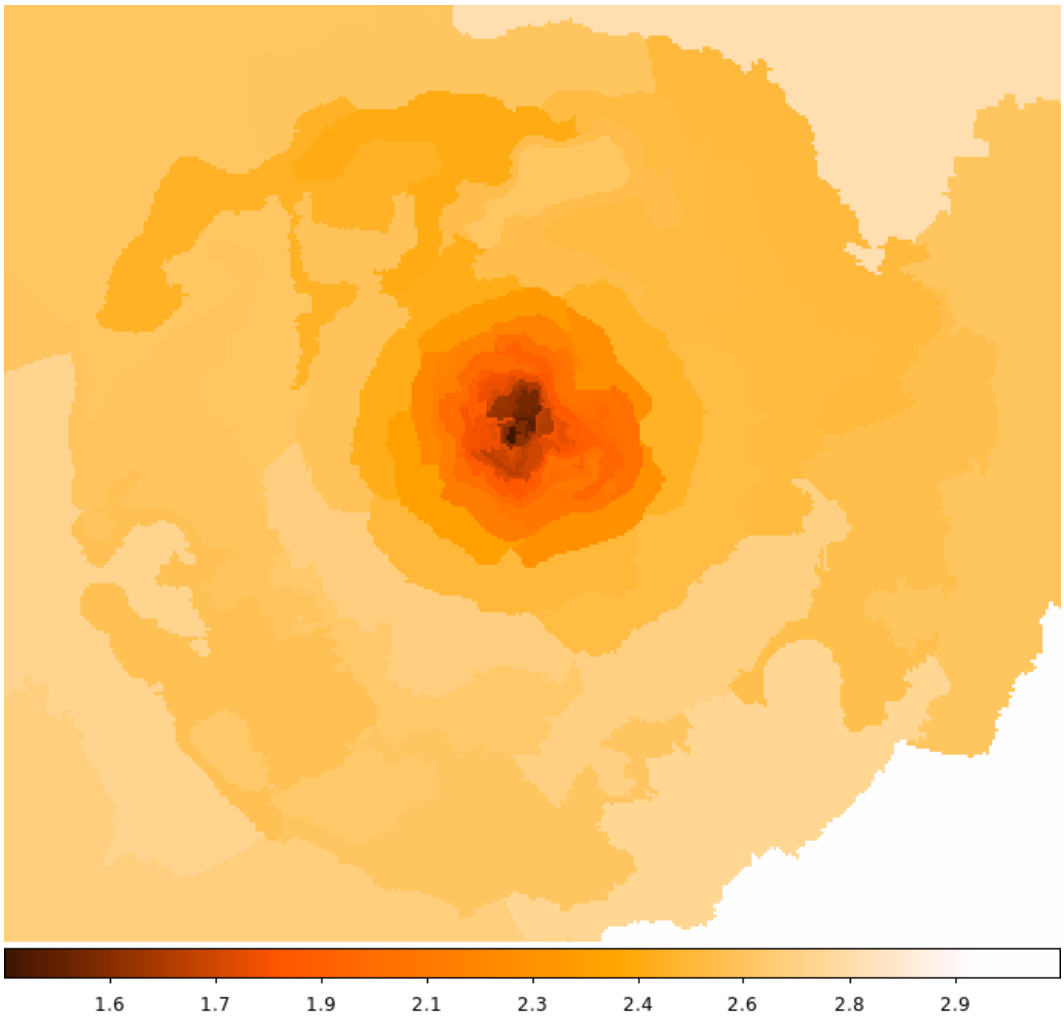

Figure 6.4: Photon index map for the entire remnant. The colourbar shows the power-law photon index, with the darker (lighter) colour reflecting a harder (softer) spectrum.

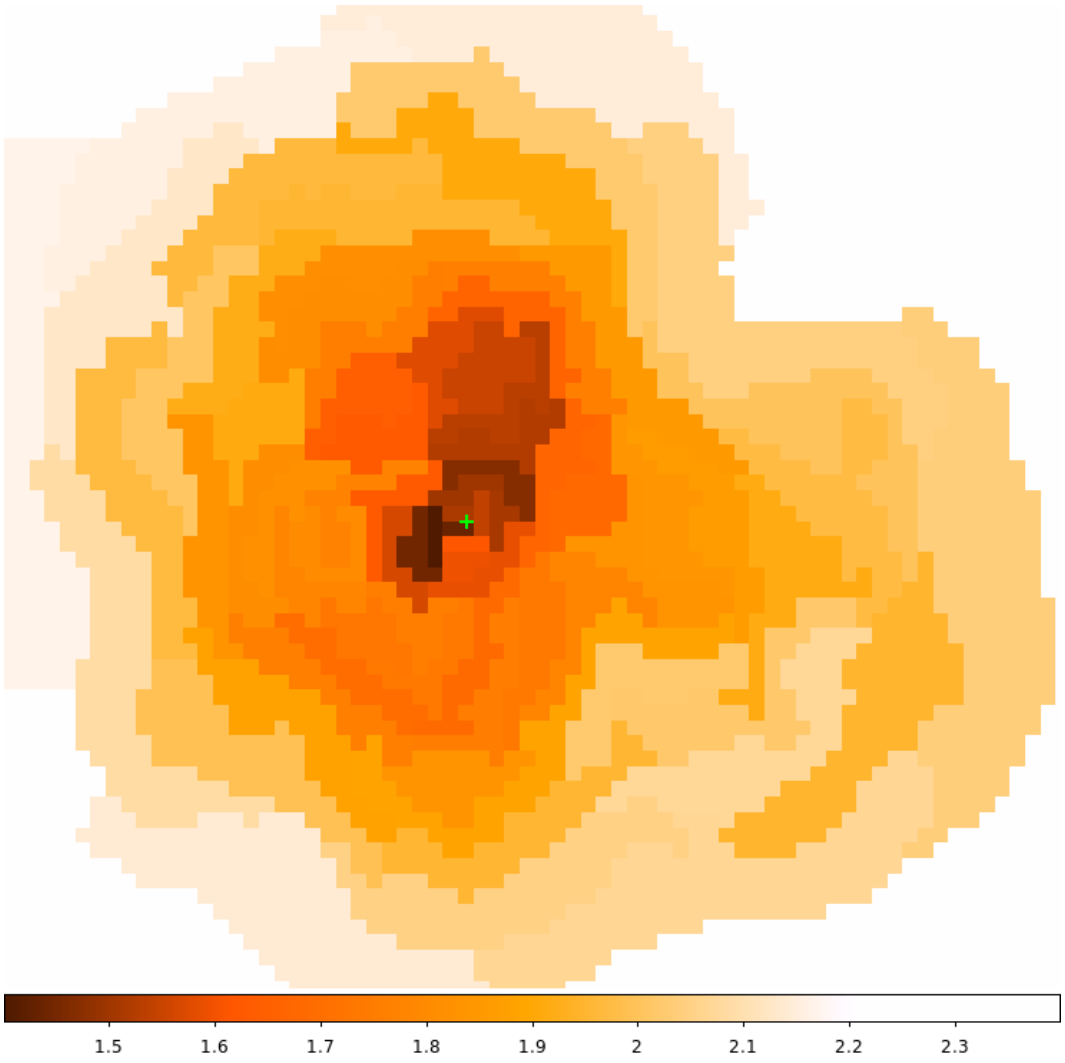

Figure 6.5: Photon index map zoomed in on the PWN. The green cross marks the position of the PSR. See §3.3.1 for details

account for the halo emission, an annulus centred on the pulsar with radius 44″–48″ was chosen as background which had a negligible effect on the spectral index. This is expected due to the drop in surface brightness outside the PWN. Figure 6.2 shows that the surface brightness where the internal background was taken is fainter by a factor of more than 20 from the inner PWN. Therefore the dust scattered halo component leads to a systematic underestimation of the photon index errors, yet the overall result will remain unchanged. Additionally, the halo contributes minimally above 5 keV (Bocchino et al. (2005)) and when we restrict our fits to the range 5–8 keV we find the trend is unchanged. The high energy profile differs in that the pulsar component is not visible in the first data-point.

The near linear increase of the spectral index with radius is consistent with that observed in other young PWNe, such as 3C 58 (Slane et al. (2004)). The spectral index continues to rise beyond the edge of the PWN at 40″, which reaches a maximum at 50″ and remains roughly flat to the edge of the remnant, see Figure 6.7. The model fitting of the spectral index profile will be discussed in detail in section 6.5.2. We include the best fit power-law parameters in the appendix to assist with future modeling work (see Tables A1-A4), and in spatially resolved spectroscopic studies of the whole remnant, including the halo and shell emission.

6.3.6 PSR J1833–1034

Evidence of weak thermal x-ray emission from the pulsar powering $G21.5-0.9$ has been suggested (Matheson & Safi-Harb 2010). To follow up on this study with the deeper exposure, we select a 2″ radius centred on the pulsar at $\alpha(2000) =$

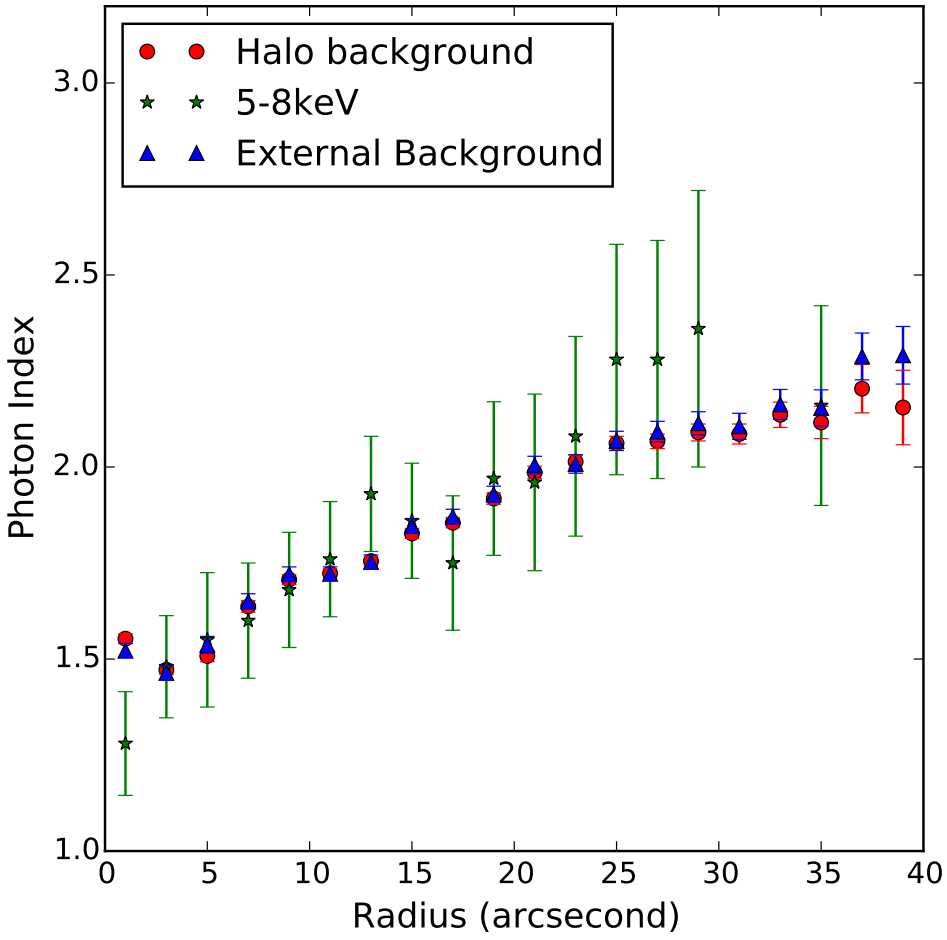

Figure 6.6: Photon index found for rings of increasing size within the central bright PWN. The External (triangles, blue symbols) and Halo (circles, red symbols) background profiles correspond to the 0.5–8 keV bands and use a background region outside and from within the halo, respectively. The 5–8 keV profile (stars, green points) also use the internal background, which is an annulus centred on the pulsar with a radius of 44″–48″ to minimize contribution from the dust scattering halo. Errorbars on the photon index are at the 90% confidence level.

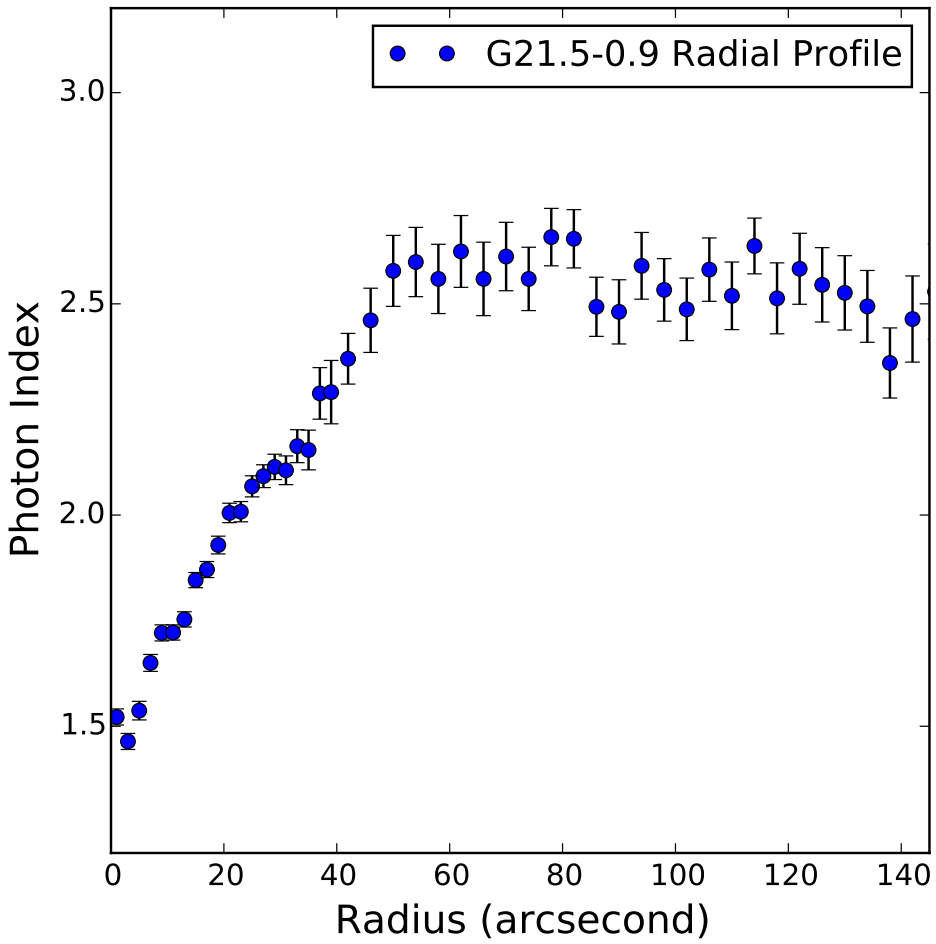

Figure 6.7: Spectral index vs radius fit for the entire remnant over 0.5–8 keV, with the absorption frozen to the best fit value found from fitting the PWN. The northern knot region coincides with the slight increase at 80″ and the limb-brightened edge of the remnant corresponds to the drop at 140″.

$18^h33^m33.54^s$, $\delta(2000) = -10^o34'07.6$" using observations with an off-axis angle less than $3'$[3]. The background was extracted from a circular annulus centred on the PSR with radius $2''$– $4''$ to remove contamination from the PWN. The spectra were fitted with an absorbed power-law utilizing the best fit column density in the PWN. The fitting results are provided in Table 6.2, and a combined spectrum is shown in Figure 6.8. The single power-law model derives a hard spectral index $\Gamma = 1.54 \pm 0.02$ with $\chi^2_\nu(\nu) = 1.075(3731)$. The addition of a thermal blackbody component improves the fit slightly, which yields a harder spectral index $\Gamma = 1.35 \pm 0.12$ with temperature $kT = 0.43^{+0.04}_{-0.09}$ keV and $\chi^2_\nu(\nu) = 1.072(3729)$. F-test is a statistical measure of the requirement of an additional model based on improvement in the reduced chi-squared value vs the change in the number of degrees of freedom. We find that the thermal component is required over a power-law alone with an F-test probability of 7.6×10^{-3}. This is notably less significant than the previous result by Matheson & Safi-Harb (2010), which found a probability of 2.6×10^{-4}.

6.3.7 Northern Knot

The bright knot to the north of the PWN appears as a region of enhanced soft X-ray emission. Previous studies suggested a two-component model with both thermal and non-thermal emission. However, the thermal emission component was not well constrained. Bocchino et al. (2005) found evidence for thermal emission in the 'North Spur', which is characterized by a two-component power-law plus vnei

[3]90% of the energy of a 1.5 keV point source is contained within a radius of $1''.5$ at an off axis angle of $3'$

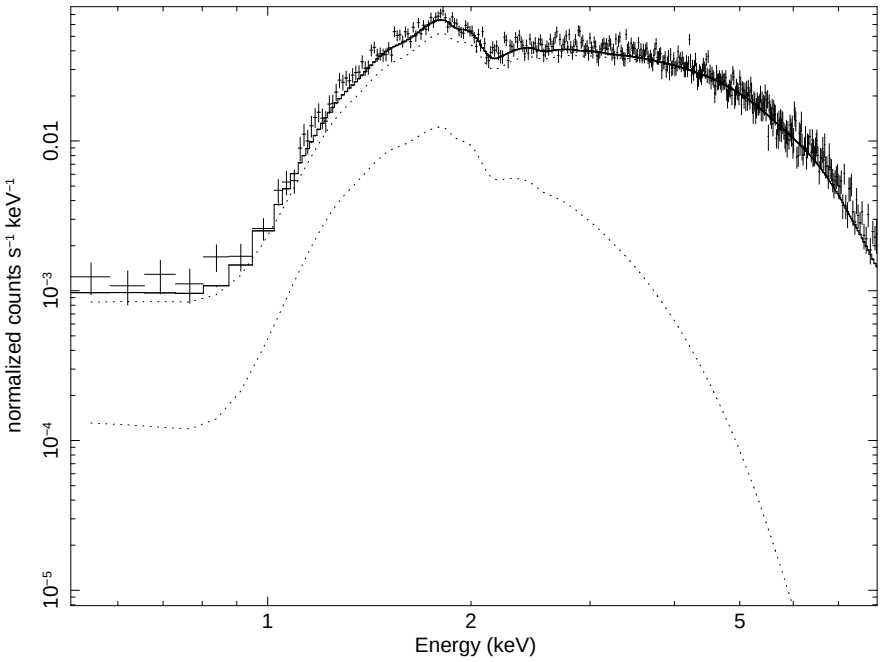

Figure 6.8: Combined spectra of the PSR with the simultaneous model fit (solid line), power-law and blackbody components (dashed lines).

Table 6.2: Spectral-fitting results for PSR J1833–1034.

Model	Model Parameter	PSR
	Effective Exposure	280.2 ks
Power-law	$N_H(10^{22}$ atoms cm$^{-2})$	3.237 (Frozen)
	Γ	1.54 (1.52 - 1.56)
	Norm $((10^{-4})^a)$	8.34 (8.13 - 8.57)
	$\chi^2_\nu(\nu)$	1.075 (3731)
	Flux $(10^{-12})^b$	3.19 $\pm$ 0.02
Power-law	$N_H(10^{22}$ atoms cm$^{-2})$	3.237 (Frozen)
+	Γ	1.35 (1.23 - 1.46)
Blackbody	Norm $((10^{-4})^a)$	6.14 (5.04 - 7.08)
	kT (keV)	0.43 (0.34 - 0.47)
	Norm $((10^{-6})^c)$	5.74 (2.89 - 8.68)
	$\chi^2_\nu(\nu)$	1.072 (1421)
	Flux $(10^{-12})^b$	3.16 (3.13 - 3.18)
	Thermal flux$(10^{-13})^b$	1.18
	Non-thermal flux $(10^{-12})^b$	3.04
	Thermal flux $(10^{-13})^d$	4.57

[a] photons keV^{-1} cm^{-2} s^{-1}

[b] Observed flux in units of erg cm^{-2} s^{-1}

[c] L_{39}/D^2_{10}

[d] Unabsorbed flux in units of erg cm^{-2} s^{-1}

model. The fitting to *Chandra* and *XMM-Newton* data produced two minima: one is consistent with solar abundances and the other with enhanced abundance of Si (2–20 times solar) and Mg (0.6–3 times solar). Matheson & Safi-Harb (2010) show the northern knot is dominated by non-thermal emission while the thermal component comprising only 6% of the observed flux. The abundances are more consistent with the solar abundances provided by Bocchino et al. with $Mg = 0.72$ (0.40–1.06), $Si = 0.84$ (0.32–1.35) although also included a large (albeit poorly constrained) abundance of Sulphur, $S = 107$ (4–210). In addition to the two-component model, we fit the data with thermal and non-thermal models separately. The results (see Table 6.3 and Figure 6.9) are consistent with the previous *Chandra* study. The thermal model requires solar abundances but a higher temperature. The addition of a non-thermal component improves the fit, meanwhile lowering the required temperature and enhancing the abundance of Si. The abundance of Si is poorly constrained and tied to the VPSHOCK normalization. When both parameters are allowed to vary, there is no plausible upper limit found on the Si abundance; however the lower limit is still characteristic of enhancement. In order to place plausible constraints on the abundance, the normalization of the VPSHOCK model was frozen at its best fit value for the calculation of the Silicon error range. Our results are consistent with the 2nd minima discussed in Bocchino et al. (2005) and supports the interpretation of an ejecta knot of Si. Assuming the emitting volume is an ellipsoid with $V = 1.77 \times 10^{55} D_5 f cm^3$, where f is the filling factor, we estimate the density of the emitting plasma to be 42 cm^{-3}, which is significantly higher than the ambient density calculated in section 6.3.8.

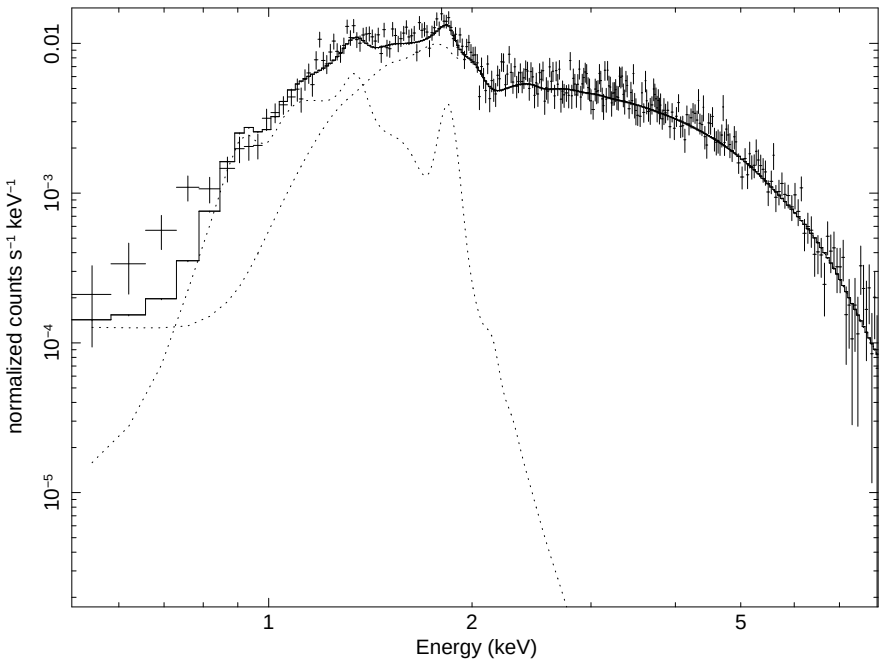

Figure 6.9: Combined Spectra of the knot plotted with the simultaneous fit result for a power-law + VPSHOCK model. See text for details.

Table 6.3: Spectral-fitting results for the northern knot. See text for details.

Model	Parameter	Northern Knot
	Effective Exposure	509.4 ks
	$N_H(10^{22}$ atoms cm$^{-2})$	3.237 (Frozen)
Power-law	Γ	2.62 (2.578-2.67)
	Norm $(10^{-4})^a$	3.67 (3.51-3.84)
	$\chi^2_\nu(\nu)$	1.306 (815)
	Flux $(10^{-13})^b$	3.12 (3.07-3.16)
vpshock	kT (keV)	4.2 (3.8-4.7)
	Mg	0.56 (0.39-0.72)
	Si	0.31 (0.24-0.39)
	S	0.16 (0.04-0.28)
	$n_{et}(10^{10}$cm^{-3} s)	2.86 (1.70-4.75)
	Norm $(10^{-4}$ cm$^{-5})$	5.04 (4.64-5.55)
	$\chi^2_\nu(\nu)$	1.062 (811)
	Flux $(10^{-13})^b$	3.33 (3.27-3.36)
Power-law	Γ	2.24 (2.17-2.31)
+	Norm $(10^{-4})^a$	2.51 (2.28-2.72)
vpshock	kT (keV)	0.15 (0.12-0.17)
	Mg	0.77 (0.35-1.72)
	Si	15.7 (7.7-26.2)
	$n_{et}(10^{13}$ cm^3 s$^{-1})$	5.0 (>0.3)
	Norm (cm^{-5})	0.102 (0.042-0.177)
	$\chi^2_\nu(\nu)$	1.041 (1178)
	Flux $(10^{-13})^b$	3.20 (3.04-3.21)
	Non-thermal flux $(10^{-13})^b$	3.05
	Thermal flux $(10^{-13})^b$	0.15
Power-law^c	Γ	2.55 (Frozen)
+	Norm $(10^{-4})^a$	2.70 (1.64-2.96)
Power-law	Γ	1.3 (0.4-2.1)
+	Norm $(10^{-5})^a$	2.0 (1.6-8.0)
vpshock	kT (keV)	0.14 (0.13-0.15)
	Mg	1.1 (0.5-1.8)
	Si	37 (5-118)
	$n_{et}(10^{13}$ cm^3 s$^{-1})$	2.7 (>0.04)
	Norm (cm^{-5})	0.14 (0.08-0.28)
	$\chi^2_\nu(\nu)$	1.041 (1176)

[a] Photons keV^{-1} cm^{-2} s^{-1}

[b] Observed flux in erg cm^{-2} s^{-1}

[c] Dust scattering halo component

The dust scattering halo complicates the analysis of the faint thermal emission. To better understand its effect on our fits we extract a background from an annulus surrounding the knot. The general result does not change. We find a power-law photon index and temperature that are consistent (within error) with the external background. The abundances show the same trend with an approximately solar abundance of Mg and an enhanced abundance of Si; however the parameters are less bound with the upper limit for Si remaining unconstrained. Alternatively, we try adding an additional power-law component with its photon index fixed to the value at which the radial profile (see Figure 6.7) appears to level off, and allow the normalization to vary. Again, the thermal parameters are consistent with the previous result. A harder photon index of 1.3 is found for the non-thermal component yet this addition does not improve the fitting statistic (see Table 3).

6.3.8 Eastern Limb

The nature of the extended emission surrounding the central PWN in G21.5−0.9 has been a puzzle since the first *Chandra* observations (Slane et al. (2000); Safi-Harb et al. (2001)). Models including dust scattering and shock heated ejecta have been proposed. Imaging analysis by Matheson & Safi-Harb (2010) found limb-brightening along the south eastern edge of the remnant, concluding that the dust scattering halo could not account for the total extended emission. Spectral analysis found an unreasonably high temperature for the emission to be purely thermal, which implied particle acceleration rather than shock-heated ejecta (Matheson & Safi-Harb 2010). Nynka et al. (2014) found an excess of emission above 10 keV in the direction of the

eastern limb with NuSTAR data, which further support the non-thermal model. Our results are presented in Table 6.4, with a combined spectra shown in Figure 6.10. The spectrum is best explained with a two-component power-law plus PSHOCK model. The emission is primarily non-thermal and the thermal component contributes only 3.5% of the total flux. Although the thermal contribution is small, it is statistically required with a F-test probability of 2.7×10^{-11}. No emission lines are observed and the thermal component is characterized by a temperature $kT = 0.37$ keV and small ionization time-scale $n_{et} = 6.57 \times 10^9$ cm^{-3} s (see Table 6.4). For a limb emitting volume of $6 \times 10^{56} D_5^3 f cm^3$, where f is the filling factor, the small amount of thermal emission suggests an emitting density of 1.76 cm^{-3}. The explosion energy implications of this density are further discussed in section 6.5.3.

In order to decouple the scattered halo emission from the limb itself, we extract a background from just inside the limb, with a similar treatment to the northern knot. However the limb brightening is not significant enough to provide robust statistics. Instead we add a power-law component with the photon index fixed to the leveled off value from the radial profile and allow the normalization to vary. With this added non-thermal component we again find a faint thermal contribution with temperature of 0.23 keV (Table 4) - consistent within error of our non-halo result and a photon index of 1.5. Again, the added component does not improve the fitting statistic.

6.4 Variability in the Pulsar Wind Nebula

Bright Knots, which appear and fade away on time-scales of weeks to months with velocities of $\sim 0.5c$, have been observed in PWNe such as the Crab and Vela nebulae

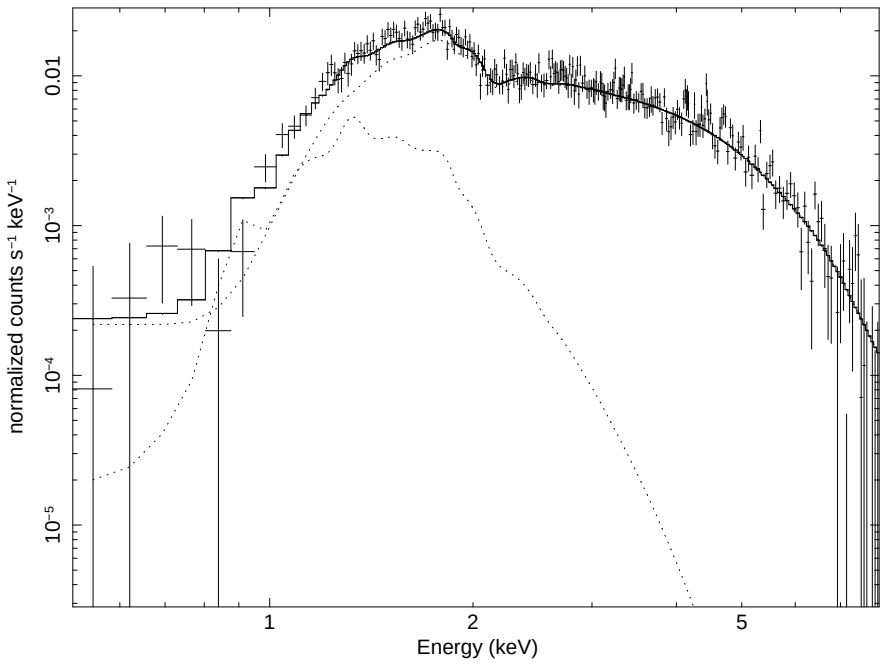

Figure 6.10: Combined Limb spectra plotted with the simultaneous fit to a power-law + PSHOCK model.

Table 6.4: Spectral-fitting results for the eastern limb. See text for details.

Model	Parameter	Eastern Limb
	Effective Exposure	318.7 ks
	$N_H(10^{22}$ atoms cm$^{-2})$	3.237 (Frozen)
Power-law	Γ	2.49 (2.44-2.54)
	Norm $(10^{-4})^a$	5.36 (5.11-5.63)
	Flux $(10^{-13})^b$	5.38 (5.32-5.45)
	$\chi^2_\nu(\nu)$	1.016 (1040)
pshock	kT (keV)	3.04 (2.85-3.37)
	$n_{et}(10^{12}$ cm^3 s$^{-1})$	2.07 (0.97-4.78)
	Norm $(10^{-4}$ cm$^{-5})$	9.73 (8.87-10.02)
	$\chi^2_\nu(\nu)$	1.177 (1039)
	Flux $(10^{-13})^b$	5.49 (5.42-5.58)
Power-law	Γ	2.22 (2.04-2.34)
+	Norm $(10^{-4})^a$	3.76 (2.90-4.41)
pshock	kT (keV)	0.37 (0.20-0.64)
	$n_{et}(10^9$ cm^3 s$^{-1})$	6.57 ($<$ 29.5)
	Norm $(10^{-3}$ cm$^{-5})$	6.21 (1.25-96.18)
	$\chi^2_\nu(\nu)$	0.966 (1037)
	Flux $(10^{-13})^b$	5.61 (5.37-5.67)
	Non-thermal flux $(10^{-13})^b$	5.41
	Thermal flux $(10^{-13})^b$	0.20
Power-law^c	Γ	2.55 (Frozen)
+	Norm $(10^{-4})^a$	4.3 (0-4.9)
Power-law	Γ	1.5 (0.5-2.3)
+	Norm $(10^{-5})^a$	3.7 (0.6-44.6)
pshock	kT (keV)	0.23 (0.15-0.37)
	$n_{et}(10^{13}$ cm^3 s$^{-1})$	5 (Unconstrained)
	Norm $(10^{-3}$ cm$^{-5})$	4.2 (1.1-36.8)
	$\chi^2_\nu(\nu)$	0.966 (1036)

[a] Photons keV^{-1} cm^{-2} s^{-1}

[b] Observed flux in erg cm^{-2} s^{-1}

[c] Dust scattering halo component

(Hester et al., 2002; Pavlov et al., 2001). We searched for such features in G21.5−0.9 with the HRC observations from the same date, which were merged and normalized to 20 ks exposures. Figure 6.11 shows the result. The same process was followed for the ACIS observations, which are displayed in Figure 6.12. Unlike the Crab and Vela nebulae, G21.5−0.9 does not show persistent structure in the PWN. To reveal changes, difference images (see Figure 6.13) were created by subtracting one set of observations from the next.

If we assume that the features we see are persistent structures which have moved rather than new wisps which formed between observations we can calculate the velocity required. Tracking several bright knots we find velocities of 0.2–0.75 c with an average of 0.5 c. Performing the same analysis on the ACIS observations yields consistent results.

6.5 Discussion

6.5.1 Pulsar J1833-1034

The spectra of PSR J1833–1034 can be fitted reasonably well with a single power-law. The addition of a thermal blackbody component does improve the fit but only marginally. The F-test probability of 0.17 indicates that this component is unimportant compared to the previous result of Matheson & Safi-Harb (2010).We assume this thermal component is real and then examine the effect of the fit on the pulsar parameters. We assume black-body radiation, i.e., $L = 4\pi R^2 \sigma T^4$. The unabsorbed thermal flux of 4.57×10^{-13} erg cm^{-2} s^{-1} at a distance of 5 kpc and

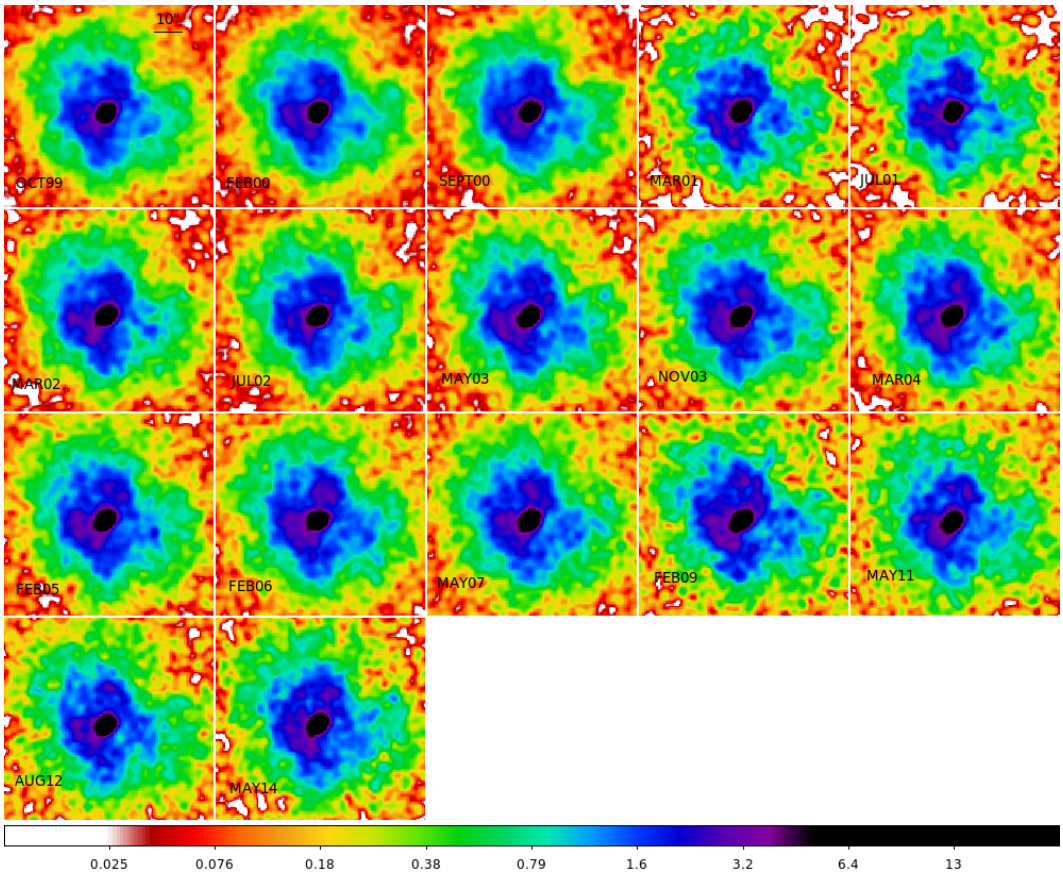

Figure 6.11: Variability seen with HRC.

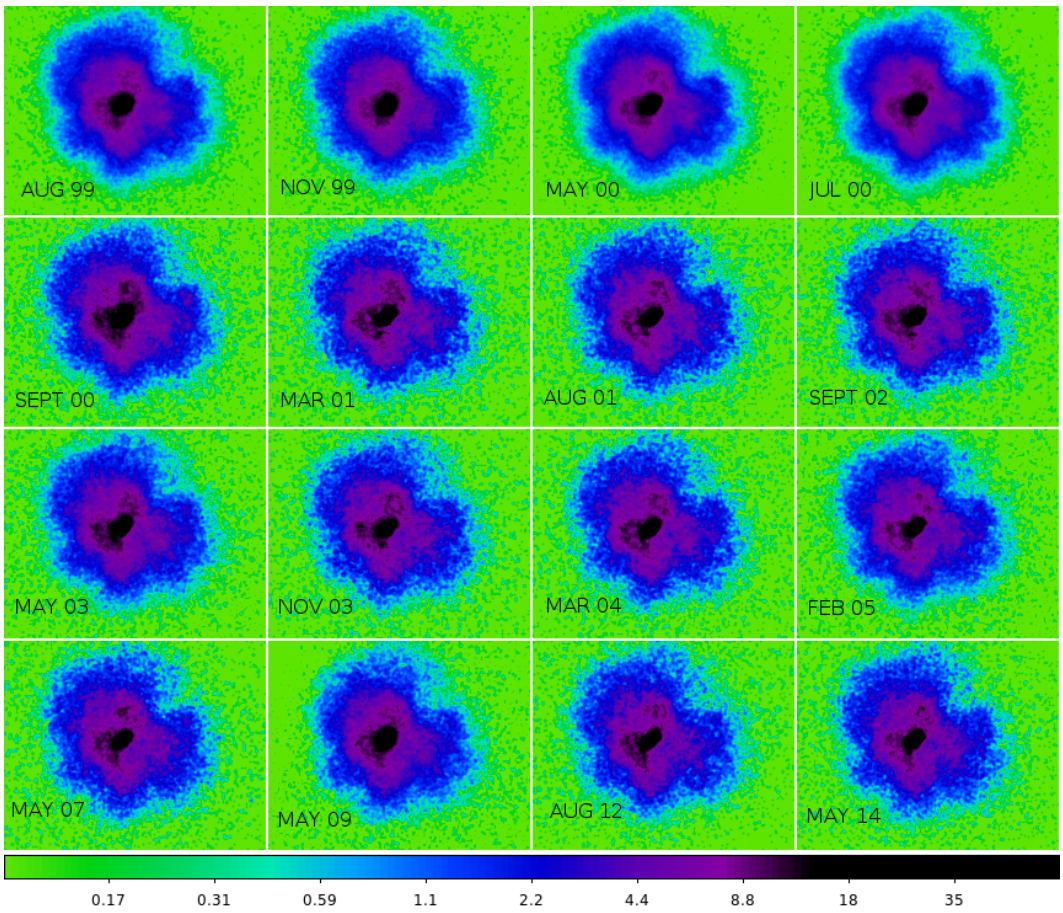

Figure 6.12: Variability seen with ACIS

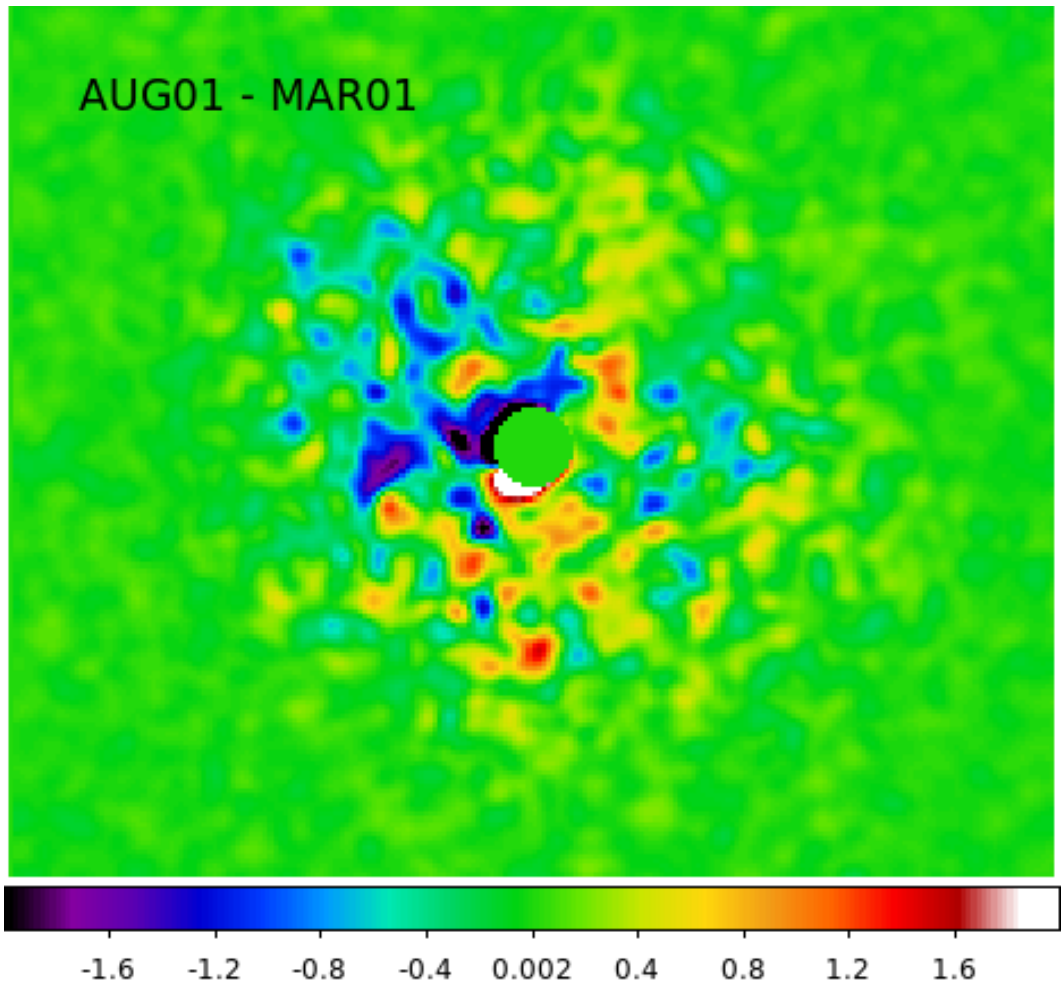

Figure 6.13: Sample ACIS difference image. The PSR has been removed to highlight the faint changes

temperature of 0.43 keV suggest an emitting region of 0.6 km in size, which is much smaller than the canonical radius of a neutron star and is consistent with the previous suggestion that the source is a small hot spot on the neutron star surface. The spectral map of the PWN (Figure 6.5) reveals that the PSR is offset from the regions of harder spectra. If we attribute this offset to the termination shock radius, then the nebular magnetic field can be estimated as follows. Given the spin-down energy loss $\dot{E} = 3.37 \times 10^{37}$ erg s^{-1} (Camilo et al., 2006), $\theta_s = 0.46'' \eta^{-1/2} d_5^{-1} B_{mG}^{-1}$, where $\theta_s = r_s/d$, η is the filling factor of pulsar wind and B_{mG} is the nebular magnetic field in mG. The offset of $3''.5$ suggests a magnetic field of 0.13 mG.

6.5.2 Pulsar wind nebula

Kennel & Coroniti (1984a,b) (hereafter KC) treat the pulsar wind as magnetohydrodynamic (MHD) flow and then derive the steady-state particle and magnetic field structure in the PWN with spherical symmetry and a purely advective wind flow. The KC model was able to explain the spectral and spatial distribution of the optical and X-ray emission in the Crab Nebula, but failed in the radio band. The discovery of axisymmetric jet-torus structures in PWNe like the Crab nebula with high resolution X-ray and optical imaging (e.g. Weisskopf et al., 2000; Hester, 2008) motivates 2-dimensional (2D) MHD simulations of PWNe with anisotropic pulsar wind power. Current 2D MHD simulations are able to reproduce the jet-torus structure and the inner ring feature in PWNe with polar angle dependent pulsar wind power (e.g. Komissarov & Lyubarsky, 2003; Del Zanna et al., 2006). However, toroidal structures are only detected in the inner part of the nebula (e.g. Safi-Harb

et al., 2001; Slane et al., 2004; Hester, 2008), where the impact of the pulsar wind is crucial. In the outer part of the nebula, complex filamentary structures with fingers and loops are instead observed (e.g. Seward et al., 2006; Hester, 2008). It is found that the standard MHD model ran into problems to explain the spectral index distribution and surface brightness profile in the outer part of the nebula (Amato et al., 2000; Slane et al., 2004). The polarization measurements (e.g. Hester, 2008) and the deep *Chandra* images (e.g. Seward et al., 2006) indicate that the magnetic topology in the filamentary structure is much more complicated than the toroidal field assumed in the standard MHD model.

Tang & Chevalier (2012) show that the introduction of diffusive particle transport in PWNe can explain the spectral index distribution and the nebular size behavior in young PWNe like the Crab and 3C 58 very well. It is assumed that advection plays a dominant role in the inner part of the nebula with toroidal structure, while diffusion becomes dominant in the outer part of the nebula with filamentary structure. The exact nature of diffusion is still unclear, and is likely induced by the Rayleigh-Taylor (RT) instability at the outer boundary of the nebula (e.g. Chevalier & Gull, 1975; Jun, 1998) or/and the kink instability triggered at the TS (e.g. Begelman, 1998; Camus et al., 2009). These fluid instabilities may be able to destroy the ordered toroidal field, which is imposed by the pulsar wind, and drive turbulence in the PWN. Recent 3-dimensional MHD and test particle simulations reveal a turbulent nebula with high velocity fluctuation (Porth et al., 2016), which indicates efficient diffusive transport of particles in PWNe. The effective diffusion coefficient is estimated as (Porth et al., 2016).

$$D_{eff} \sim 2 \times 10^{27} \left(\frac{L_{TS}}{0.13\mathrm{pc}}\right) \mathrm{cm}^2\mathrm{s}^{-1} \quad (6.1)$$

which is found to be independent of energy for electrons up to PeV energy. L_{TS} is the radius of TS.

In Fig. 6.14, we fit the spectral index distribution between 0.5 keV and 8 keV in G21.5-0.9 with both the KC model and a pure diffusion model (Tang & Chevalier, 2012) assuming simple spherical symmetry. The red dashed line represents the KC model results with $\sigma = 3 \times 10^{-3}$, $\alpha = 1.9$ and $B_{TS} = 50\mu G$,[4] where σ is the Poynting flux to particle energy flux ratio at the TS, α is the power law index of the injected particle spectrum and B_{TS} is the magnetic field at the TS. σ is chosen to be 3×10^{-3} to match the expansion velocity of 910 km/s at the outer boundary of G21.5–0.9 (Bietenholz & Bartel, 2008). It is clear that the KC model is inconsistent with the spectral index distribution in G21.5–0.9, which is similar to the previous study of 3C 58 (Slane et al., 2004). The blue solid line presents the diffusion model results with $\alpha = 1.9$, $D \sim 2.1 \times 10^{27}\mathrm{cm}^2/\mathrm{s}$ and $B = 130\mu G$ (see §5.1). D and B are the diffusion coefficient and magnetic field respectively, which are assumed to be constant for simplification and should be understood as the spatial averaged values in the PWN. The angular radius of the TS is assumed to be $\theta_s \sim 3''.5$. It is interesting to note that the effective diffusion coefficient D_{eff} defined in eq. (6.1) is estimated to

[4]In the KC model, the flow velocity decreases very quickly with radius in the postshock region. As a result, a small magnetic field is needed to explain the observed large nebular size. However, even with a small magnetic field, the KC model cannot reproduce the spectral index profile successfully as shown in Fig. 6.14, which motivates the introduction of diffusive transport of particles.

be $\sim 1.3 \times 10^{27}\mathrm{cm}^2/\mathrm{s}$ with $L_{TS} \sim 0.08\mathrm{pc}$, which agrees with our diffusion model results.

In the pure diffusion model, the photon index distribution of the nebula is determined by the dimensionless ratio $\zeta = r^2/Dt_c$, where r is the radius and t_c is the cooling time scale. If $\zeta \ll 1$, the photon index distribution is very flat. If $\zeta \gtrsim 1$, the photon index distribution gradually steepens as ζ increases. For synchrotron-dominated cooling, $\zeta \propto r^2 B^{3/2}\nu^{1/2}/D$, where ν is the corresponding emission frequency. The diffusion coefficient of charged particles in a nebula depends on the magnetic field configuration and the Larmor radius. The nature of this magnetic field dependence is not fully understood yet. In the limit of Bohm diffusion, $D \propto B^{-1}$ and $\zeta \propto r^2 B^{5/2}\nu^{1/2}$ which is considered to be a reasonable choice in the presence of strong turbulence (e.g., Hussein & Shalchi, 2014). Field line random walk represents another limiting case, in which magnetic field lines wander due to turbulence and the particles follow the field lines exclusively. In this case, the diffusion coefficient scales as $D \propto B^{-2}$ and $\zeta \propto r^2 B^{7/2}\nu^{1/2}$ (Shalchi, 2009). The magnetic dependence of D in the nebula is likely between the two limiting cases.

The spatial dependence of the magnetic field in the nebula is very complicated according to 2D and 3D MHD simulations (Del Zanna et al., 2006; Porth et al., 2016), which is beyond the scope of this work. Here we briefly discuss the magnetic configuration in the KC model. Behind the termination shock, the magnetic field evolves as $B \propto r$ due to the flux freezing. As r increases, the magnetic pressure gradually becomes dominant. After that, the radial speed is approximately constant and $B \propto r^{-1}$ instead. In the $B \propto r$ regime, which corresponds to the inner part

of the nebula, we have $\zeta \propto r^{9/2}$ for Bohm diffusion and $\zeta \propto r^{11/2}$ for field line random walk respectively. If ζ increases with radius, we expect the photon index distribution steepens much faster with radius compared to our simplified calculation with constant D and B. In the $B \propto r^{-1}$ regime, which corresponds to the outer part of the nebula, we instead have $\zeta \propto r^{-1/2}$ and $\zeta \propto r^{-3/2}$ for the two limiting cases of diffusion. If ζ decreases with radius, the photon index distribution becomes more flat compared to our simplified calculation. In summary, if we consider the spatial dependence of B and D described above, then the photon index distribution steepens in the inner region and flattens in the outer region, which appears to be more consistent with the data of G21.5–0.9.

Based on the above discussion, when $D \propto B^{3/2}$, ζ is the same and the photon index distribution remains almost the same. If we instead assume $B = 50\mu G$ as indicated by de Jager et al. (2008), then we obtain $D \sim 5 \times 10^{26}\mathrm{cm}^2/\mathrm{s}$, which is consistent with the results derived in Porth et al. (2016) based on 3D MHD simulations. Recently, G21.5–0.9 was discussed by Lu et al. (2017) with an improved model including dynamical evolution of the central pulsar, energy dependence of diffusion coefficient D, and radial dependence of diffusion coefficient D and magnetic field B. It is not straightforward to compare with their fitting results directly. Here we only consider the spatially averaged value derived at present day. Lu et al. (2017) found that $B \sim 40\mu G$ and $D \sim 1 \times 10^{26} cm^2 s^{-1}$ for the energy range of interest here, which is consistent with our simple toy model results surprisingly well (we note that the diffusion coefficient shown in Table 2 of Lu et al. (2017) is at a much lower electron energy). According to the above discussion, if we assume the diffusion

coefficient provided in eq (6.1) is a good approximation, then we can decouple D and B in the pure diffusion model and apply the model to estimate the spatially averaged magnetic field in a PWN.

6.5.3 Supernova Remnant

The absence of a shell-like structure surrounding some PWNe is a long standing puzzle. Whether the undetected shells are due to expansion into a very low density medium or a consequence of a low energy electron-capture supernova explosion (e.g., Nomoto et al. (1982); Yang & Chevalier (2015)) remains an open question. Deep observations revealed thermal emission in 3C 58 (Bocchino et al., 2001; Gotthelf et al., 2007) and G54.1+0.3 (Bocchino et al., 2010), which is attributed to the missing shells and/or shock-heated supernova ejecta. The faint thermal emission detected in the eastern limb may be used to calculate the shock speed and estimate the energy released during the supernova event. The Rankine-Hugoniot relations for an adiabatic shock (Reynolds, 2008) yield $kT = \frac{3}{16}\mu m_p v_s^2$, where μ is the mean mass per particle ($\mu \approx 0.6$), m_p is the proton mass and v_s is the shock speed. The observed temperature of 0.37 keV corresponds to a shock speed of 562 km/s. Assuming a constant shock velocity and 5 kpc distance, the $140''$ shell radius gives an age of 1.2 kyr, which is slightly larger than the 870 years derived from radio observations of the nebula expansion with a velocity of 910 km/s. For young remnants with an age less than 1000 years, the forward shock speed is expected to be higher. Although the derived temperature is low, it is consistent with that found in 3C 58 (Gotthelf et al., 2007; Bocchino et al., 2001), which is described by a dominant

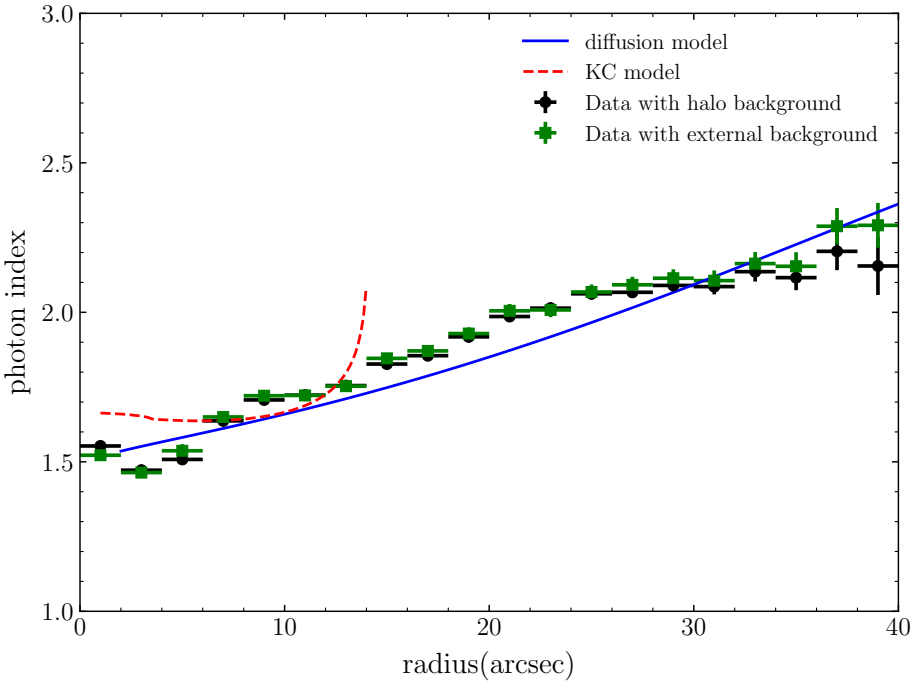

Figure 6.14: Fitting of the photon index distribution between 0.5 keV and 8 keV in G21.5–0.9. The black and green crossings are the data with halo and external background respectively. The blue solid line is the pure diffusion model fitting with $\alpha = 1.9$, $B = 130\mu G$ and $D \sim 2.1 \times 10^{27}\mathrm{cm}^2/\mathrm{s}$. The red dashed line is the KC model fitting with $\alpha = 1.9$, $B_{TS} = 50\mu G$ and $\sigma = 3 \times 10^{-3}$.

non-thermal component with $\Gamma \sim 2-3$ and a weaker thermal component with $kT \sim 0.2$ keV. However, 3C58 is older, and more evolved, with the thermal emission residing at the outer boundary of the PWN rather than a distinct and separate limb-brightened component. The low temperature may indicate a non-equilibrium state of the electrons and ions as suggested by Hughes et al. (2000), therefore we note that the estimated shock velocity scales as $\sqrt{T_p/T_e}$. We use the thermal component to calculate the ambient density into which the shock wave is expanding. For a limb emitting volume of $6 \times 10^{56} D_5^3 f cm^3$, where f is the filling factor, we find a number density of 1.76 cm^{-3} which corresponds to a limb mass of $\sim 1 M_\odot$. If we assume this is the swept-up mass, then the remnant must be expanding into a low-density medium with $n_e \sim 0.19$ cm^{-3}, which is smaller than the upper limit of 0.65 cm^{-3} provided by Bocchino et al. (2005). Extending the limb to a full sphere, we estimate the kinetic energy of the supernova to be 3×10^{49} erg, which is much smaller than the 10^{51} erg expected for a typical supernova. The minimal thermal emission may indicate the SNR is expanding into the wind blown bubble produced by its progenitor. Elwood et al. (2017) predicts cavities with radii of $\approx$ 2–20 pc. G21.5−0.9 is consistent with the lower limit of this range. The low mass loss prior to a type IIP supernova combined with the wind blown cavity suggests the shock has not yet swept up enough mass to transition into a Sedov-Taylor phase.

Future observations with a sensitive, high-resolution, spectrometer such as the X-Ray Imaging and Spectroscopy Mission ($XRISM$, formerly known as $XARM$) in the near future, and $ATHENA$ in the more distant future, should reveal the missing thermal X-ray emission from the shocked ambient or circumstellar material

in G21.5–0.9 and other shell-less PWNe.

Acknowledgements

We thank Roger Chevalier for comments on the manuscript. This research made use of NASA's Astrophysics Data System and the HEASARC operated by NASA's Goddard Space Flight Center. S.S.H. acknowledges support by NSERC through the Discovery Grants and the Canada Research Chairs programs, and by the Canadian Space Agency. B.G. acknowledges support from a University of Manitoba Graduate Fellowship. We thank the referee for their careful reading of the paper which helped improve its quality and clarity.

Chapter 7

CTB 87

Next we examine CTB 87 – a plerionic remnant which does not show a shell at any wavelength. Unlike the young circular remnant G21.5–0.9 discussed in the previous chapter, CTB 87 is an evolved pulsar wind nebula. It displays a cometary morphology in X-ray, while the offset radio emission resembles a boomerang with the elbow pointing towards the X-ray peak. Previous analysis of a *Chandra* observation (Matheson et al. (2013)) resolved the putative pulsar CXOU J201609.2+37111, surrounded by a an extended X-ray nebula. The morphology was interpreted as either a bow-shock or reverse shock interaction, with the latter appearing more likely. The lack of a visible shell at any wavelength complicates the analysis. Here we present a deep observation of CTB 87 utilising the superior sensitivity and larger field of view of *XMM-Newton*. We examine the morphological and evolutionary stage of the pulsar wind nebula, search for thermal emission expected from a supernova shell or reverse shock interaction, present the first spectral index map and compare with numerical MHD simulations of this system. This chapter contains text and images from Guest, B., Safi-Harb, S., MacMaster, A., Kothes, R., Olmi, B., Amato, E.,

Bucciantini, N., & Arzoumanian, Z., *Deciphering the Morphology of the Pulsar Wind Nebula CTB 87 with XMM-Newton.* Monthly Notices of the Royal Astronomical Society, 491, 2, 2020.

7.1 Introduction

CTB 87 is a plerionic supernova remnant (SNR) which shows a centrally filled morphology with no evidence of a shell at any wavelength. It has a radio size of $8' \times 6'$ with a central flux density of 9 Jy at 1 GHz (Green 2014) and a spectral break at 11 GHz (Sun et al. 2011). HI data from the Canadian Galactic Plane Survey (Kothes et al. 2003) provides a distance estimate of 6.1 kpc. Recently Liu et al. (2018) found a superbubble, $\sim 37'$ in radius surrounding the SNR using HI 21 cm, WISE mid-IR, and optical extinction data. A previous *Chandra* observation (Matheson et al. 2013) identified a point source, CXOU J201609.2+371110, as the putative pulsar, and found an offset of $\sim 100''$ between the X-ray and radio peaks. Paired with the cometary morphology of the X-ray emission, this suggested the radio is either an evolved PWN due to supersonic motion of the neutron star, or a relic nebula resulting from interaction with the reverse shock. Observations in γ-rays with MILAGRO revealed an unresolved source, MGRO J2019+37 (Abdo et al. 2007). This was later resolved by VERITAS as two sources, of which VER J2016+371 is spatially coincident with CTB 87 (Aliu et al. 2014). *Fermi*-LAT found a source nearby to this VERITAS source in each of the 3 FGL catalogs (Abdo et al. 2010; Nolan et al. 2012; Acero et al. 2015), the high energy FHL catalogs (Ackermann et al. 2013, 2016; Ajello et al. (2017)), and the supernova remnant catalog (Acero et al. 2016). The

relation of this source to CTB 87 is unclear. The *Fermi* source position is slightly different depending on the energy band used. Abeysekara et al. (2018) argues this is the result of two unresolved high energy γ-ray sources, an idea supported by the evidence of variability in the low-energy FGL catalog analysis with reduced evidence in the FHL analysis. When the *Fermi* emission is modeled as two point sources, a single power-law is required to fit the CTB 87 point source and the TeV VERITAS emission.

This study is aimed at addressing the nature of the PWN through a deep *XMM-Newton* observation combined with numerical simulations. In particular, we aim to address the cometary morphology of the PWN, constrain its spectral properties and search for (the so far missing) thermal X-ray emission expected from a supernova shell or reverse shock interaction with supernova ejecta. This is particularly important for addressing the nature of the growing class of shell-less PWNe which currently constitute 8–15% of the SNR population (Ferrand & Safi-Harb, 2012)[1]. Section 2 describes the observations. In Sections 3 and 4, we present our imaging and spectroscopy study results, including the first spectral index map of the PWN and the search for thermal X-ray emission from the SNR. In Section 5, we discuss these results in light of the evolutionary scenario for CTB 87 and the properties of its putative pulsar. Section 6 presents our numerical simulations aimed at reproducing the morphology of the compact X-ray nebula and spectral index map. Finally, we summarize our results and conclusions in Section 7.

[1]http://snrcat.physics.umanitoba.ca

7.2 Observations

CTB 87 (G74.9+1.2) was observed with *XMM-Newton* (ObsID 0744640101) for 125 ks starting 14 December 2014. The European Photon Imaging Camera (EPIC) detectors; MOS1, MOS2, and pn were operated in full frame imaging modes with the medium filter. Data were processed with the Science Analysis System (SAS) Version 16.1.0. Filtering for good time intervals, bad pixels, and out of time events was performed with *emchain/epchain* for MOS and pn, respectively. Data products were then more strictly filtered for flaring with *evselect* and *tabgtigen* based on the appearance of the light curves. The effective exposure following filtering was 100 ks for MOS1, 105 ks for MOS2, and 75.4 ks for pn. Spectra were extracted separately from each detector with *evselect* and fit simultaneously using the X-ray spectral fitting software XSPEC v12.9.1 (Arnaud 1996) over the $0.3 - 10$ keV energy range.

7.3 Imaging

Matheson et al. (2013) used the superb angular resolution of the *Chandra* X-ray Observatory to identify a point source as the putative pulsar, and arcs at the edge of the X-ray nebula which extend towards the radio peak. We recognize the pulsar as the bright source towards the centre of the PWN (Figure 7.1), and observe a cometary morphology with the PWN appearing brighter to the north-west of the pulsar. The arcs seen with *Chandra*, however, are not readily apparent. An abundance of faint nebular emission not seen before appear in the *XMM-Newton* data extending to the south-east, with the south-west edge lying along a chip gap in the pn detector.

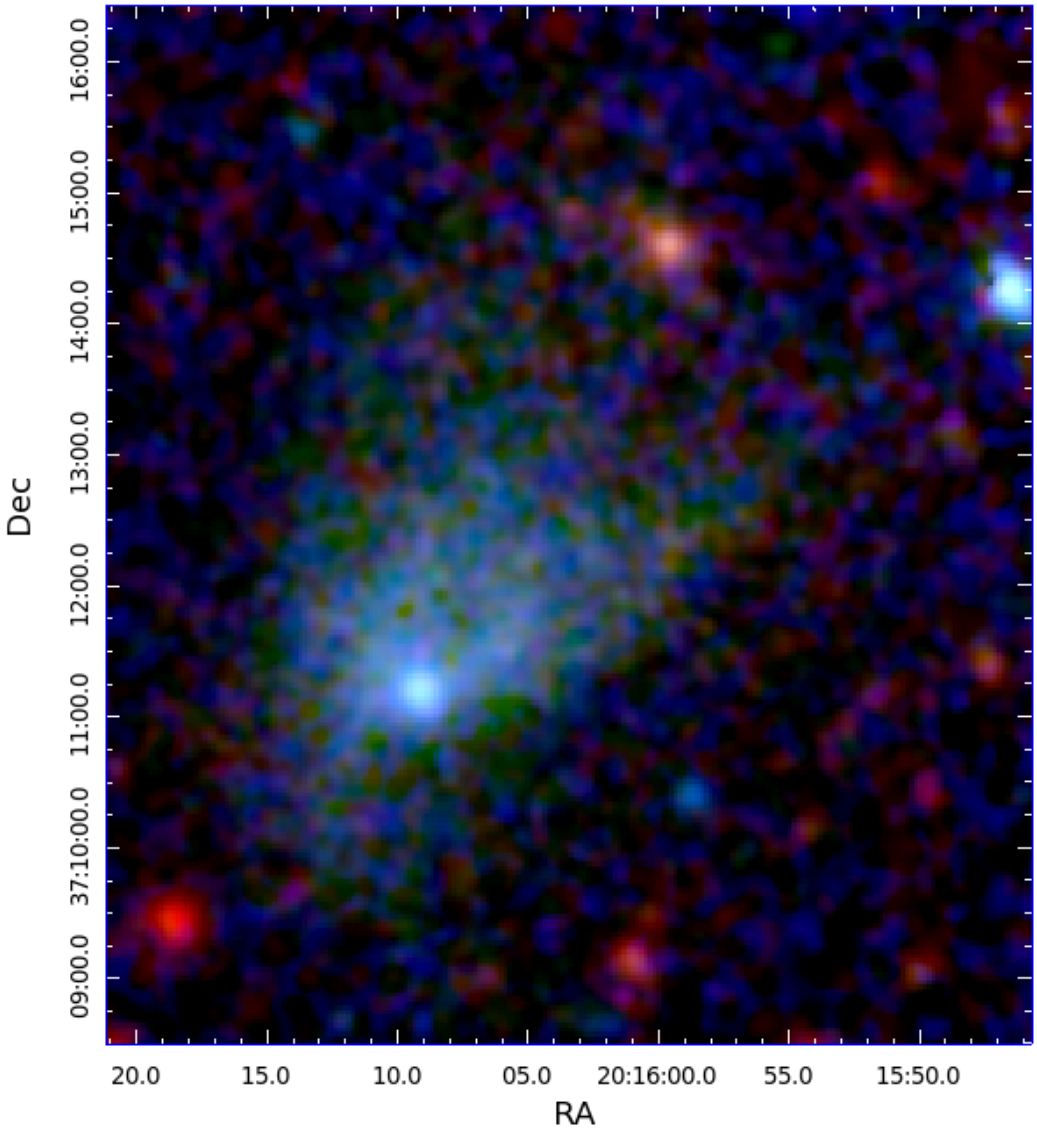

Figure 7.1: Merged MOS1, MOS2 and pn RGB image adaptively smoothed to a signal-to-noise ratio of 4. The energy bands are Red: 0.3-1.5 keV, Green: 1.5-5 keV, Blue: 5-10 keV.

7.4 Spectroscopic Analysis

Here we present a spatially resolved spectroscopic analysis of the different components of CTB 87. Our spectroscopic study is targeted to constrain the parameters of the pulsar candidate and associated nebula (§4.1 and §4.2), map the spectral index across the SNR (§4.3 and §4.4), as well as search for any thermal X-ray emission that could be associated with the SNR (§4.5). *XMM-Newton* has the advantage (over *Chandra*) of its sensitivity to low-surface brightness emission.

7.4.1 Compact Object

Spectra from the putative pulsar were extracted from a circle centred at $\alpha(2000) = 20^h19^m9^s.2$, $\delta = +37^o11'10"$. Background spectra were extracted from a surrounding annulus. Due to the differing PSF of the detectors, the extraction radii are $8''$ for MOS1 and MOS2 and $11''$ for pn, with backgrounds spanning $10''$–$13''$ and $12''$–$15''$, respectively. The spectra were fit with an absorbed power-law with the absorption given by the Tuebingen-Boulder ISM absorption model (tbabs) with the abundances from Wilms et al. (2000b). The column density was frozen to 2.249×10^{22} cm^{-2}, the best fit value found from fitting the diffuse nebula emission (see section 7.4.2). The best fit yields a photon index $\Gamma = 1.62\,(1.48 - 1.77)$ and an absorbed flux of $F_{abs,0.3-10\ keV} = 7.56 \times 10^{-13}$ erg cm^{-2} s^{-1} where the parameters are reported with 90% confidence intervals. The spectrum is shown in Figure 7.2.

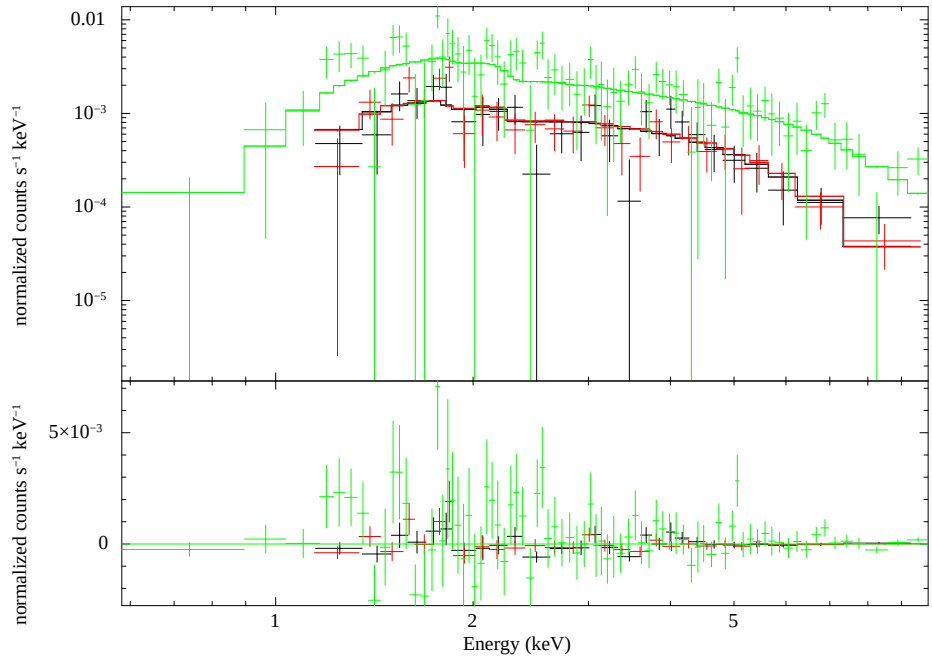

Figure 7.2: Pulsar spectrum and residuals from the MOS (black,red) and PN (green) detectors plotted with the best fit model.

7.4.2 Diffuse Nebula

To examine the properties of the extended nebular emission we extract spectra from the outer green ellipse ($171'' \times 129''$) in Figure 7.3 with a $10''$-radius circle containing the pulsar and the unrelated point source to the north excluded. Background was extracted from a surrounding elliptical annulus ($200'' \times 160''$ shown in red in Fig. 7.3). The best fit result was found with an absorbed power-law model with a column density 2.25 (2.10 – 2.40) $\times$ 10^{22} cm^{-2}, photon index $\Gamma = 1.91$ (1.84 – 1.99). This column density was then frozen for the subsequent fits to the inner regions (Table 7.1).

7.4.3 Radial Profile

One of the main questions surrounding CTB 87 is the nature of its morphology. The previous *Chandra* study by Matheson et al. (2013) identified a bow-shock or cometary appearance of the X-ray PWN and favoured a reverse shock interaction model rather than one of ram-pressure confinement due to an inferred high pulsar velocity. We examine spectra from opposite directions of the pulsar candidate to search for evidence of an interaction. The radial profile regions (Figure 7.4) are selected by generating 5 concentric rings centred on the pulsar from $5'' - 217''$, with the angular extent given by the polygon which bounds the cometary morphology to the north west, and a symmetric polygon to the south east. As the reverse shock encounters the PWN, it is predicted to compress the local magnetic field, leading to a more rapid synchrotron burn off, and softening of the spectral index (e.g., Kennel & Coroniti (1984b)). Comparing the profiles (Figure 7.5), we find that the spectral

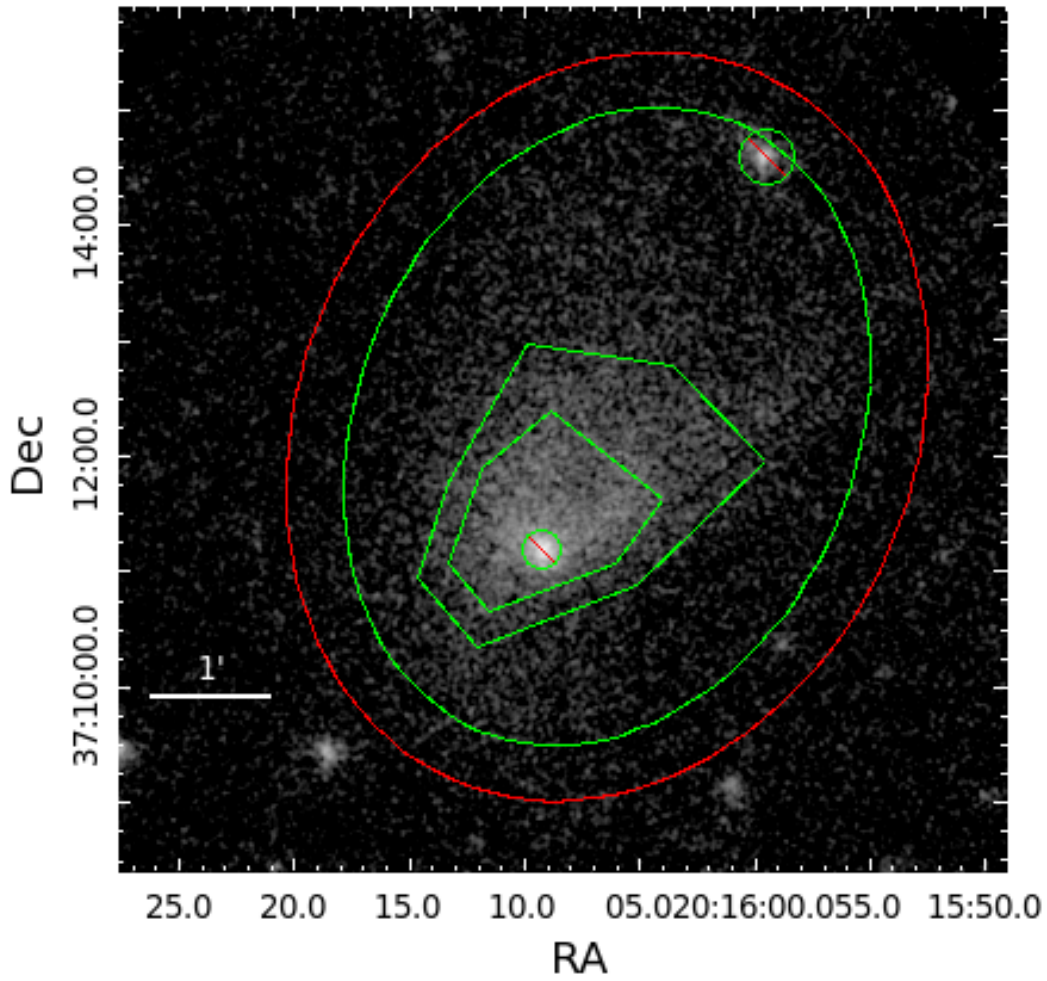

Figure 7.3: Regions used to examine the diffuse nebular emission. The green ellipse defines the total diffuse region, while the red bounds the annulus used for background subtraction.

	Total	Outer	Mid	Inner	Pulsar
N_H 10^{22} [a]	2.25 (2.10 - 2.40)	2.25	2.25	2.25	2.25
Photon index, Γ	1.91 (1.84 - 1.99)	2.18 (2.09 - 2.27)	1.93 (1.88 - 1.98)	1.76 (1.73 - 1.80)	1.62 (1.48 - 1.77)
Norm 10^{-4} [b]	5.61 (5.05 - 6.26)	2.62 (2.38 - 2.87)	1.45 (1.37 - 1.53)	1.65 (1.58 - 1.72)	0.17 (0.15 - 0.20)
$\chi^2(\nu)$	1.080 (1039)	1.112 (675)	1.055 (612)	0.931 (664)	0.998 (133)
Flux 10^{-13} [c]	16.01 (15.71 - 16.23)	5.07 (4.91 - 5.24)	4.01 (3.92 - 4.10)	5.85 (5.77 - 5.94)	0.76 (0.72 - 0.78)

Confidence ranges are 90%. Models were fit over the range 0.3–10 keV

[a] cm^{-2}

[b] photons keV^{-1} cm^{-2} s^{-1}

[c] erg cm^{-2} s^{-1}, 0.3-10 keV observed.

Table 7.1: Absorbed power-law model fits to the regions shown in Fig. 7.3.

indices are consistent within error, suggesting that if a reverse shock interaction has occurred, enough time has elapsed for the pulsar wind to return the nebula to equilibrium. We note that there is an apparent trend of softer indices for the southern (blue) region shown in Figure 7.4 out to a 150″-radius, however the errorbars are larger for this region given the lower surface brightness. A deeper observation is needed to study the southern outflow, particularly visible in Figure 7.3, to constrain its spectral index and its variation.

7.4.4 Photon Index Map

The apparent pure non-thermal nature of CTB 87 makes traditional RGB images appear simplistic with the only observable being a slight softening of the bulk emission with distance from the pulsar. To search for fine detail and hidden features in the non-thermal emission, we generate a photon index map. Using the adaptive binning software *Contbin* (Sanders 2006) we generate regions which meet a signal limit (chosen such that each contains at least 400 counts by the MOS detectors), extract spectra and fit with an absorbed power-law. The absorption was frozen to the best fit value from the total nebula region. The spectral map (Figure 7.6) shows steepening with distance from the central pulsar, along with trailing arms stretching to the north-west towards the radio peak.

7.4.5 Search for Thermal Emission

Our RGB image (Figure 7.1) shows no clear signs of excess soft X-ray emission attributable to shocked ISM or ejecta. We therefore take two approaches for our search

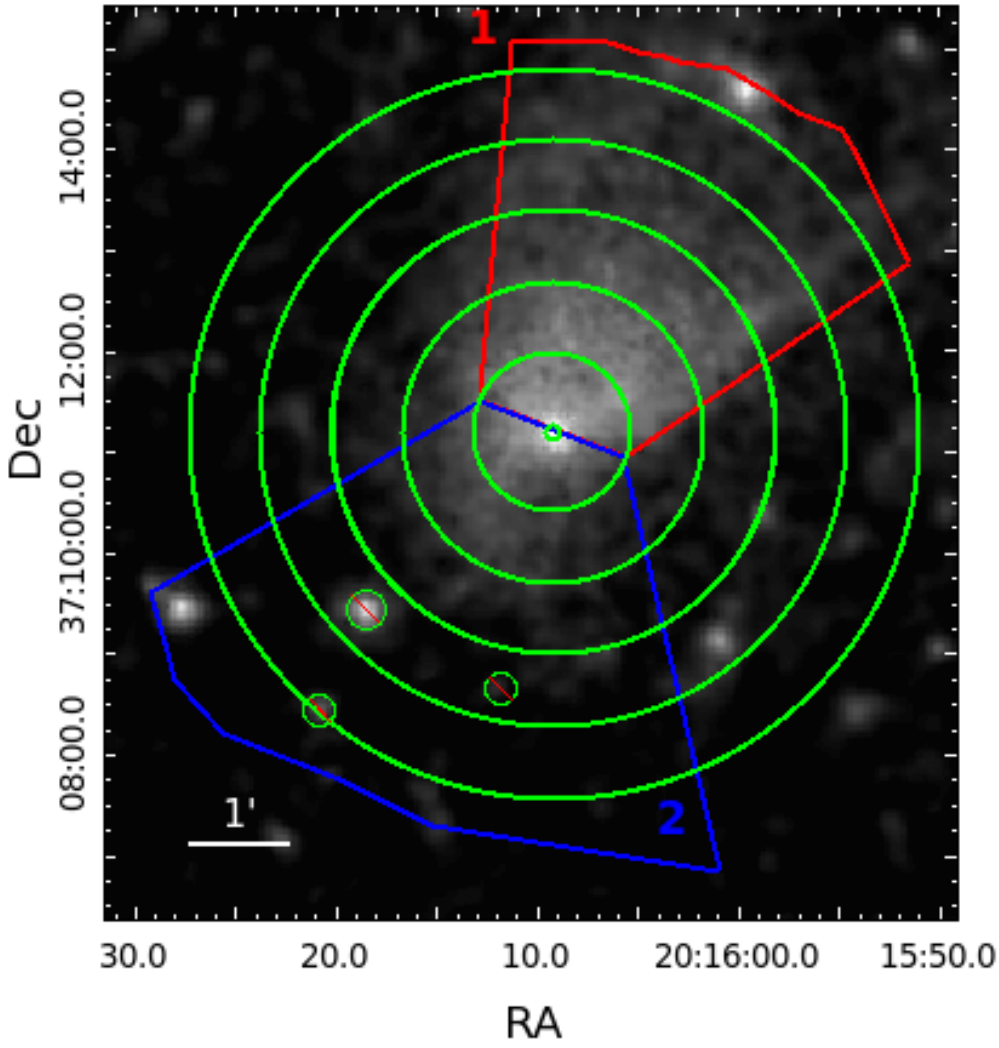

Figure 7.4: Regions used to extract spectra for the radial profile. Point sources (shown in circles) were removed before fitting the PWN's spectra.

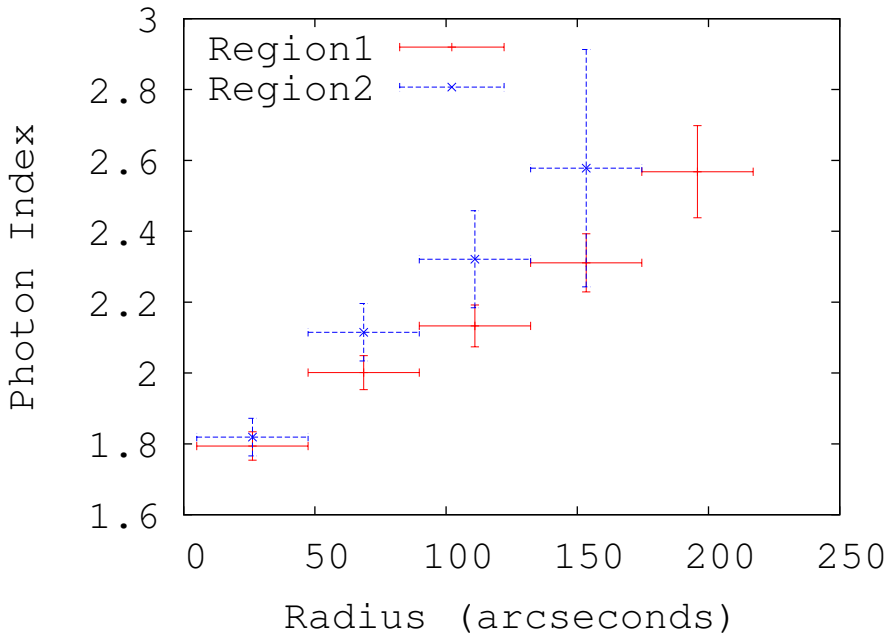

Figure 7.5: Results of radial profile analysis showing the photon index at increasing distance from the pulsar for the regions shown in Figure 7.4. Region 1 follows the cometary morphology back towards the radio peak. Region 2 covers the emission ahead of the proposed bow shock. We do not display the outermost section of region 2 as it does not contain sufficient emission to fit a spectrum.

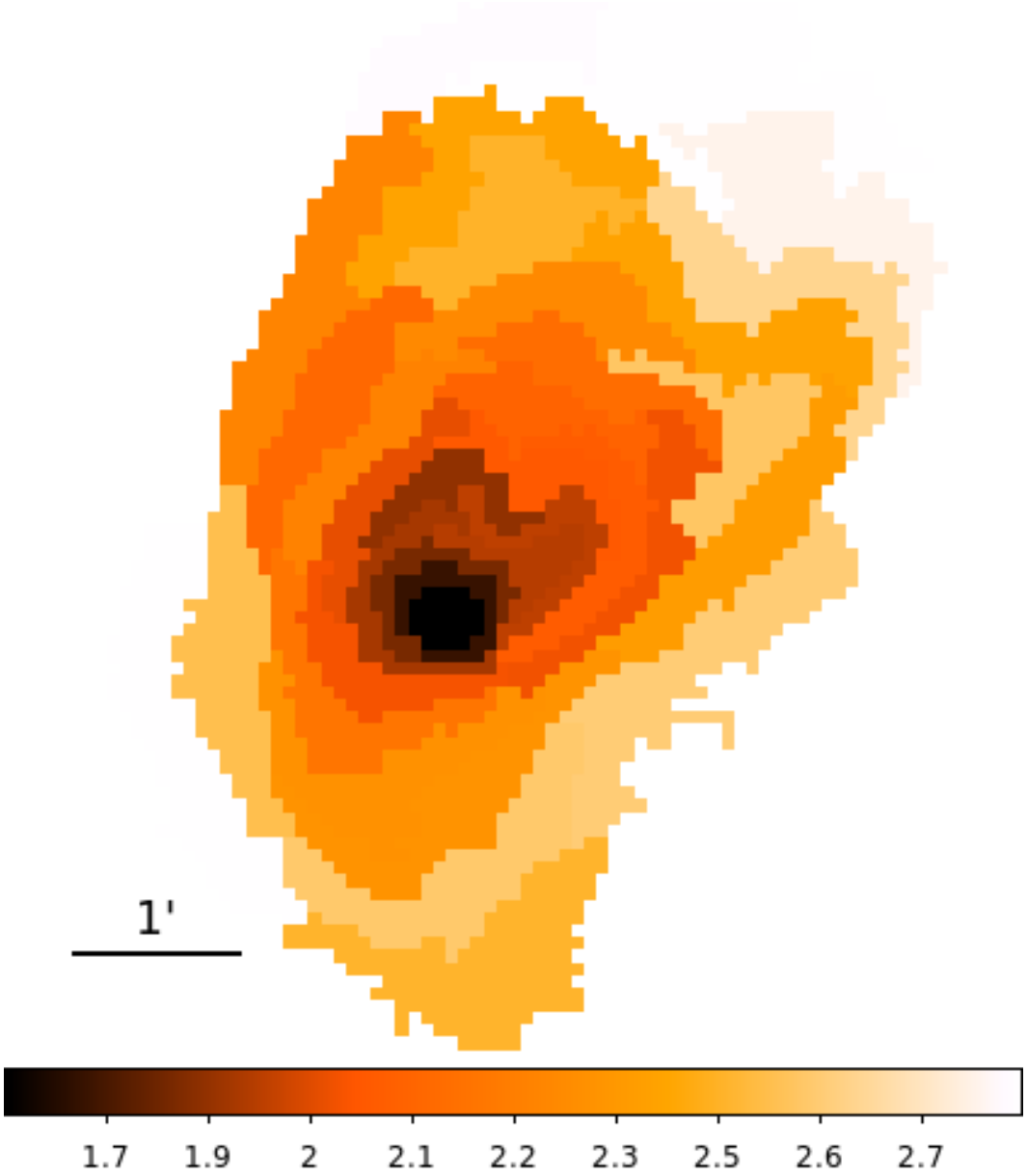

Figure 7.6: Adaptively binned regions covering the PWN, each fit with an absorbed power-law and coloured by photon-index. The cometary morphology is apparent with trailing arms. There is also extended emission to the south.

for thermal X-ray emission from CTB 87. First, we extract spectra from an elliptical annulus region surrounding the X-ray PWN and fit it with an absorbed thermal model (*APEC* in XSPEC) which refers to the 'Astrophysical Plasma Emission Code' (Smith et al. 2001) and describes collisionally ionized diffuse gas calculated from the AtomDB atomic database. This gives an upper limit on the observed thermal flux from a surrounding shock-heated medium of 1.85×10^{-13} erg cm^{-2} s^{-1}. If the cometary morphology is due to the interaction with a reverse shock, we expect the dominant source of thermal emission to be along the bow-shock like feature. Our second approach to place limits on the thermal emission is to freeze the best fit power-law parameters from the total diffuse region and add a thermal APEC component until the model exceeds the data by 2σ. This provides an observed flux limit of 8.687×10^{-15} erg cm^{-2} s^{-1} for a temperature of kT = 0.82 keV, the best fit temperature from the surrounding region. We later investigate the density implied by a range of temperatures (Section 7.5.2).

7.5 Discussion

7.5.1 Putative Pulsar Properties

To date no pulsations have been observed from CTB 87, however we may estimate the properties of the neutron star using its X-ray flux and the empirical results of Li et al. (2008). The unabsorbed putative pulsar's luminosity in the 2–10 keV band is $3.5 \times 10^{32} D_{6.1}^2$ erg s^{-1}. The spin-down energy loss ($\dot{E}$) is then given by $L_{\rm X,PSR} = 10^{-0.8} \dot{E}^{0.92}$ leading to $\dot{E} = 1.76 \times 10^{36}$ erg s^{-1}. Alternatively an estimate can be

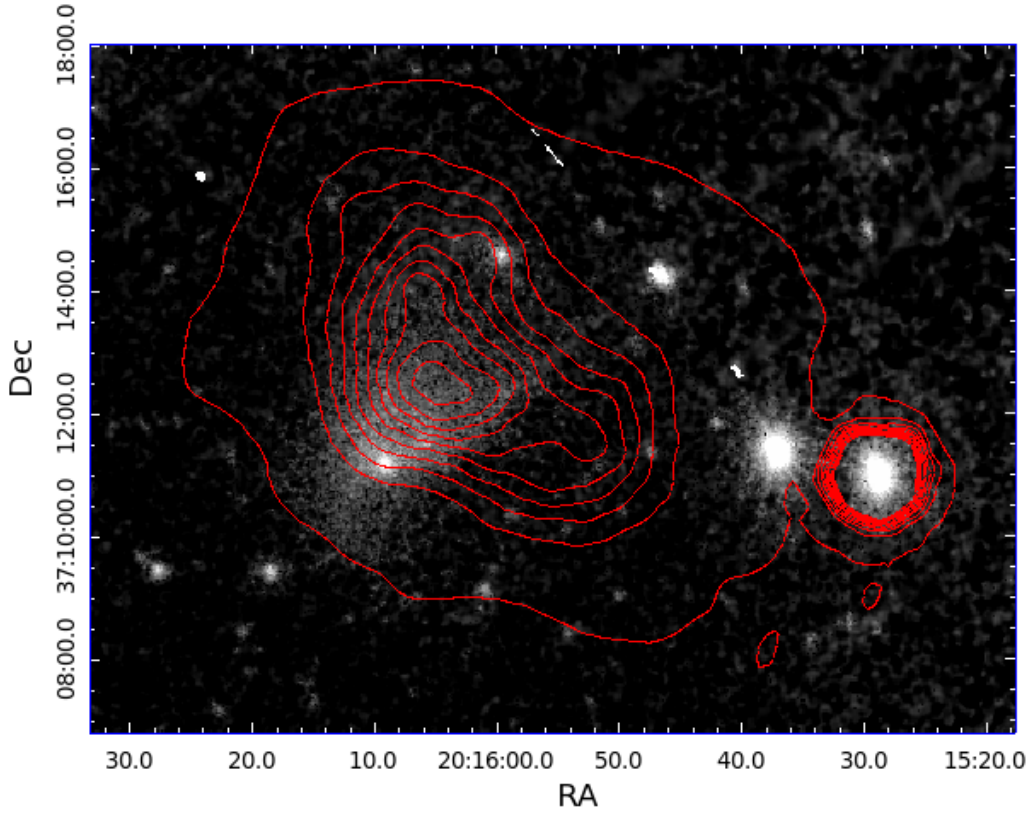

Figure 7.7: Merged MOS1, MOS2, and pn image overlayed with the radio contours from the Dominion Radio Astrophysical Observatory as part of the Canadian Galactic Plane Survey (Taylor et al. (2003)).

made from the unabsorbed PWN luminosity in the same band ($L = 7.4 \times 10^{33} D_{6.1}^2$ erg s^{-1}) and the spin-down energy loss may be predicted from $L_{\rm X,PWN} = 10^{-19.6} \dot{E}^{1.45}$ which gives $\dot{E} = 7.5 \times 10^{36}$ erg s^{-1}.

Li et al. (2008) also provide empirical results for the characteristic age (τ) of a pulsar given either the pulsar or PWN luminosity. These are, respectively, $L_{\rm x,PSR} = 10^{38.9} \tau^{-1.4}$ yr, and $L_{\rm x,PWN} = 10^{42.4} \tau^{-2.1}$ yr, leading to ages of ∼34.5 kyr and 11.5 kyr respectively. This is comparable to the 5–28 kyr estimate from Matheson et al. (2013) which was based on typical neutron star kick velocities and the assumption of the radio emission belonging to a relic nebula formed at the birth location of the pulsar.

Combining this age with the predicted spin-down energy loss allows an estimate of the pulsar properties through the spin-down energy loss and pulsar braking index relations (described in, e.g., Gaensler & Slane (2006)). The period (P) is given by $P = ((4\pi^2 I)/((n-1)\dot{E}\tau))^{1/2}$, the period derivative by $\dot{P} = P/((n-1)\tau)$, and surface magnetic field by $\mathrm{B} = 3.2 \times 10^{19} I_{45}^{1/2} R_{10}^{-3} (P\dot{P})^{1/2}$. Here n is the braking index, I_{45} is the moment of inertia of the neutron star in units of 10^{45}g cm^2, and R_{10} is the radius in units of 10 km. Table 7.2 lists estimates of these values based on the two different calculated energy loss rates and an adopted average age of 20 kyr. These properties are within the range expected for rotation-powered pulsars with prominent PWNe. Future timing observations of CXOU J201609.2+371110 are needed to pin down the properties of this pulsar candidate.

$\dot{E}$	1.76×10^{36} erg s^{-1}	7.5×10^{36} erg s^{-1}
P [a]	0.13 s	0.065 s
$\dot{P}$ [b]	1.06×10^{-13}	0.51×10^{-13}
B [c]	1.8×10^{12} G	3.8×10^{12} G

[a] $I_{45}^{1/2}\dot{E}_{36}^{-1/2}t_{20}^{-1/2}$ [b] $I_{45}^{1/2}\dot{E}_{36}^{-1/2}t_{20}^{-3/2}$ [c] $I_{45}\dot{E}_{36}^{-1/2}R_{10}^{-3}t_{20}^{-1}$

Table 7.2: Pulsar properties based on the spin-down energy loss derived from the X-ray luminosity of the pulsar (left) and PWN (right), and a characteristic age of 20 kyr.

7.5.2 Limits on Ambient Density and Faint Thermal Emission

No thermal X-ray emission nor limb-brightening has been detected from CTB 87. The lack of any observed SNR shell suggests expansion into a low-density medium. To examine the level of density down to which our observations are sensitive we set an upper limit on the density of emitting electrons by estimating the upper limit on any thermal contribution to the total diffuse emission. The normalization of an additional thermal component in the diffuse region has an upper limit of $\frac{10^{-14}}{4\pi D^2}\int n_e n_H dV = 5.67 \times 10^{-5}\mathrm{cm}^{-5}$ (for kT=0.82 keV). This implies that $\int n_e n_H dV \sim f n_e n_H V = 10^{14}(4\pi D^2)(5.67 \times 10^{-5} cm^{-5})$, where f is the volume filling factor, n_e is the electron density, $n_H \sim n_e/1.2$. The total volume V is assumed to be an ellipsoid with semi-axis of a=b=171″, and c=129″. This volume projected is the ellipse shown in Figure 7.3. The electron density upper limit is then $n_e < 0.05 f^{-1/2} D_{6.1}^{-1/2}$ cm^{-3}. To understand how our assumption of the temperature of the emitting electrons affects the density we freeze the temperature parameter and derive the corresponding upper limit for the electron density. The results are shown in Figure 7.8. The high

temperature and low inferred density are consistent with the picture of expansion into a stellar wind blown bubble (Matheson et al. 2013; Liu et al. 2018, Kothes et al. in prep.)

According to the radio study (Kothes et al., in prep), the shell-type SNR has a radius which would place it outside the *Chandra* and *XMM-Newton* observations in any direction. In addition, any thermal emission from those parts of the shell that is moving towards us or away from us would be too faint and diffuse to be detected. Because of the large size, its thermal emission would have been subtracted with the estimated background.

The other thermal component that could be detected is the emission from the supernova ejecta. The radio study (Kothes et al., in prep) places the blast wave of the supernova explosion at a radius larger than 30 pc inside the HI cavity. For a maximum ejecta mass of 20 $M_\odot$, evenly distributed inside the SNR, we would find an average electron density of about $n_e = 0.006$ cm^{-3} assuming it consists of 90 % hydrogen and 10 % helium and the material is fully ionized. This is obviously a lower limit since the ejecta should also contain heavier elements, in which case we would get a lower number of electrons per mass unit. This is well below our detection threshold for any reasonable temperature.

In the direction of the molecular cloud complex a candidate for a radio shell was detected with a radius of about 13 pc (Kothes et al., in prep). If we distribute ejecta of 20 $M_\odot$ evenly inside this shell, we get an average electron density of $n_e = 0.075$ cm^{-3}, again, fully ionized, with 90% hydrogen and 10% helium. This is slightly above our detection threshold, but this is of course an upper limit since we do not take heavier

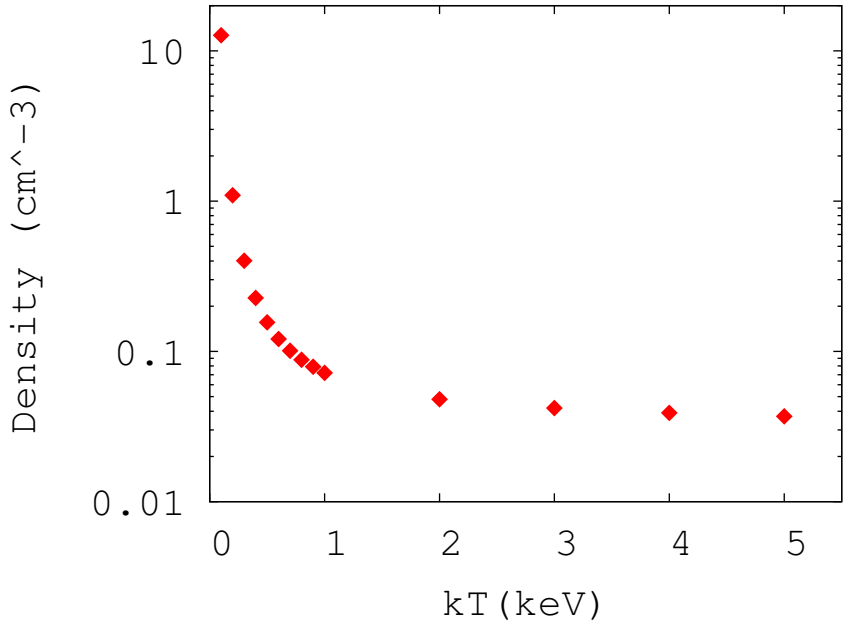

Figure 7.8: Upper limit on the ambient density derived from adding a thermal bremsstrahlung component with fixed temperature.

elements into account. Below 15 $M_{\odot}$ the thermal emission from the ejecta would definitely be undetectable.

7.5.3 Morphology

The overall appearance of CTB 87 is similar to G327.1–1.1 (Temim et al. 2015), and MSH 15–56 (Yatsu et al. 2013) which display a cometary morphology. However, both are embedded in SNR thermal shells which we do not detect in our deep

XMM-Newton observation. G327.1–1.1 displays prongs of non-thermal emission extending ahead of the bow-shock which has been proposed to be a limb-brightened cone and is similar to the emission we see extending to the south-east of the putative pulsar. The lack of thermal emission in CTB 87 may be the result of expansion into a low-density medium. Emission from high-temperature, low-density plasma mimics a power-law and the high column density masks any faint soft X-rays.

The brightest radio emission forms a kidney shape with the elbow pointing towards the X-ray peak (Figure 7.7). The X-ray emission likewise displays a cometary morphology with trailing arms which point back towards the radio centre. There are two main accepted possibilities for the source of this morphology. The neutron star may be moving supersonically through the ambient medium, leaving a relic radio nebula behind, and driving a bow shock. Alternatively, the morphology may be due to an interaction with the reverse shock of the SNR shell. In order to drive a bow shock, the ram pressure due to the pulsar's proper motion ($\rho_0 v_{\rm PSR}^2$, where ρ_0 is the density of the ambient medium) must exceed the nebular pressure. Matheson et al. (2013) argued against this due to the unlikely high pulsar velocity needed. To drive a bow-shock, the pulsar must satisfy $v_{\rm PSR} \geq 325 n_0^{2/17} E_{51}^{1/17}$ km s^{-1} (van der Swaluw et al. 2004, where E_{51} is the explosion energy of the supernova and n_0 is the ambient density. The required velocity for the lower limit on density given a hot thermal component with $kT \gtrsim 1$ keV, $\rho \approx 0.05$cm^{-2} (Figure 7.8) is 218 km s^{-1}. Assuming the radio emission is from a relic PWN, the offset between the radio and X-ray peak locations of $\sim 140''$ (see Fig. 6) leads to a maximum age of 19 kyr for motion in the plane of the sky, and older for an arbitrary inclination angle. A bow shock origin also

brings into question the nature of the faint extended emission preceding the pulsar (to the south-east/south, see Figs. 7.1 and 7.3) which is much more pronounced in this *XMM-Newton* observation.

Arguing for the reverse shock scenario proves to be difficult due to the absence of observed thermal X-ray emission. The very low density derived in Section 7.5.2 is consistent with expansion into low-density ejecta expanding into a stellar wind bubble, in agreement with the results of Liu et al. (2018) and Kothes et al. 2019 (in preparation). A reverse shock interaction may however explain the the steep radio spectrum observed from the central kidney-shaped component. This component is embedded in a large diffuse hard-spectrum region which may represent the unperturbed PWN (Kothes et al., in preparation).

7.6 Numerical simulations

The morphology of CTB 87 is reproduced here by means of 2D axisymmetric relativistic hydrodynamical (HD) simulations based on the numerical code PLUTO (Mignone et al., 2007). The aim of this numerical study is to verify how the pulsar parameters inferred from observations match the shape of the compact X-ray nebula, constraining the possible geometry of the system, in particular focusing on reproducing the X-ray spectral index map.

The simulation has a cylindrical grid, with a domain range $z \in [-110, 50]$ ly and $r \in [0, 80]$ ly, corresponding to a 50×25 pc^2 box, and a resolution at the base level of 272×544 cells. Increased resolution near to the pulsar location and at

the shock is obtained by imposing 5 refinement levels thanks to Adaptive Mesh Refinement (AMR) facilities (Mignone et al., 2012), achieving a maximum resolution of 8704×17408 cells. The simulation employs an HLL Riemann solver, a second order Runge-Kutta time integrator and a Van Leer Limiter. The equation of state is set to be ideal, with the appropriate adiabatic index for describing a relativistic plasma ($\gamma_A = 4/3$), and the relativistic nature of the unshocked pulsar wind is ensured by imposing a wind Lorentz factor of 10.

The simulation has the pulsar located at the centre of the grid, and a wind is injected within a small region in its surroundings (details of the wind modeling can be found in Olmi et al. 2015). The interaction of the pulsar wind with the surrounding ejecta of the supernova explosion generates the observed PWN. The variation of the pulsar energy output with time is given by $L(t) = \dot{E}_0/(1 + t/\tau_0)^{(n+1)/(n-1)}$, with $\dot{E}_0$ the initial spin-down energy, n the braking index and τ_0 the spin-down age of the system. Since the pulsar powering the PWN has not yet been identified, the exact properties of the pulsar are not known. Moreover there are no clear indications about the location of the supernova remnant shell.

We have thus considered average values of the parameters as inferred from the spectral study of well known systems (see for example Torres et al. 2014) imposing $E_{\rm SN} = 10^{51}$ erg, $M_{\rm ej} = 12 M_\odot$ and $n = 3$.

The initial spin-down energy $\dot{E}_0 = 5 \times 10^{38}$ erg s^{-1} and spin-down time $\tau_0 = 2150$ yr have been chosen in order to get a spin-down luminosity of $\dot{E} \simeq 4.8 \times 10^{36}$ erg s^{-1} at the age of $\sim$20 kyr, corresponding to a rough average of the values estimated from

the range of X-ray luminosities (see Table 2). Those values are chosen in order to obtain a qualitative matching between the simulation and observations of the compact X-ray nebula. In any case different choices for the parameters are not expected to change the dynamical evolution of the system, ensuring that the characteristic time and radius of the system, as defined in Truelove & McKee (1999), are kept fixed. For example this means that the same results can be obtained considering: $E_{\rm SN} = 5.2 \times 10^{50}$ erg, $M_{\rm ej} = 8.1 M_{\odot}$, $\dot{E}_0 = 9.6 \times 10^{38}$ erg s^{-1} and $\tau_0 = 2000$ yr; or $E_{\rm SN} = 10^{51}$ erg, $M_{\rm ej} = 20 M_{\odot}$, $\dot{E}_0 = 3.3 \times 10^{38}$ erg s^{-1} and $\tau_0 = 3060$ yr.

Based on the analysis of the X-ray observations presented in Matheson et al. (2013), we suggest that the pulsar kick velocity is inclined by $\alpha = 100^{\circ}$ with respect to the plane of the sky, i.e., with an inclination of 10° with respect to the line of sight, and rotated by $\theta \sim 30^{\circ}$ towards the NW direction. The inclination of the line of sight is shown in Fig. 7.9, superposed on a density map, in logarithmic scale. The figure shows that the ambient density is rather low, of the order of $\rho_0 \sim 0.08 - 0.5 \times 10^{-24}$ g/cm^{-3}, in agreement with estimates and compatible with typical values of the ejecta density. According to the described geometry we impose a kick velocity of $v_{\rm PSR} \sim 400$ km/s, in order to match the expected lower limit of the planar velocity (~ 220 km/s). The system is then evolved up to a final age of $t_f = 20000$ yr, in agreement with the prediction from the analysis of the X-ray and radio emission. At this age the PWN has an elongated morphology due to its proper motion with respect to the centre of the explosion and it has already interacted with the SNR reverse shock.

Let us stress here that, from the modelling point of view, the reverse shock

scenario and the bow shock one are similar. The deformation of the PWN morphology produced by an incoming reverse shock moving through a non-uniform medium would produce dynamically the same effect of the proper motion of the pulsar in the ambient (uniform) medium, as considered in the present case. Only the combined case of the proper motion and the anisotropy of the ambient medium could lead to a more complex dynamics (Kolb et al. 2017). Our predictions remain thus valid in the light of our qualitative analysis for both scenarios.

Based on our initialisation values, the radius of the remnant at the present age $t_f = 18.5$ kyr is $R_{\rm SNR} \sim 6 \times 10^{19}$ cm or ~ 20 pc (or ~ 60 ly as can be seen in Fig. 7.9). The pulsar is then located at about $0.5R_{\rm SNR}$, which is close to the transonic limit of $\sim 0.7R_{\rm SNR}$. The radius of the termination shock ($r_{\rm TS}$) can be then roughly estimated from the expression of the typical bow shock stand-off distance, defined as $d_0 = [\dot{E}/(4\pi c \rho_0 {\rm v}_{\rm PSR}^2)]^{1/2}$ based on balance of the wind momentum flux and the ram pressure of the ambient medium with local density ρ_0: $r_{\rm TS} \sim d_0 = 0.06$ pc. This is also in agreement with the direct estimation from dynamic maps, from which the termination shock is $r_{\rm TS} \sim 0.1$ pc. These values are both roughly consistent with the ~ 0.15 pc estimation given in Matheson et al. (2013) from the combination of the distance of the X-ray inner arc to the putative pulsar position ($\sim 5''$) and the estimated distance of the source of 6.1 kpc. This discrepancy of $r_{\rm TS}$ with the X-ray estimate is not significant, given that the uncertainty in the distance of the X-ray inner arc to the pulsar location, possible small variations of the source distance and the resolution of the X-ray maps. Notice moreover that the estimation from the bow shock scenario is strongly dependent on the value of the ambient density, which is

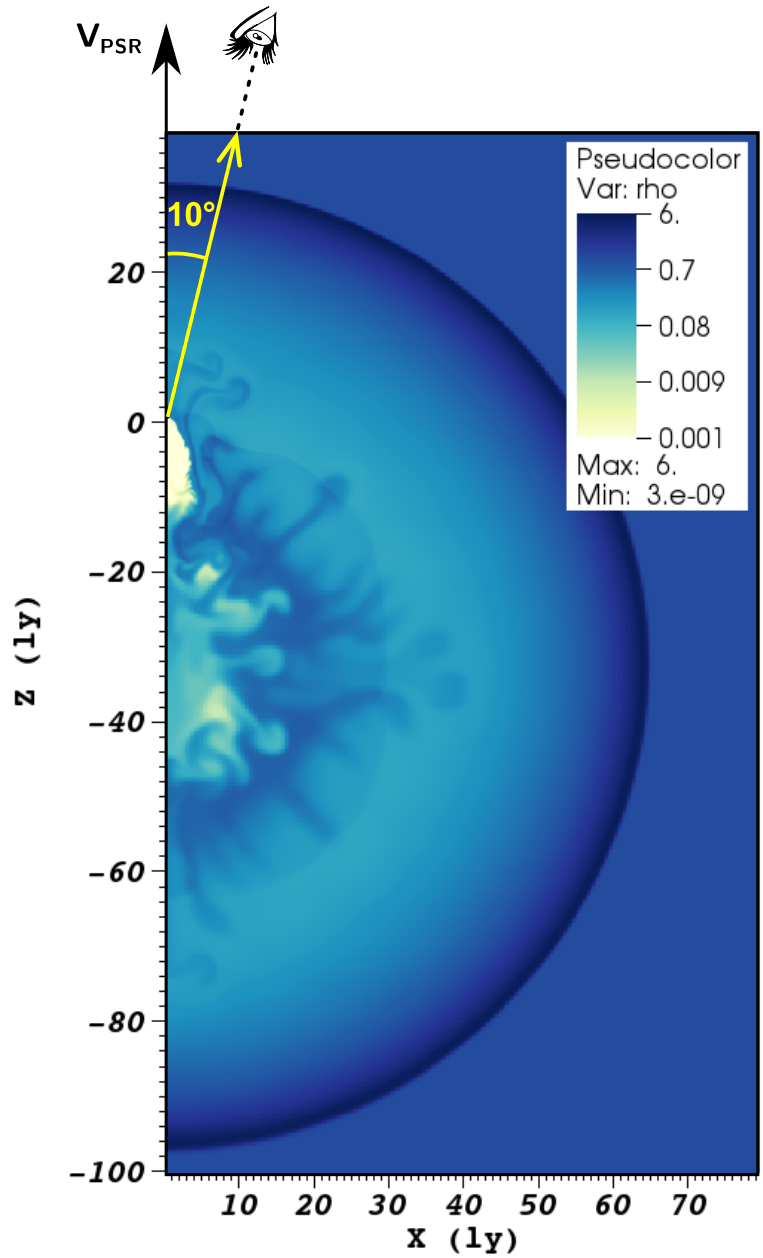

Figure 7.9: Half of a planar map of the density in units of 10^{-24} particles/cm^3, with logarithmic scale. The yellow line indicates the line of sight inclination with respect to the pulsar direction of motion (the z axis).

not known with precision.

Fig. 7.10 shows the synthetic X-ray spectral index map in the 0.5–10 keV range, to be compared with XMM-Newton observations. The synthetic map is built with the following procedure: the emission range is divided into 8 different, equally spaced, frequencies; and for each frequency the emissivity is computed with standard expressions for the synchrotron emission (as can be found for example in Del Zanna et al. 2006). The value of the magnetic field is assumed in the post-processing analysis by imposing that the magnetic pressure is a small fraction of the total pressure. The exact amount is determined by the matching of the size of the emitting area with the one observed in the same energy range. This leads to an average magnetic field in the nebula of the order of $\sim 6\,\mu$G, which is fully compatible with the estimation of a magnetic field of$\sim 50\,\mu$G at the termination shock given in Matheson et al. (2013), since strong magnetic dissipation is expected to take place as the flow moves from the inner to the outer nebula and a drop by a factor of 10 is not unrealistic (Olmi et al. 2016, Olmi 2019). Spectral index maps are then computed following the procedure given in Del Zanna et al. (2006), and the final map is built as the combination of the single maps.

Fig. 7.10 shows a rather impressive agreement with observations, both in terms of the expected shape and of the shell-like distribution of values of the spectral index. The region surrounding the pulsar is well recognizable as the ~ 1.5 spectral index zone and is surrounded by shells of increasing value of the spectral index up to 2.8. The major difference is in the diffuse emission in the farther region, which is also non-axisymmetric in the data and, of course, cannot be exactly reproduced with

2D axisymmetric simulations. In order to reproduce non axisymmetric features the system must be in fact simulated with full 3D geometry. On the other hand, this is computationally rather challenging. Such 3D simulations are very demanding in terms of numerical cost (core-hours and total duration of the simulation, as it is largely discussed in Porth et al. 2014; Olmi et al. 2016), since they require very high resolution at the grid centre, where the pulsar wind is injected. Moreover accounting for such a long evolution as required in the present case (10–20 kyr vs a few hundreds of years, the typical duration of 3D simulations) would require very long time-scales with the actual computational resources, making the 3D approach not feasible for our study. On the other hand the 2D approach was largely shown to be able to match the main morphological properties of PWNe (Blondin et al., 2001; van der Swaluw et al., 2004; Del Zanna et al., 2006; Olmi et al., 2014, 2015), while the HD approximation seems to be adequate in representing evolved systems, where the magnetic field is expected to be quite low and tangled in the bulk of the nebula, due to magnetic dissipation (Temim et al. 2015, Kolb et al. 2017, Olmi 2019). Except for the obvious deformation from a perfect axisymmetric structure, we might thus expect that a 3D magneto-hydrodynamic representation would not change that much the results of the global morphology found with the present approach.

7.7 Conclusions

Using a 125 ks observation with *XMM-Newton*, we do not find evidence of thermal X-ray emission, supporting the scenario for expansion into a stellar wind bubble. We present the first spectral index map of the PWN revealing high-resolution hard

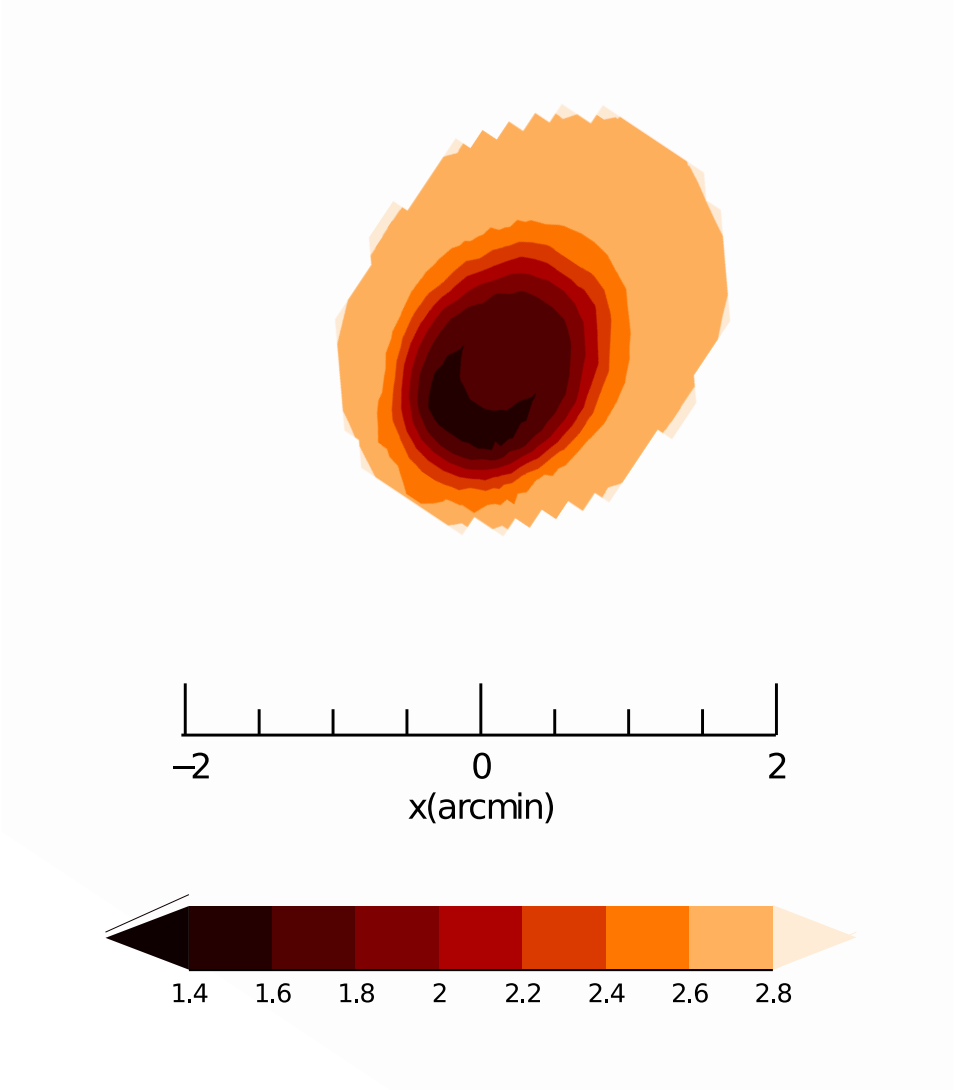

Figure 7.10: Map of the X-ray spectral index of CTB 87 in the 0.5-10 keV band. Value of the spectral index is given as contours of different colours expressed by the scale in the bottom of the map. Dimensions of the system are given in arcminutes. This map must be compared with Fig. 7.6, keeping in mind that the simulation can only reproduce the emission from the compact nebula, while the contribution to the spectral index map from the diffuse nebula is not considered here.

structures close to the pulsar candidate, and an overall steepening of the photon index away from it. We find low-surface brightness emission to the south of the pulsar candidate, which suggests diffusion of particles in that direction. The combined X-ray and radio study of the compact nebula supports the relic PWN scenario resulting from interaction with the reverse shock of an evolved ∼20 kyr PWN.

The geometry of the system is investigated by means of HD numerical simulations. Given the uncertainties in the parameters connected to the PSR and the SNR, we have considered a set of values compatible with average ones from the known PWN catalogue, according with the ranges identified from the multi-wavelength analysis of the system. An investigation of different sets of parameters would be computationally demanding and, in any case, the global morphology of the system is not expected to change if the parameters (i.e., $E_{\rm SN}$, $M_{\rm ej}$ and τ_0) are varied keeping constant the characteristic time and radius as defined in Truelove & McKee (1999). Moreover the primary intent here was to reproduce the morphology of the X-ray compact nebula, especially in terms of the spectral index map. These give us some indications on the possible geometry of the system on the plane on the sky, which would hopefully be better constrained in the future with new observations. For instance variations of the inclination angle and PSR velocity can be easily accounted for in the same model, without affecting heavily the predictions. The impressive agreement of the spectral index map with the *XMM-Newton* observations supports the scenario of an evolved and elongated PWN moving towards the observer through low-density SNR material.

Timing and deeper observations extending beyond the radio nebula are needed to explore open questions about this system. In particular the spin properties

of the pulsar candidate and a measurement of its proper motion will be crucial. Furthermore, a deeper X-ray spectroscopic study extending to larger distances from the pulsar candidate may reveal weak thermal X-ray emission from this system.

Acknowledgements

This research was supported by the Natural Sciences and Engineering Research Council of Canada (NSERC) through the Discovery Grants and the Canada Research Chairs Programs (S.S.H.). B.G. acknowledges support from a University of Manitoba Graduate Scholarship. E.A., N.B. and B.O. wish to acknowledge financial support from the "Accordo attuativo ASI-INAF n. 2017-14-H.0, progetto: *on the escape of cosmic rays and their impact on the background plasma*", the SKA-CTA-INAF and INAF-MAINSTREAM projects. We acknowledge an earlier contribution by H. Matheson towards the XMM proposal. We thank the referee for comments that helped improve the paper. This study made use of NASA's Astrophysics Data System and ESA's *XMM-Newton* facility.

Chapter 8

Observing Variability in PWNe

The previous two chapters involved searching for and fitting the very faint emission from a surrounding shell. To do this, all available observations were stacked, and spectra were fit simultaneously to improve the statistics. This technique is commonly used in PWN research unless the emission is expected to be variable either through indication of significant brightening or motion of features between observations.

Excluding outburst events, PWNe are remarkably stable in their overall emission. The energy of the pulsar wind originates from the kinetic energy lost from the spin-down of the rotating neutron star, it is therefore natural to expect the energy injection to be fairly regular and for the emission to reach a stable equilibrium. Combining this with the travel time for any disturbances in the parsec scale size of PWNe leads to the assumption that the X-ray emission should be effectively unchanged on timescales of a few years. Often observations taken years apart are merged or fit simultaneously to improve statistics when fitting resolved features such as termination shocks or jets. In the spectral map of G21.5–0.9 we present

in chapter 6 all available observations were fit simultaneously to achieve the best possible statistics. While the brightness images showed minimal variability, we show here that the assumption that the spectral maps would remain constant does not hold true. Spectral maps of G21.5–0.9 generated from observations grouped by year showed the development of an outflow like feature of hardened emission. Here we investigate whether this is a feature unique to G21.5–0.9 or common among other PWNe. We present a *Chandra* X-ray study of the young PWNe in G21.5–0.9, Kes 75, G54.1+0.3, G11.2–0.3, and 3C58. With spectral map analysis we find previously unknown variability in all, and examine the effect of known outbursts on the large scale nebula emission. The following contains text and images from Guest, B., & Safi-Harb, S., *Revealing Hidden Variability in PWNe with Photon Index Maps*. Monthly Notices of the Royal Astronomical Society. Under revision.

8.1 Introduction

The theory of pulsar winds for many years was assumed to closely follow the work of Kennel & Coroniti (1984a,b) who derived a spherically symmetric MHD model for the evolution, and emission profile for a PWN with synchrotron losses. High resolution X-ray observations (e.g. Chapter 6) have shown that the spectral index ($\alpha, S_\nu \sim \nu^{-\alpha}$) in resolved PWNe does not increase as rapidly as predicted by the KC84 theory. Alternative models have been proposed such as diffusion (Tang & Chevalier (2012)), extending the MHD analysis to 3-D (Del Zanna et al. (2018)), or a combination of both (Porth et al. (2016)). Spectral maps trace the distribution of particles in both energy and position, and X-ray emitting electrons indicate acceleration locations due

to their short synchrotron lifetimes. Comparison of observed and simulated spectral maps allow an understanding and testing of pulsar wind propagation models.

Observing variability within pulsar wind nebulae has previously been limited to cases of significant brightening, or the few instances where transient features are interpreted in terms of intrinsic motion (Pavlov et al., 2001; Hester et al., 2002; DeLaney et al., 2006) or associated with an occasional magnetar-like outburst from the pulsar (Blumer et al., 2017; Younes et al., 2016; Kumar & Safi-Harb, 2008; Ng et al., 2008). In particular, jet and torus morphology have been only visible in cases of differing brightness with respect to the surrounding nebula and favourable alignment with our line of sight. Spectral map analysis involves binning observations with an adaptive algorithm to meet a signal to noise ratio limit and colouring the results based on the desired model parameter fits. Minute changes in spectral index can become apparent even in cases with relatively few photon counts. In this work, we show that this technique reveals previously hidden structures and changes in the emitting particle spectrum where traditional RGB and brightness images have provided little insight.

8.2 Observations and Methods

8.2.1 Observations

G21.5–0.9

G21.5-0.9 (Figure 8.1 (1)) is a plerionic composite supernova remnant (SNR), and is discussed at length in Chapter 6. Due to its use as a calibration target for the

Chandra X-ray Observatory, we have observations spanning 15 years making this the ideal starting point for our analysis.

Kes 75

Kes 75 (Figure 8.1 (2)) is a plerionic composite SNR at a distance of 5.8 kpc (Verbiest et al., 2012). The PWN measures $\sim 26'' \times 20''$ with thermal emission from the supernova remnant shell seen in clumps to the south (Helfand et al., 2003). The PWN displays inner structure including a jet directed to the south (Morton et al., 2007). The 324 ms pulsar (Gotthelf et al., 2000) emitted several magnetar-like outbursts from 2000–2006 (Gavriil et al., 2008; Kumar & Safi-Harb, 2008). This resulted in a softening of the spectrum of the pulsar and a brightening of the southern jet from 2000 to 2006 (Kumar & Safi-Harb, 2008; Ng et al., 2008). Reynolds et al. (2018) found a PWN expansion age of 400 ± 40 yr making Kes 75 the youngest known Galactic PWN.

G54.1+0.3

G54.1+0.3 (Figure 8.1 (3)) is a plerionic SNR at an estimated distance of 6.3 kpc (Shan et al., 2018). The SNR displays a bright point source, surrounding ring, and jet-like elongations to the east and west (Lu et al., 2002). While the X-ray emission is all non-thermal, an infrared shell was found by (Temim et al., 2010) who interpreted the emission as ejecta dust heated by early type stars within the expanding SNR. The 137 ms pulsar powering the nebula was discovered in the radio band by (Camilo et al., 2002), who calculated a characteristic age of 2900 years.

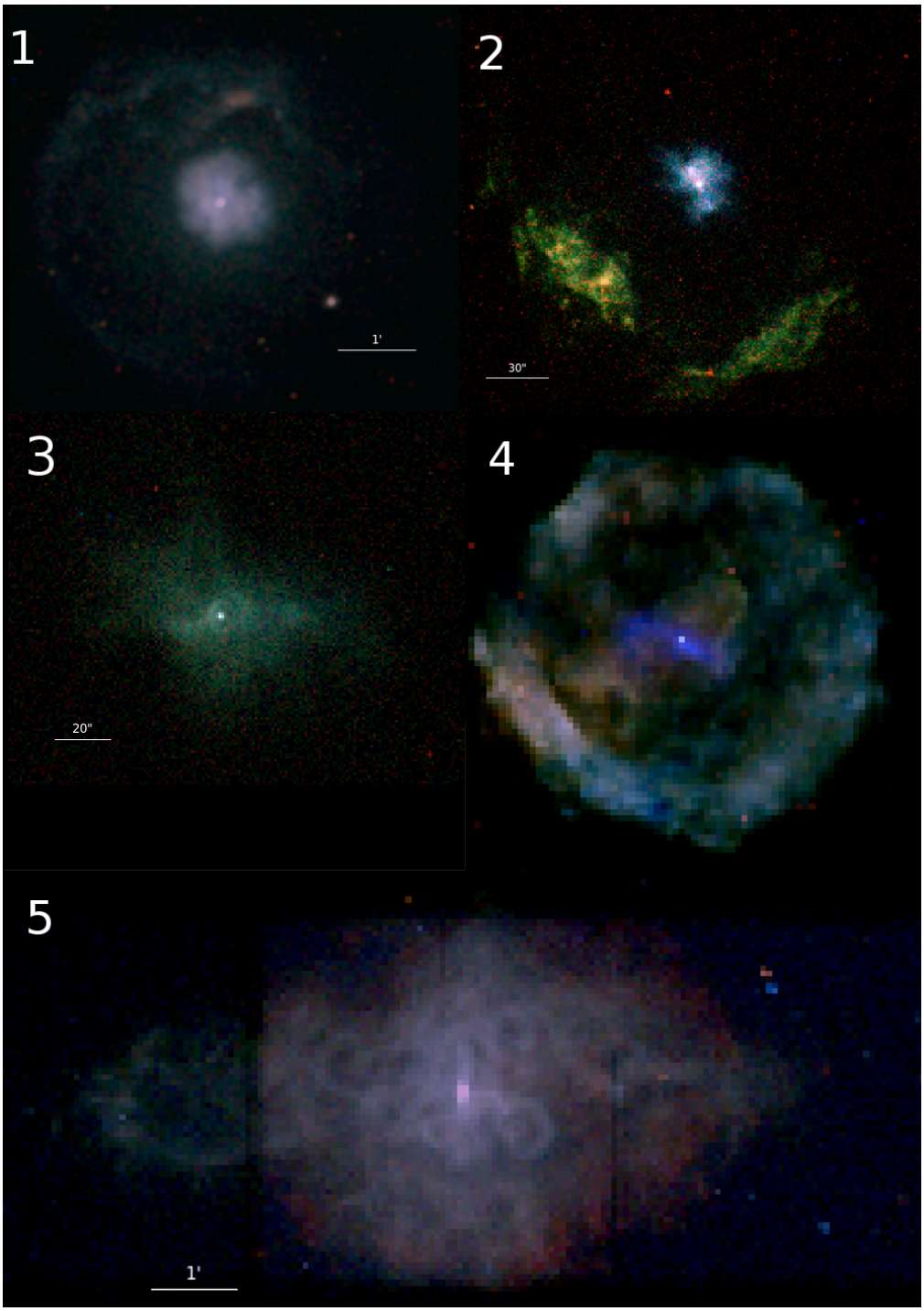

Figure 8.1: *Chandra* images of the SNRs observed: (1) G21.5–0.9, (2) Kes 75, (3) G54.1+0.3, (4) G11.2–0.3, and (5) 3C 58. The RGB images are coloured using the energy ranges 0.5–1.2 keV, 1.2–2 keV, and 2–7 keV for red, green, and blue, respectively.

G11.2–0.3

G11.2–0.3 (Figure 8.1 (4)) is a plerionic composite SNR (Vasisht et al., 1996) located at a distance of 5.5–7 kpc (Minter et al., 2008)). The PWN is powered by a 65 ms pulsar discovered by (Torii et al., 1997) using *ASCA* X-ray observations. The PWN is elongated with jet-like morphology and broadening at the centre consistent with a torus viewed edge-on (Kaspi et al., 2001; Roberts et al., 2003). The SNR shell displays a circular morphology. Borkowski et al. (2016) measured expansion of the shell from 2000–2013. Free expansion places an upper limit of the age as 3600 years however, they argue due to the advanced dynamical age where nearly all the ejecta have been shocked, significant deceleration must have occurred. The unknown density distribution of the surrounding medium leads to age estimates of 1400–2400 years.

3C 58

3C 58 (Figure 8.1 (5)) is a Crab-like SNR possibly associated with the historical supernova event of 1181 C.E. (Stephenson, 1971) and located at a distance of 2 kpc (Kothes, 2013, 2016). The 66 ms pulsar was discovered by (Murray et al., 2002). The PWN displays a central jet and torus morphology surrounding the pulsar, the nebula is full of loops and twists, while the outer PWN is embedded in thermal X-ray emission enriched with Ne and Mg suggesting its origin as swept-up ejecta (Slane et al., 2004; Gotthelf et al., 2007).

The list of observations including date and exposure time used in this analysis is provided in Table 8.1.

Table 8.1: Observation ID, date, and exposure time of the *Chandra* ACIS observations used. Data were collected from the Chandra Data Archive (https://cda.harvard.edu/chaser/).

Obs ID	Date of Obs	Exp Time (ks)
G21.5–0.9		
1433	1999-11-15	14.97
1717	2000-05-23	7.54
1726	2000-05-24	7.57
1725	2000-05-24	7.57
1838	2000-09-02	7.85
1839	2000-09-02	7.66
2872	2002-09-13	9.84
2873	2002-09-14	9.83
4353	2003-05-15	9.36
3699	2003-11-09	9.7
5166	2004-03-14	10.02
5165	2004-03-26	9.55
5158	2005-02-26	10
6070	2005-02-26	9.43
6071	2005-02-26	9.64
6740	2006-02-21	9.83
6741	2006-02-22	9.83
8371	2007-05-28	9.92
10644	2009-05-29	9.64
10645	2009-05-29	9.54
10646	2009-05-29	9.54
14263	2012-08-08	9.57
14264	2012-08-10	9.57
16420	2014-05-07	9.57
16421	2014-05-09	9.57
Kes 75		
748	2000-10-15	37.28
7337	2006-06-05	17.37
6686	2006-06-07	54.1
7338	2006-06-09	39.25
7339	2006-06-12	44.11
10938	2009-08-10	44.61
18030	2016-06-08	84.95
18866	2016-06-11	61.46
G11.2–0.3		
780	2000-08-06	19.74
781	2000-10-15	9.97
2322	2000-10-15	4.85
3909	2003-05-10	13.78
3910	2003-06-27	13.78
3911	2003-08-01	14.6
3912	2003-09-08	14.68
14831	2013-05-05	173.02
14830	2013-05-25	58.24
14832	2013-05-26	63.23
15652	2013-09-07	47.93
16323	2013-09-08	45.76
G54.1+0.3		
1983	2001-06-06	38.46
9108	2008-07-10	34.67
9109	2008-07-12	162.25
3C58		
728	2000-09-04	49.95
3832	2003-04-26	135.83
4382	2003-04-23	167.39
4383	2003-04-22	38.73

8.2.2 Methods

A finite number of photon counts are required to fit a spectrum. Typically, regions of interest are selected based on the appearance of a brightness or RGB colour image. Here we use the adaptive binning software *CONTBIN* (Sanders, 2006) to generate regions following the surface brightness of an input image and meeting a specified signal limit. This creates puzzle-like pieces that fit together completely covering the area of interest while leaving no gaps and allowing a study of features that may have been inadvertently averaged over using different methods. Spectra are then extracted and fit with the X-ray spectral fitting software *XSPEC* (Arnaud, 1996). We assume that the column density (TBABS model in XSPEC with abundances provided by Wilms et al. (2000a)) does not vary over the size of the nebula and freeze this parameter to the best fit value derived from the PWN spectrum. The regions are then coloured according to the values of the desired model parameter to generate maps. When the emission is not purely non-thermal (such as in 3C 58) we can identify the regions where a single component model is insufficient through the construction of a reduced chi-square map and add the thermal component where necessary. Additionally, in cases where there is significant contribution to the surface brightness from the thermal emission associated with the SNR (such as in G11.2–0.3) we restrict our input image and fitting range to the hard X-ray band from 3.5 – 8 keV where the non-thermal synchrotron emission from the PWN is dominant.

We investigate changes by creating a merged image to use as the input for region creation. We choose to use a merged image as input to avoid biasing our results towards a single observation. We choose a signal limit such that even the shortest

observation will yield a few hundred counts in each region while also attempting to conserve as much inherent structure through keeping the regions as small as possible. Background was taken from regions outside of the remnant while remaining on the same ACIS chip. In each case the background scaled to the individual region sizes is expected to contribute minimally to the overall total. This combined with our limit of at least ~ 300 counts per spectrum allows for the use of chi-squared statistics. Spectra were then extracted from the same set of regions for each observation, and those from a common year were fit simultaneously allowing a direct comparison. Significant changes were identified through creating error maps using the same process as above. Regions are coloured according to the significance of the difference. This was calculated using the following expression: $(\Gamma_1 - \Gamma_2)/\sqrt{\sigma_1^2 + \sigma_2^2}$, where Γ is the best-fit photon index for each observation period, and σ is the 1-sigma error value associated with each fit. Differences are deemed significant if they exceed the 2-sigma level.

8.2.3 Analysis

G21.5–0.9

We group observations by year to create individual maps and look for variability in the photon index. Figure 8.2 shows the spectral maps by year of observation. Figures 8.3 and 8.4 show the associated photon index errors and reduced chi-squared values. The region of hard photon index to the north of the pulsar found in the combined map of Guest et al. (2019) is not visible in the 1999 observation. It appears hardest in February 2005, and seems to show variability at least on the order of the observation

intervals (Table 8.1); then hardening again in 2007 and 2012 and softening by the final 2014 observation. To check if these changes are statistically meaningful, we create significance images. Figure 8.5 shows the differences between the 2005 observations where the plume spectrum is the hardest and the 2000 observations. The plume is clearly visible as a region of significant hardening while there is also a region to the south in line with a counter jet that has softened. Figure 8.6 shows the significant differences over year timescales.

A comparison with brightness variability is shown in Figure 8.7. The count rate of photons s^{-1} using the same regions is displayed similarly to the spectral maps where darker colours indicate a larger count rate. To mimic the simultaneous fitting of observations of the same year, corresponding individual count rates are averaged. The plume to the north of the pulsar appears as the only clear location of variability. The increase in count rate does not seem to correlate with a harder spectrum, rather the brightening appears to correspond with a softening of the spectrum.

Kes 75

To measure the column density, spectra were extracted from a 35 arcsecond radius centred on the pulsar. The spectra were then fit simultaneously with an absorbed power-law with a single column density while allowing the photon index and power-law normalizations to vary between the observation years. The singular column density value found from this fitting was then held constant for each individual region fit in the subsequent spectral maps. We investigate the effects of allowing an observation variable column density and its relation to detector contamination in

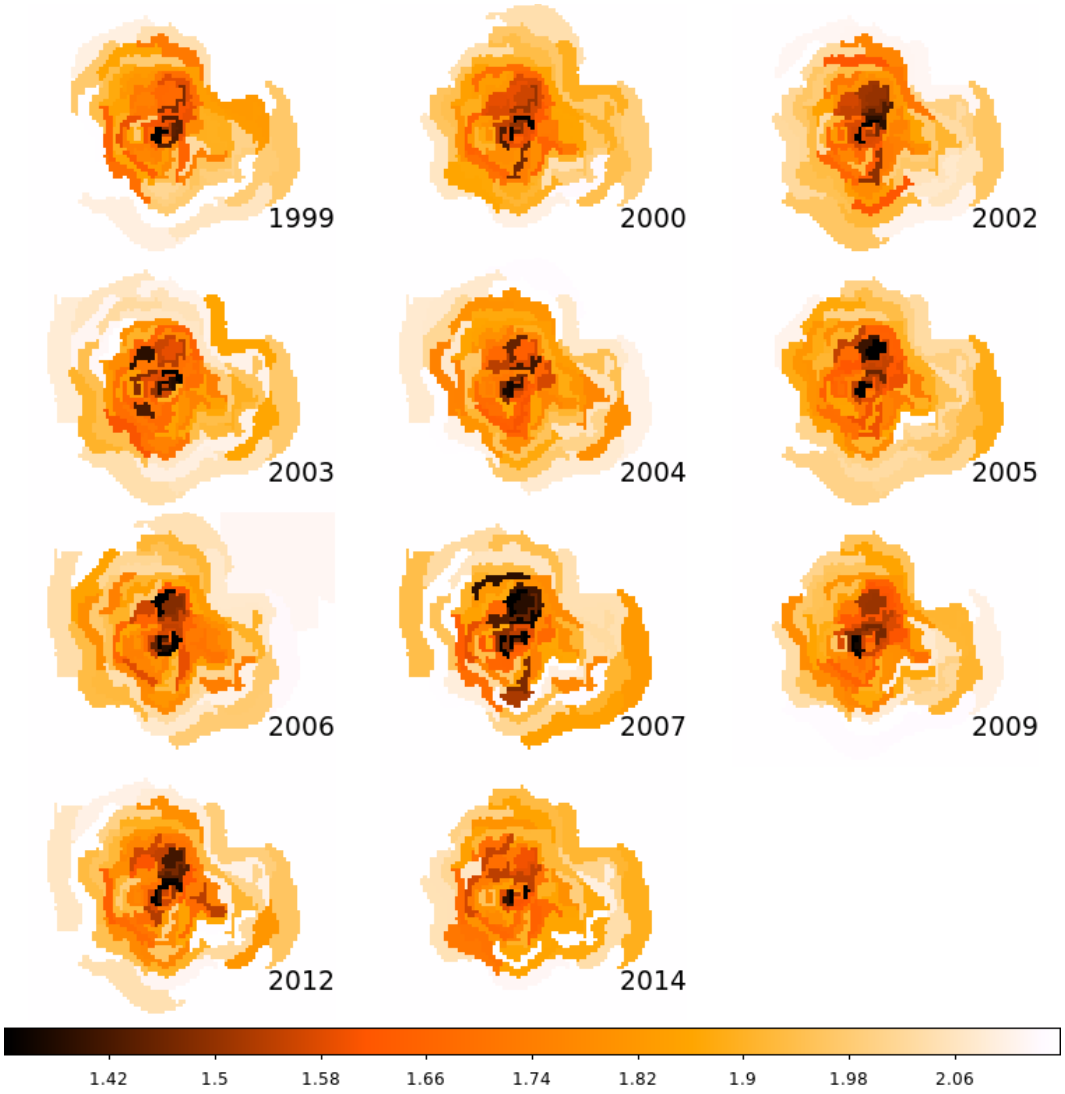

Figure 8.2: Photon index map of G21.5–0.9. The plume of hard emission to the north of the pulsar does not appear in the first year of observations and becomes more noticeable with time, reaching its hardest spectrum in the February 2005 observations.

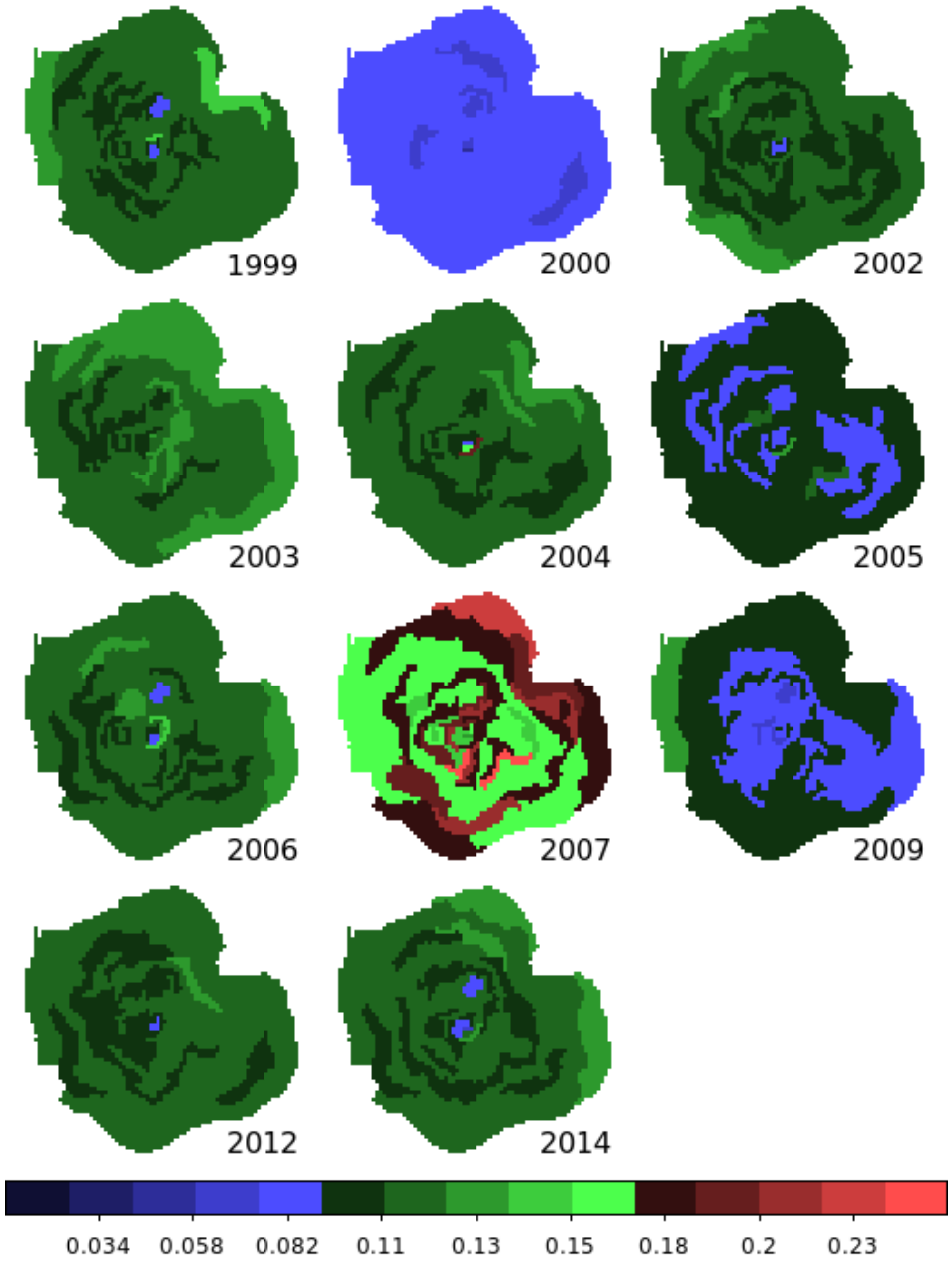

Figure 8.3: $1-\sigma$ error values of the photon index associated with the fits shown in Figure 8.2.

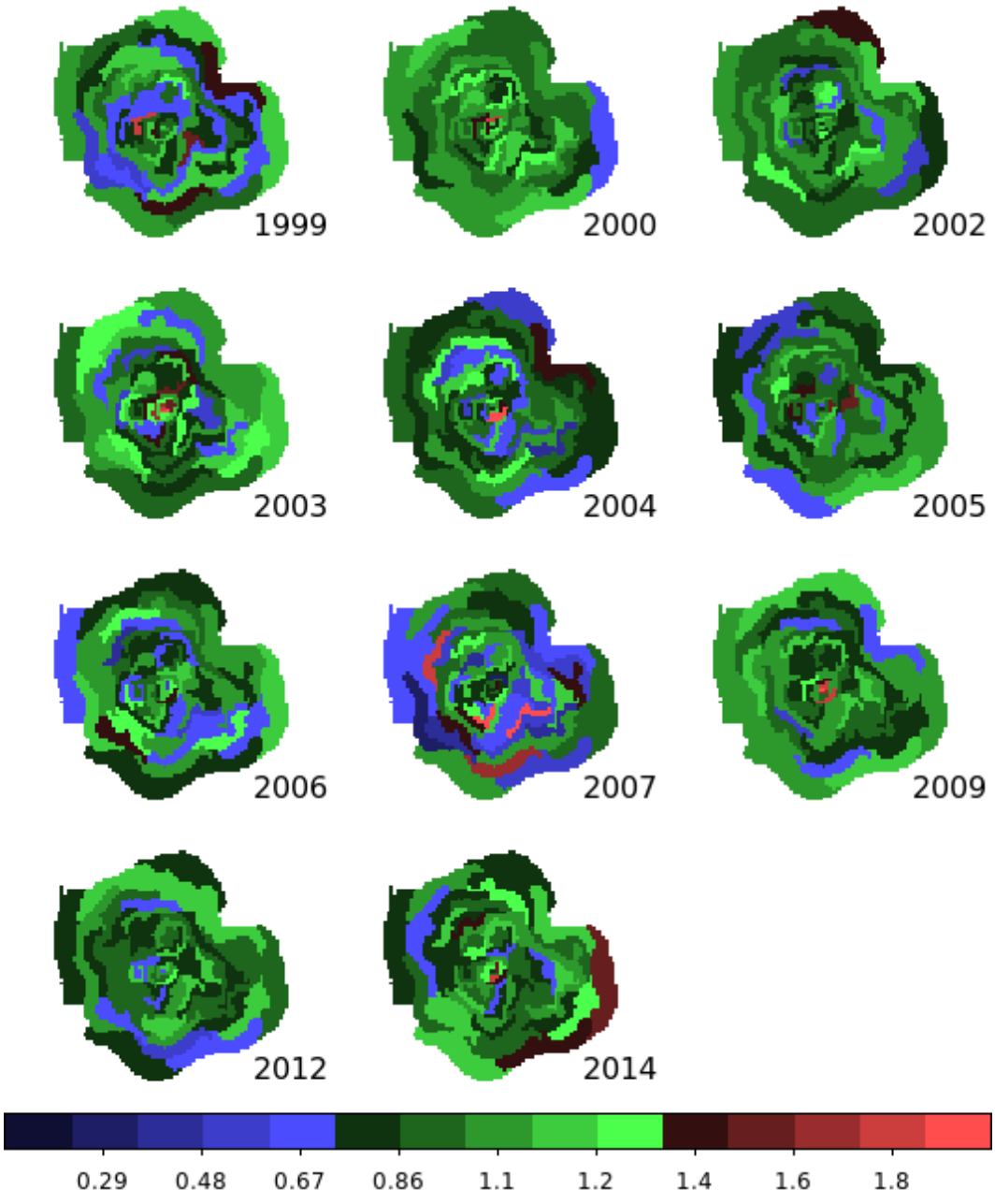

Figure 8.4: Reduced chi-squared values associated with the fits shown in Figure 8.2.

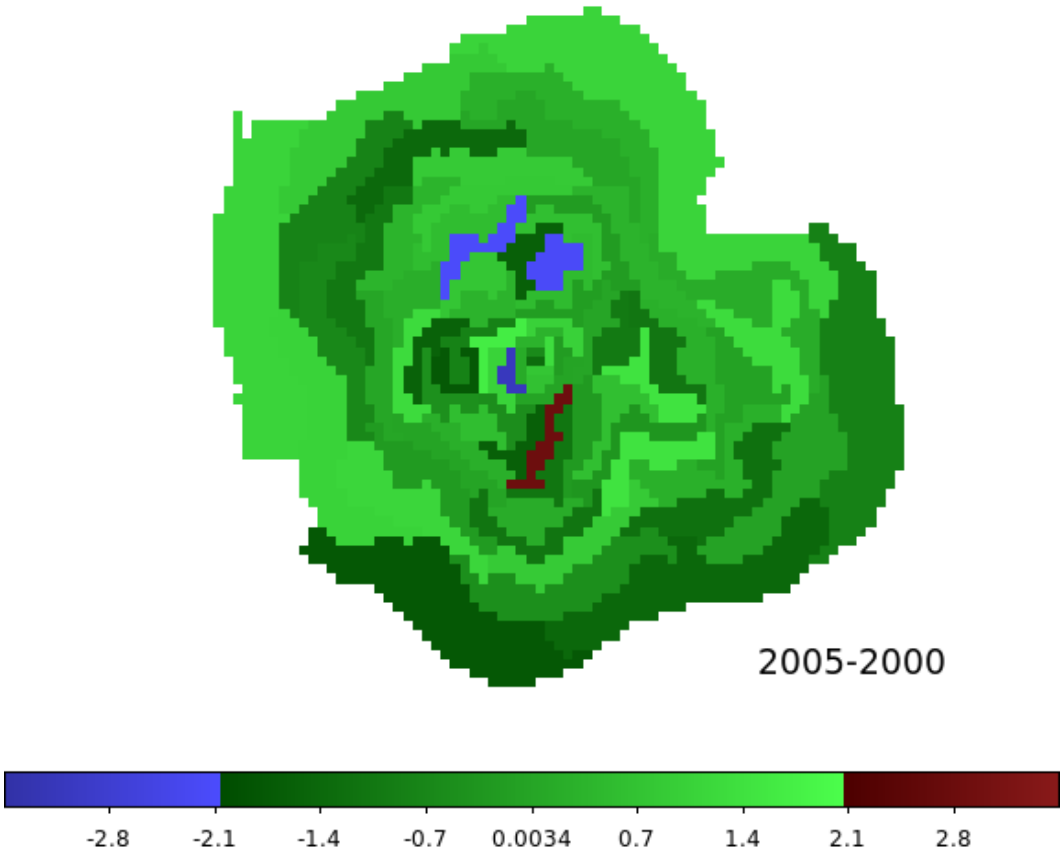

Figure 8.5: G21.5–0.9 significance map showing the changes in photon index between observations taken in 2005 and earlier observations from 2000.

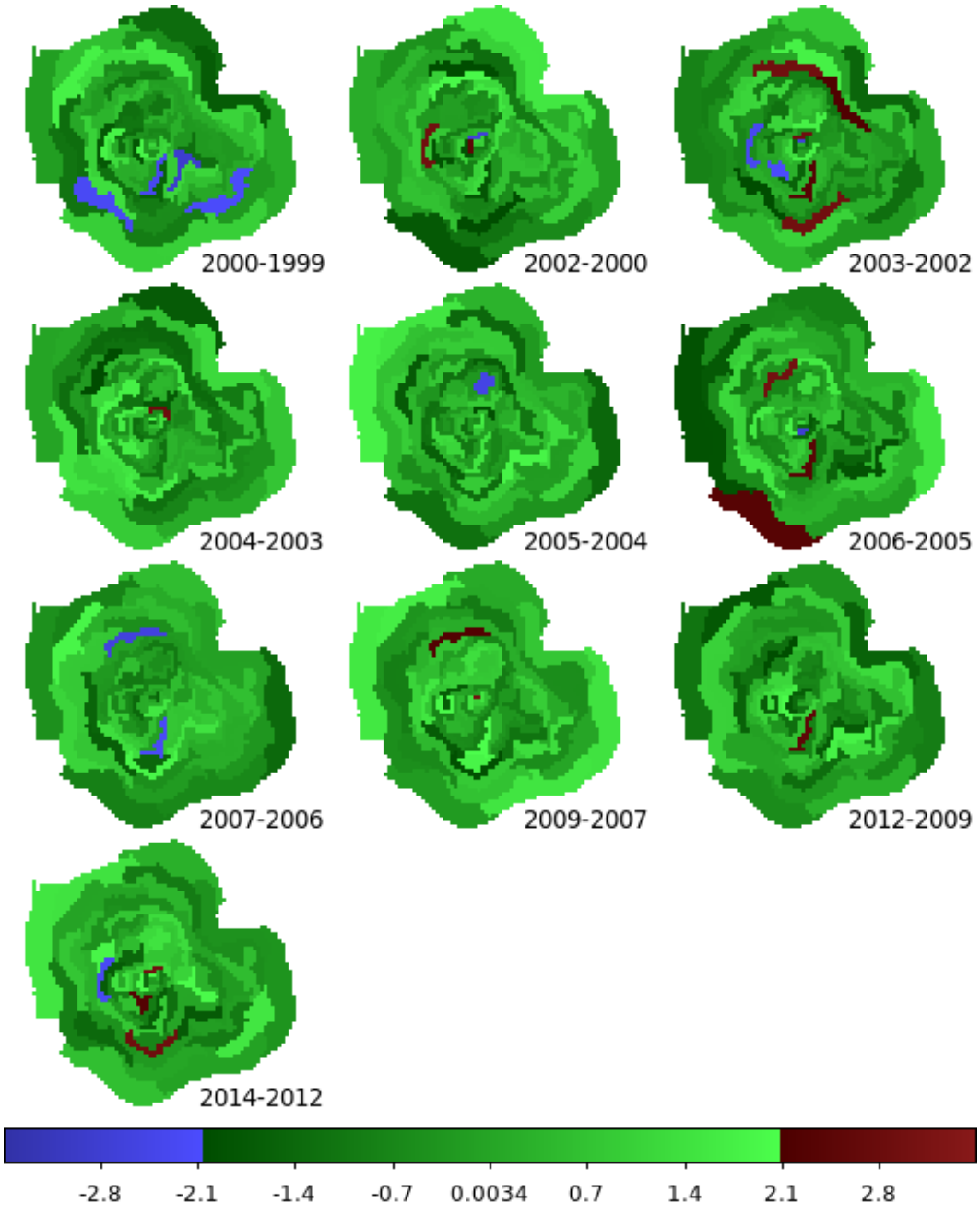

Figure 8.6: Significance map of G21.5–0.9 showing the changes in photon index on year-timescales.

Figure 8.7: Count rate maps of G21.5–0.9 (in units of photons s^{-1}). Darker colours indicate a higher count rate. For years with multiple observations, the individual count rates are averaged between observations.

section 8.3.2. Figure 8.8 shows the evolution of the Kes 75 spectral maps. Figures 8.9 and 8.10 show the associated photon index error and the reduced chi-squared values. The southern jet is observed to have the hardest spectrum along with a counter jet in the 2006 observations. In agreement with (Ng et al., 2008) the hardest region of the jet does not occur closest to the pulsar, rather there is a gap which shows a softer spectral index which is symmetric around the pulsar. The PWN was observed 4 times for 155 ks over a few days in 2006 and twice for 146 ks in 2016. These observations when fit simultaneously offer tighter constraints than the single observations in 2000 and 2009. We therefore look for significant changes between the 2006 and 2016 observations. Figure 8.11 shows the significance map. There is significant softening in the jet and direction of the counter jet, while the rest of the PWN remains largely unchanged. We look for changes in the greater nebula through the radial spectral analysis shown in Figure 8.12. Spectra were extracted from rings centred on the pulsar and fit with an absorbed power-law. The central region has been corrected for pile-up (Section 8.3.1). The softening of the pulsar spectrum is observed post outburst in 2006 in agreement with the previous study of Kumar & Safi-Harb (2008), and returns to the pre-outburst levels by 2009. Despite the significant changes seen in the spectral maps, the radial profiles do not reveal similar variations between observations in the nebula.

G54.1+0.3

The interesting morphology of G54.1+0.3 with resolved torus and clumpy jets provide an ideal target for spectral map analysis. We see evidence of softening of the torus,

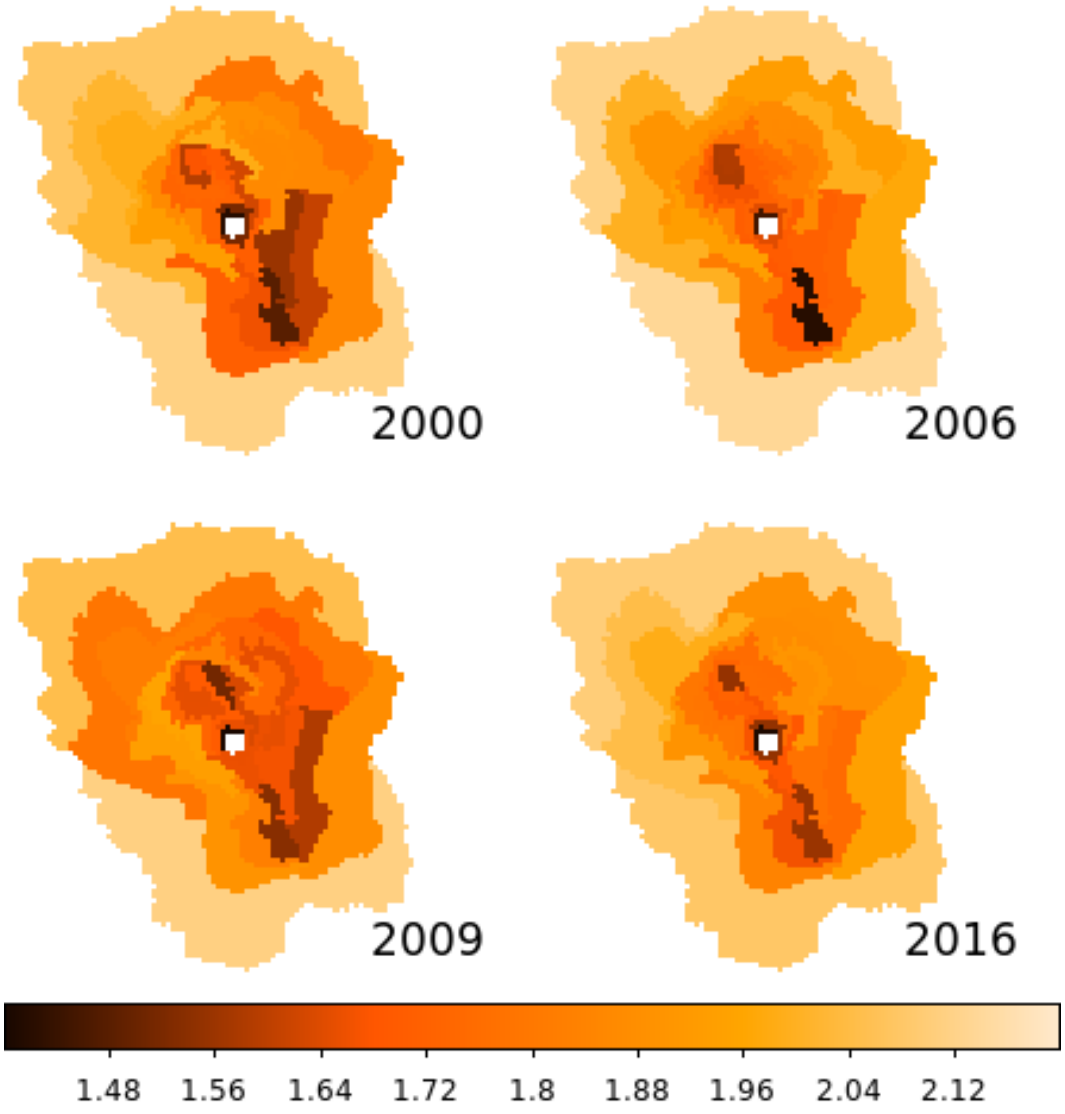

Figure 8.8: Photon index maps vs time for Kes 75. Variability is observed in the jet and surrounding nebula.

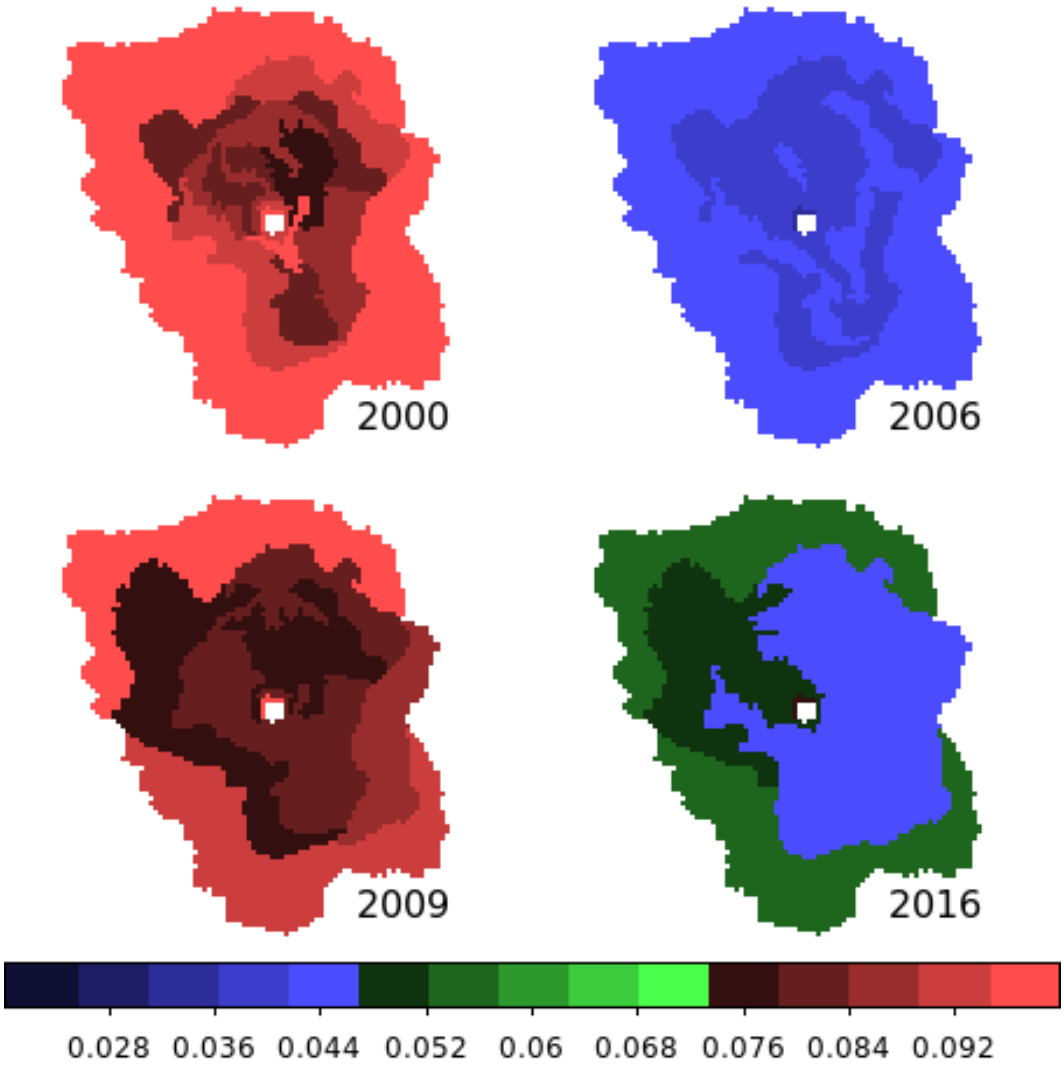

Figure 8.9: $1-\sigma$ error values in the photon index associated with Figure 8.8.

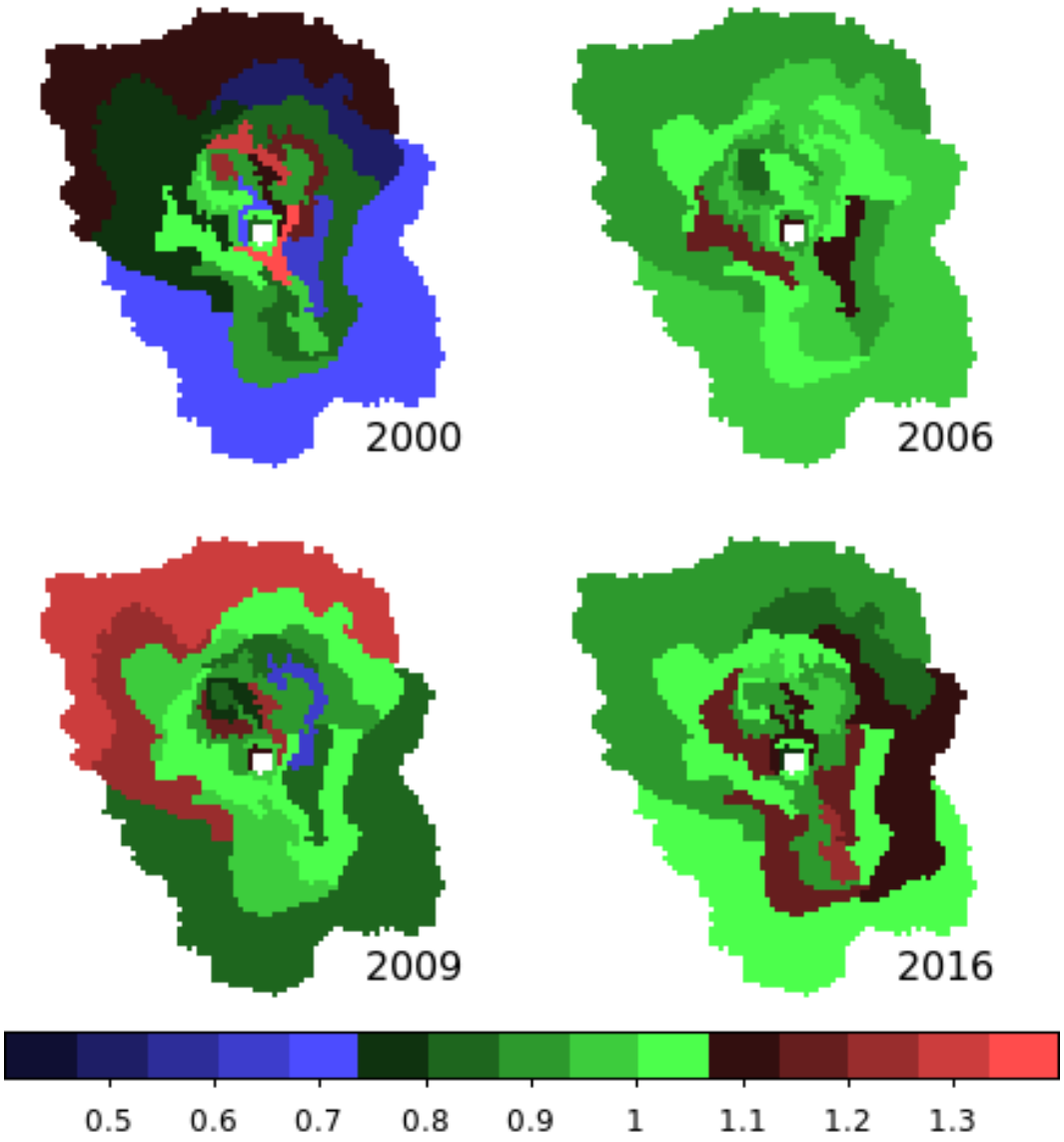

Figure 8.10: Reduced chi-squared values of the fits shown in Figure 8.8.

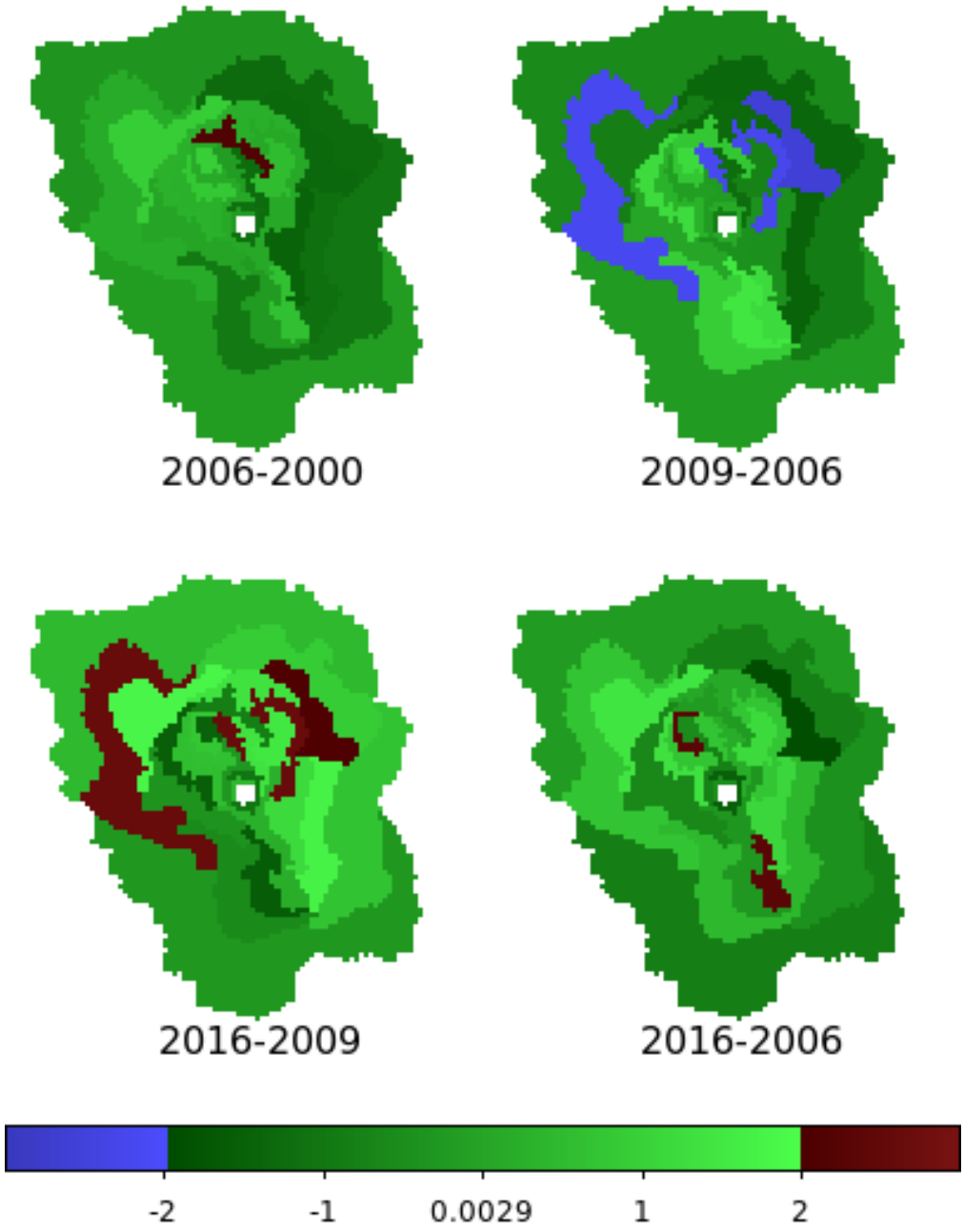

Figure 8.11: Significance maps of Kes 75. Positive (negative) values correspond to softened (hardened) photon index. The southern jet is visible as a region of softened emission along with a region to the north of the counter jet.

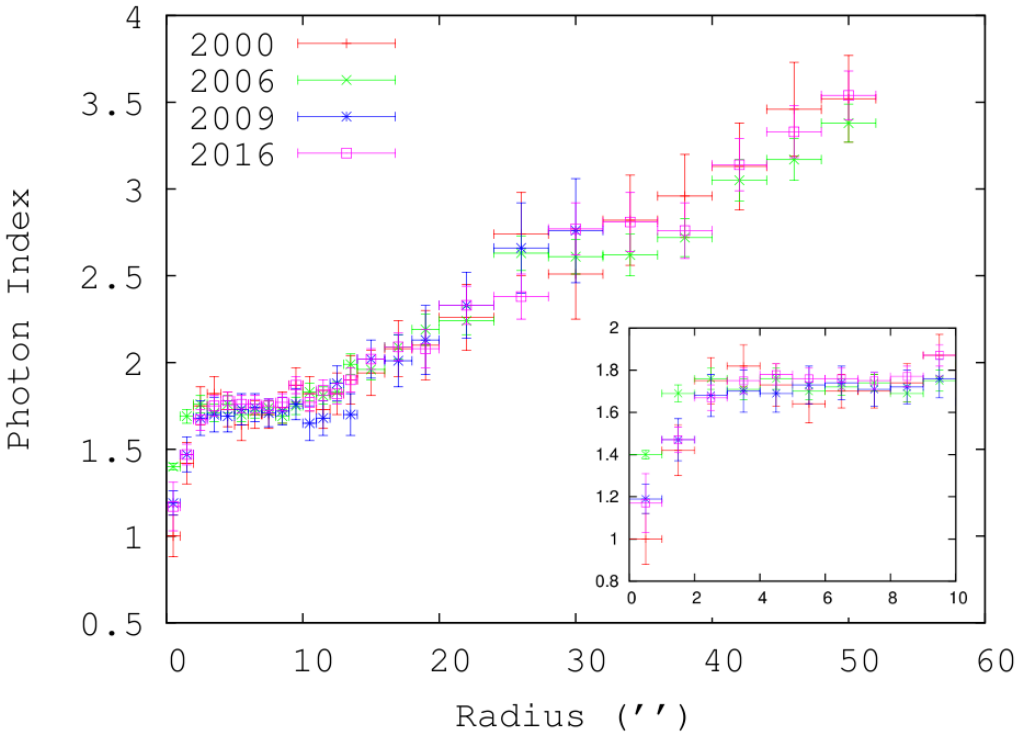

Figure 8.12: Kes 75 radial spectral profile. The radially averaged spectral index does not change significantly with time over 16 years of observations. The softening of the pulsar emission post outburst is visible however there are no long lasting effects in the nebula. The 2009 profile extends only to 30" due to the position on the ACIS detector.

most notably on the eastern side and the western jet (Figure 8.13). Unfortunately, the short observation from 2001 does not allow us to constrain the indices to the degree required to determine if significant changes have occurred (Figures 8.14 and 8.16). The reduced chi-squared values are shown in Figure 8.15.

G11.2–0.3

The significant thermal emission from the SNR shell fills the remnant and dominates the low energy band with a significant line apparent near 3 keV (Figure 8.17). We therefore filter the input image and spectral fitting range to $3.5 - 8$ keV to filter out the non-thermal emission from the PWN (Figure 8.18). The spectral maps appear to show changes with time (Figure 8.19), however all of the differences are well within the error limits. This is likely due to the relative brevity of the 2000 and 2003 observations leading to large error ranges in the accompanying spectra (Figure 8.20). Fitting all observations simultaneously to produce a single spectral map merely reproduces the 2013 map which supports this statement. The reduced chi-squared values are shown in Figure 8.21.

3C 58

When fit with a single power-law model, the map of reduced chi-squared (Figure 8.22) displays regions where the fit is poor near the edge of the PWN indicating the single power-law model is inadequate. We add a VPSHOCK model to describe the thermal emission which drastically improves the fit. Comparing the spectral maps from 2000 and 2003 (Figure 8.23) paired with the significance image (Figure 8.24)

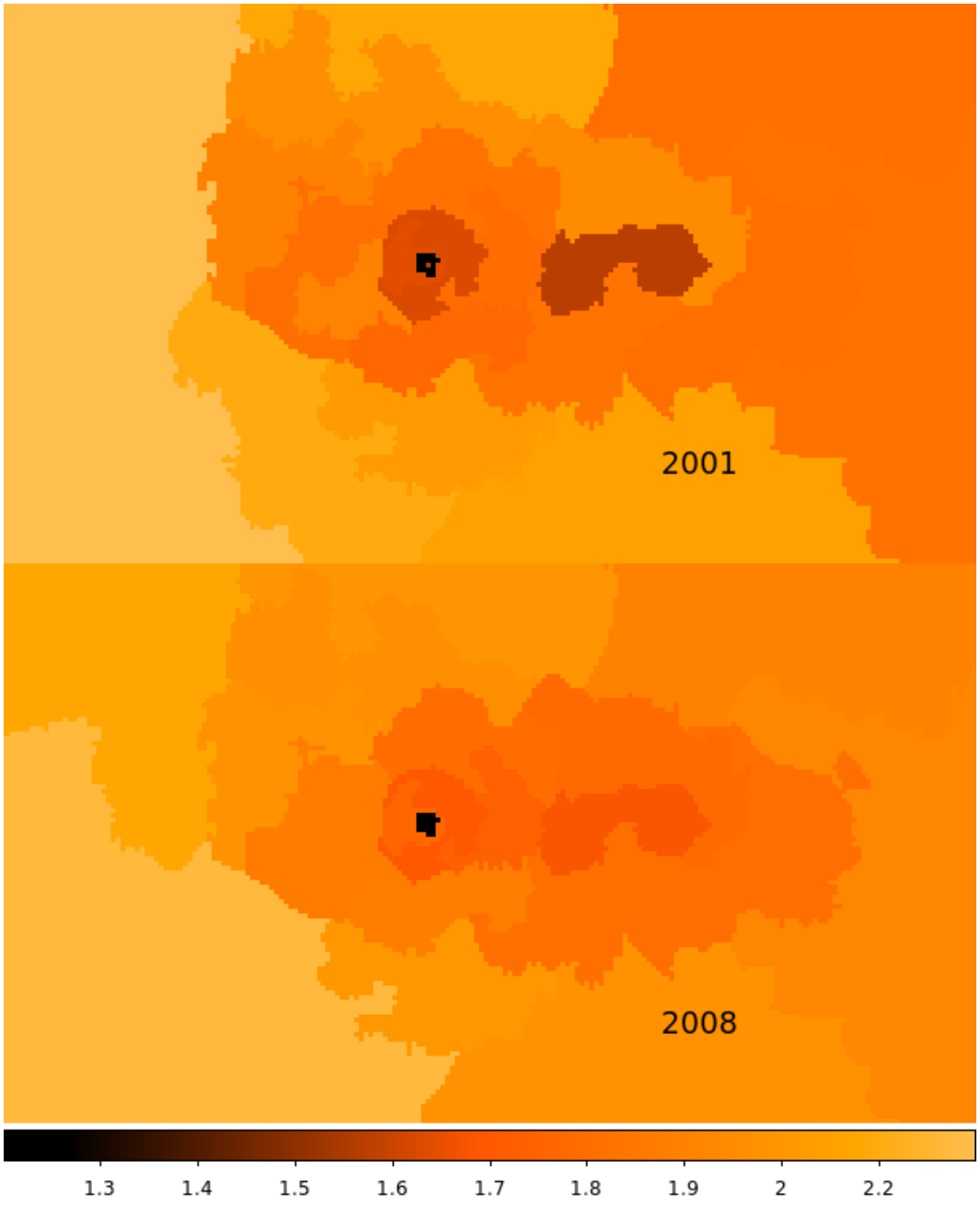

Figure 8.13: G54.1+0.3 spectral maps. While there appears to be some evidence of softening in the torus and western jet the difference is not considered significant (Figure 8.16).

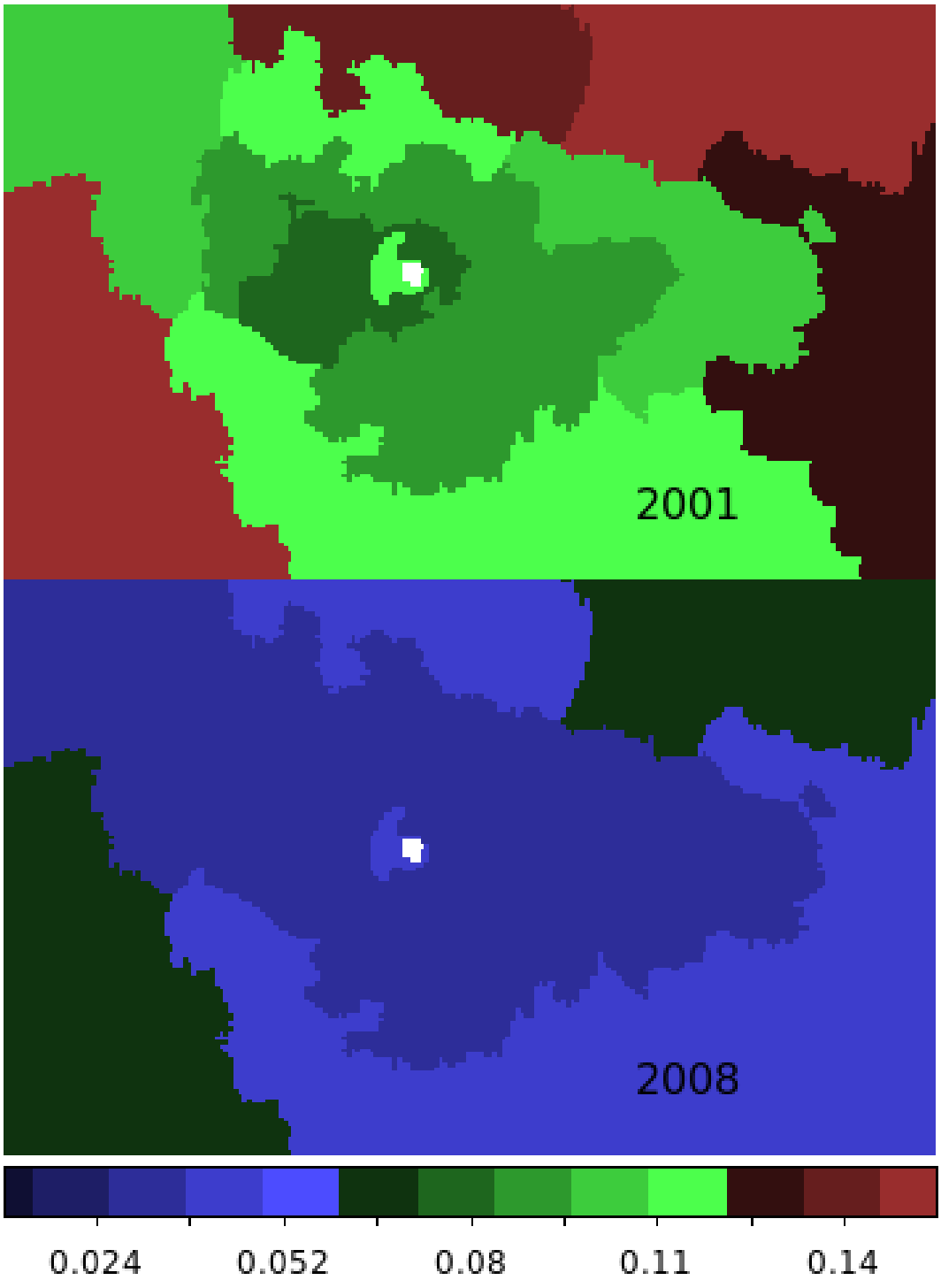

Figure 8.14: $1-\sigma$ errors of the photon index associated with the fits shown in Figure 8.13.

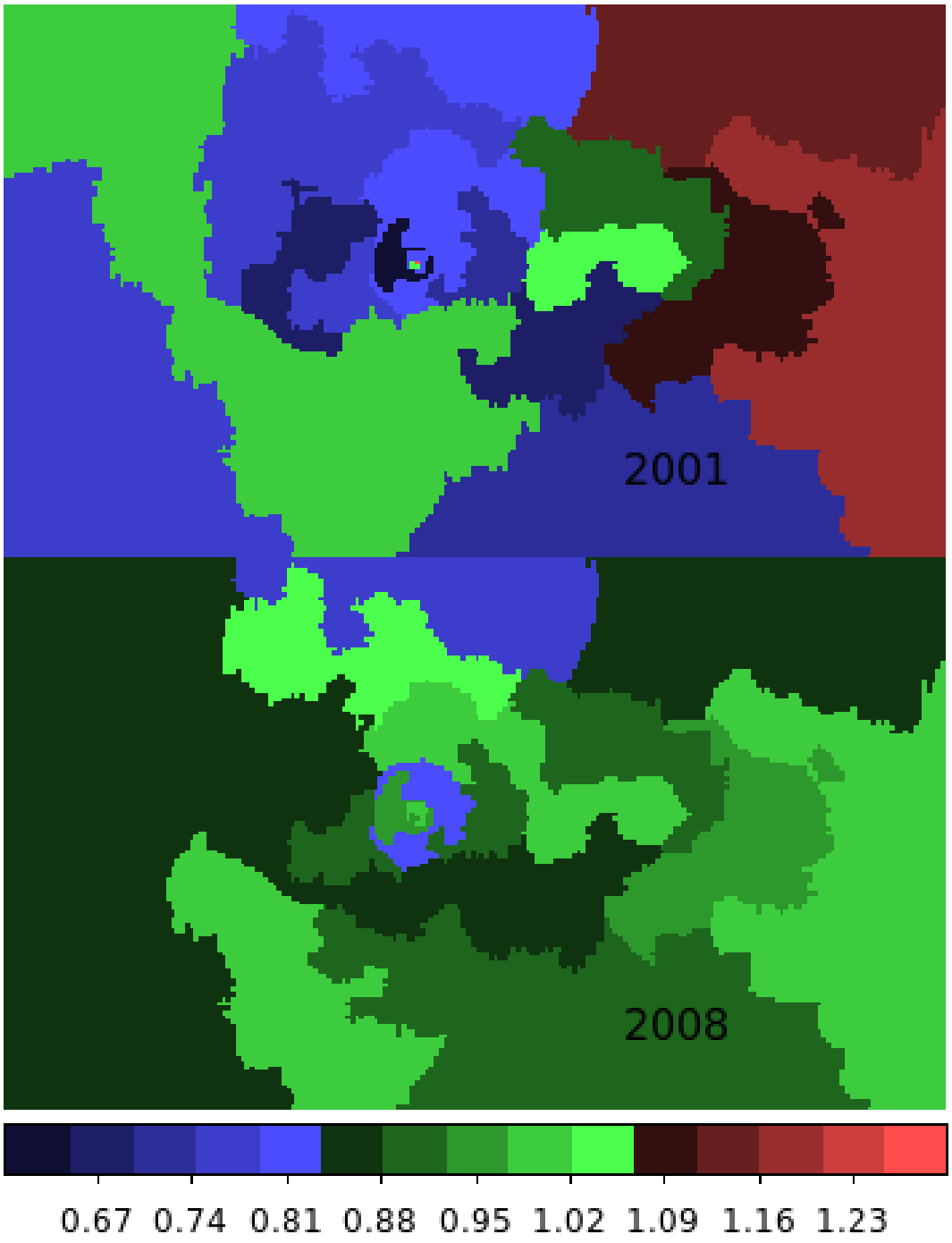

Figure 8.15: Reduced chi-squared values of the fits shown in Figure 8.13.

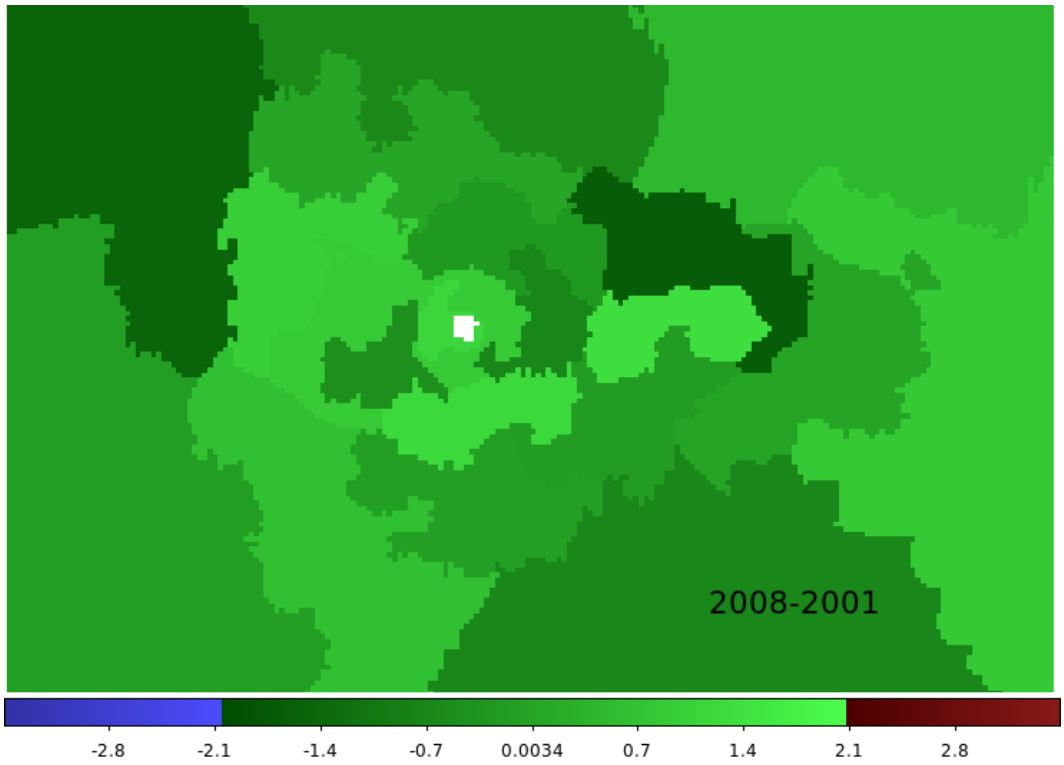

Figure 8.16: G54.1+0.3 Significance map. We find no significant differences and attribute this to the large errors associated with the brief 2001 observation.

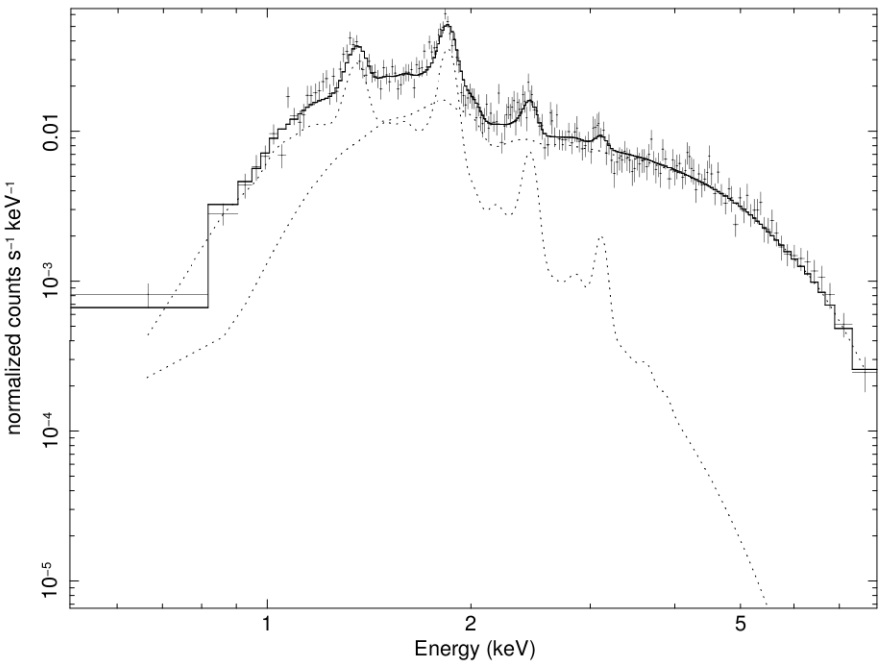

Figure 8.17: G11.2–0.3 sample spectrum of one of the selected regions displayed with the best fit (solid line) thermal (VPSHOCK) plus non-thermal (Power-law) model. The dotted line shows the components of the model spectrum fitted to the data.

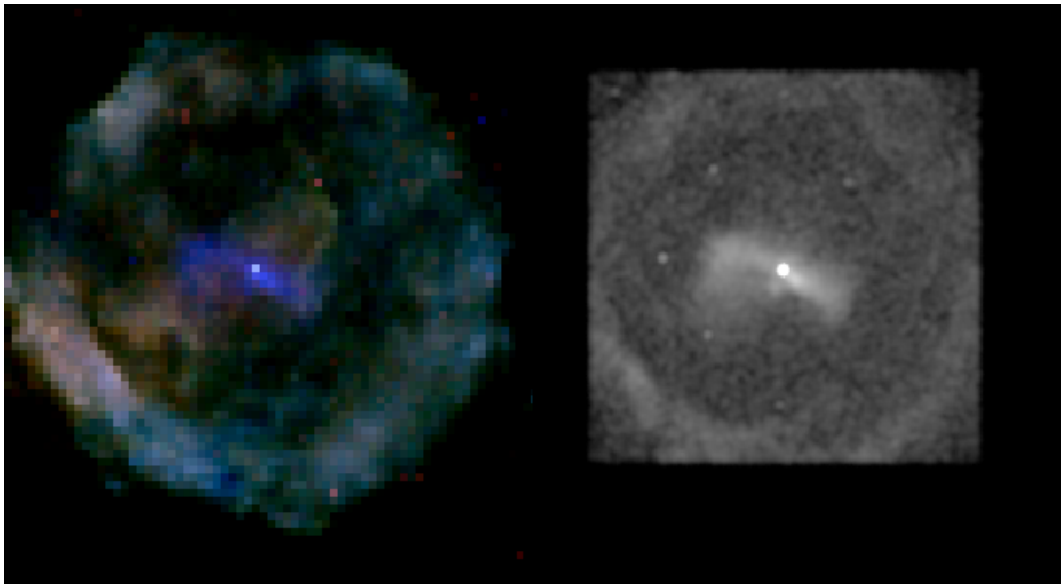

Figure 8.18: Left: RGB *Chandra* Image of G11.2–0.3 with colours defined as 0.5–1.2 keV: red, 1.2–2 keV: green, and 2–7 keV: blue. Right: Filtered 3.5–8 keV image used for spectral map region generation.

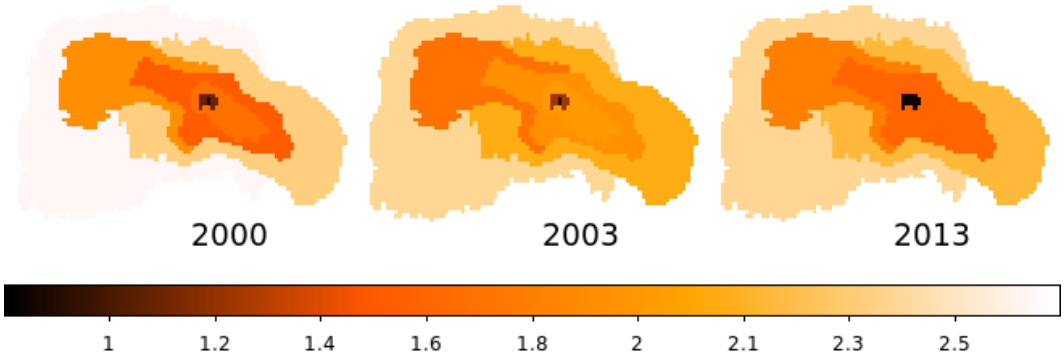

Figure 8.19: Maps of the photon index values in the PWN of G11.2-0.3

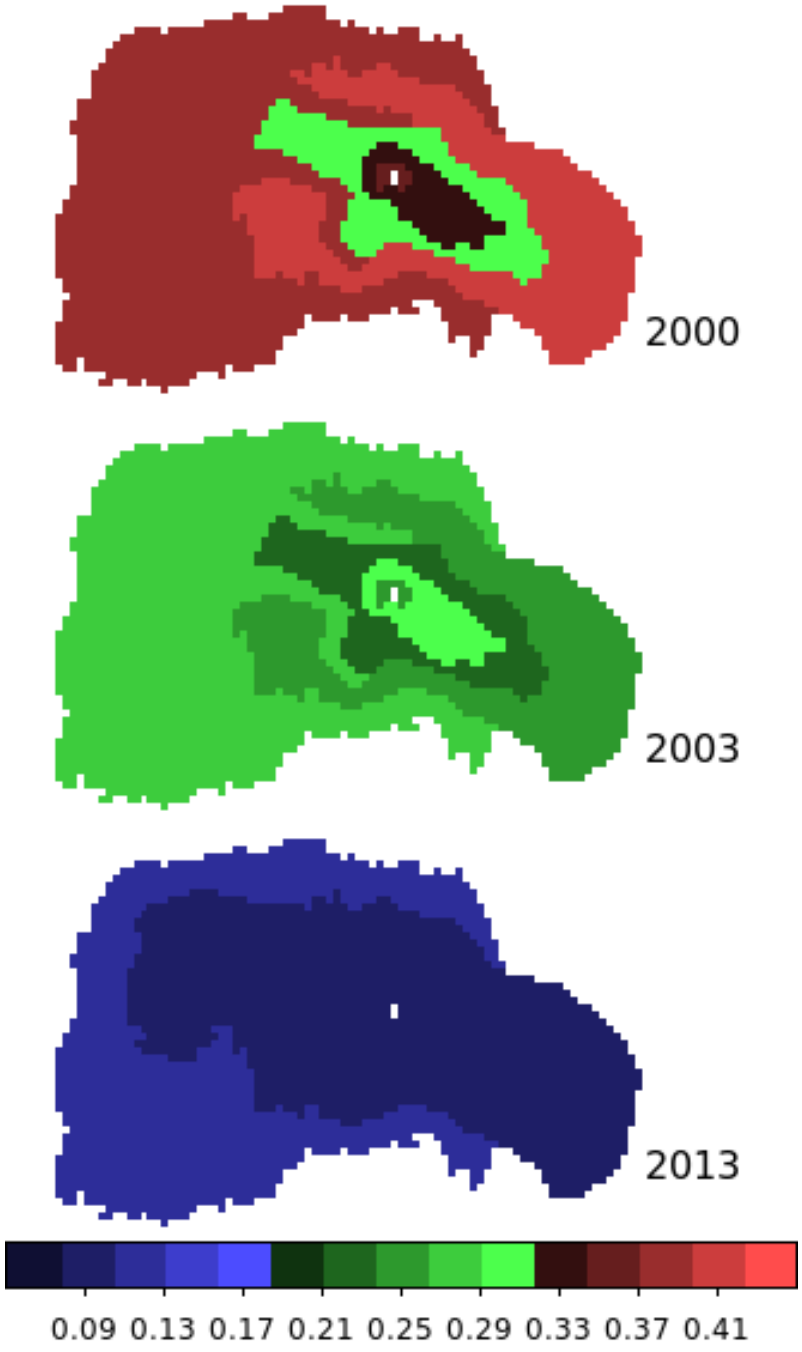

Figure 8.20: $1-\sigma$ error values of the photon index associated with the fits shown in Figure 8.19.

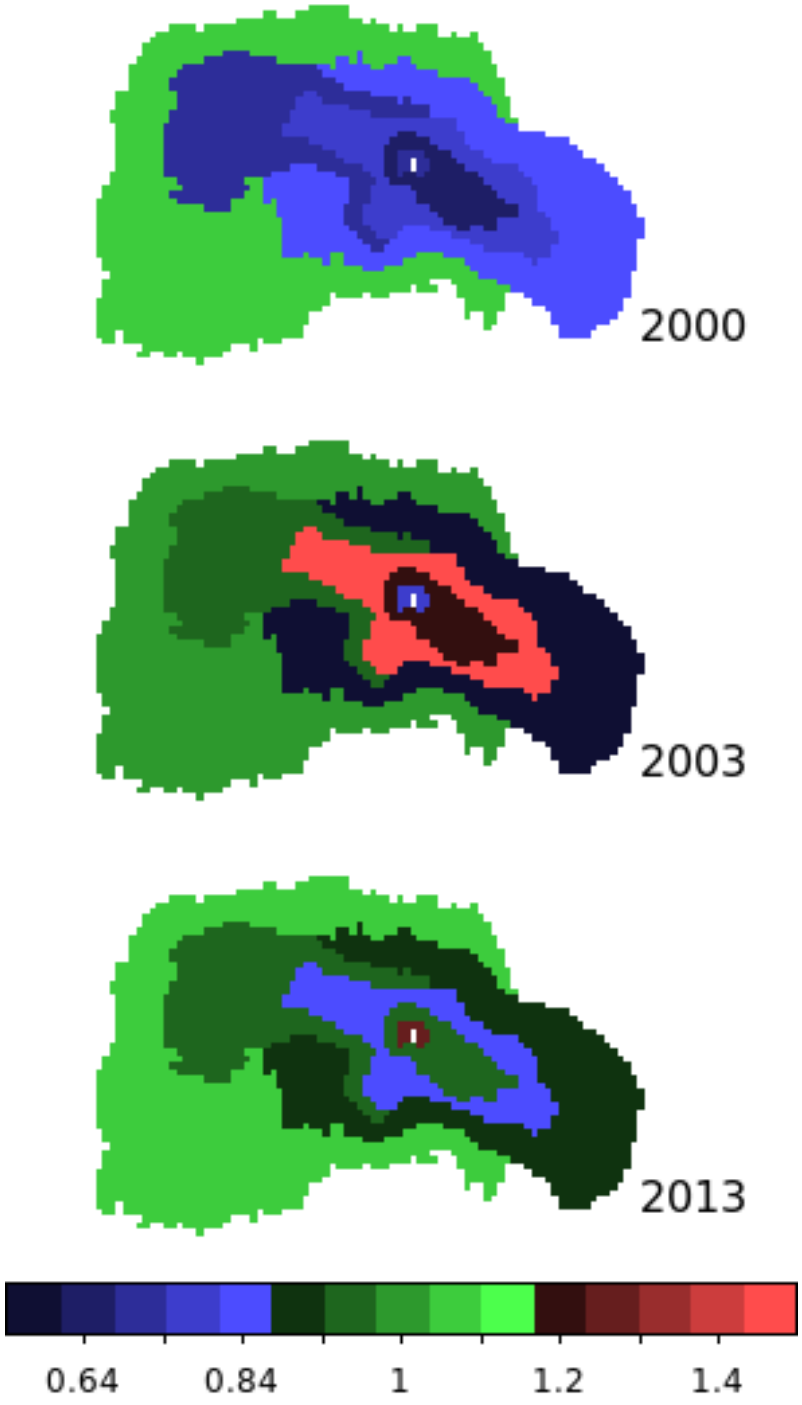

Figure 8.21: Reduced chi-squared values of the fits shown in Figure 8.19.

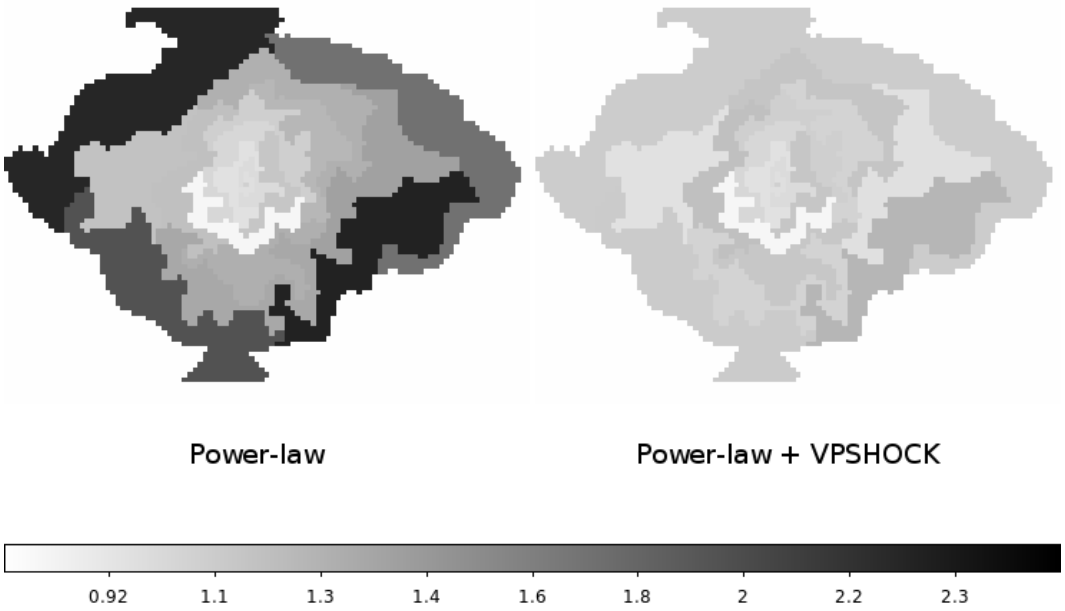

Figure 8.22: 3C 58: Maps of the reduced chi-squared value using an absorbed power-law model (left) and adding a vpshock model where required (right).

we find several regions surrounding the pulsar which have significantly hardened over this period. The component error and reduced chi-squared maps with the added two component model regions are shown in Figures 8.25 and 8.26.

8.3 Discussion

We have presented evidence for variability in several PWNe using the spectral index map technique applied to archival *Chandra* data. In the following, we discuss the effect of any possible instrumental effects on our results, in order to verify that the

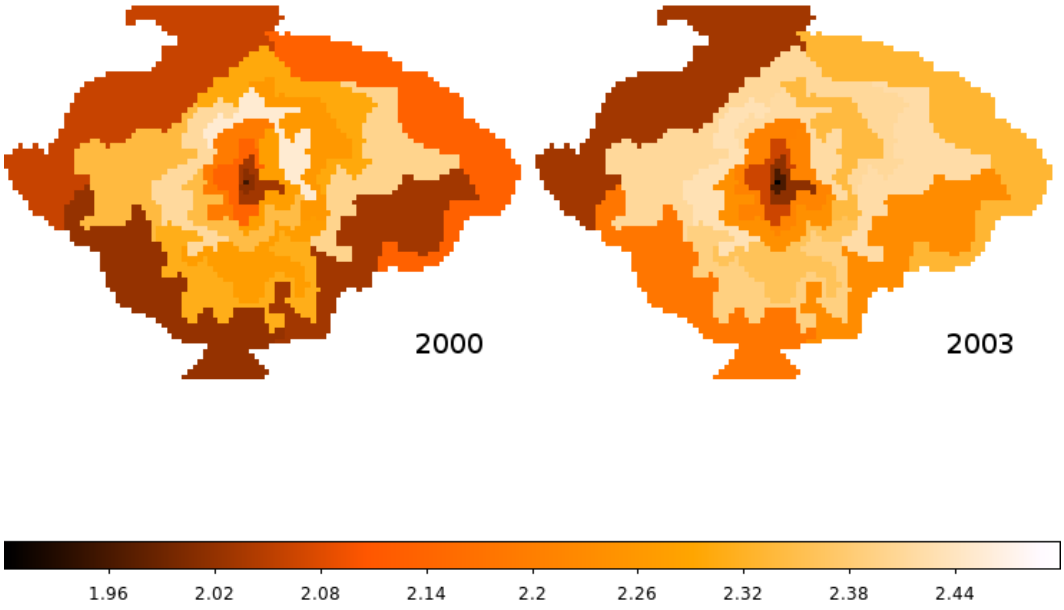

Figure 8.23: Photon index map of 3C 58. The maps are coloured by photon index with darker colours indicating a harder spectrum.

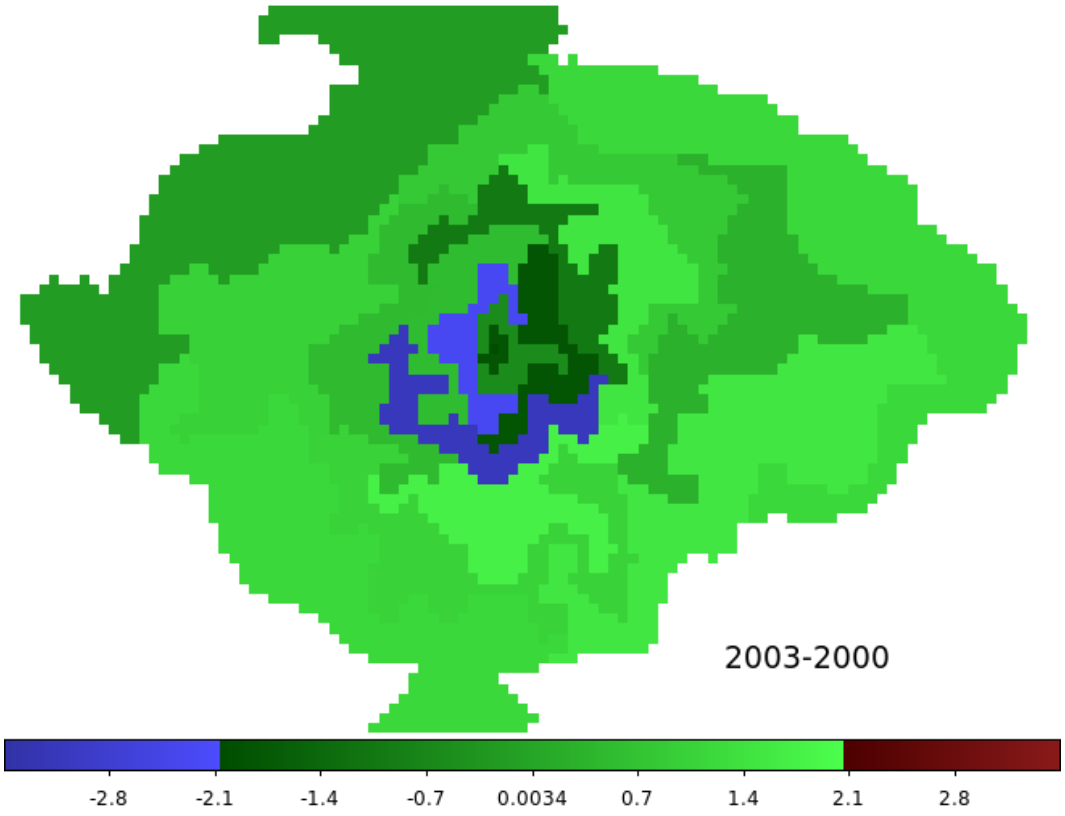

Figure 8.24: Significane map of 3C 58 comparing the 2000 to 2003 observations. Positive (negative) values correspond to softened (hardened) photon index between observations. The region surrounding the central pulsar and jet/torus structure has hardened between the observations.

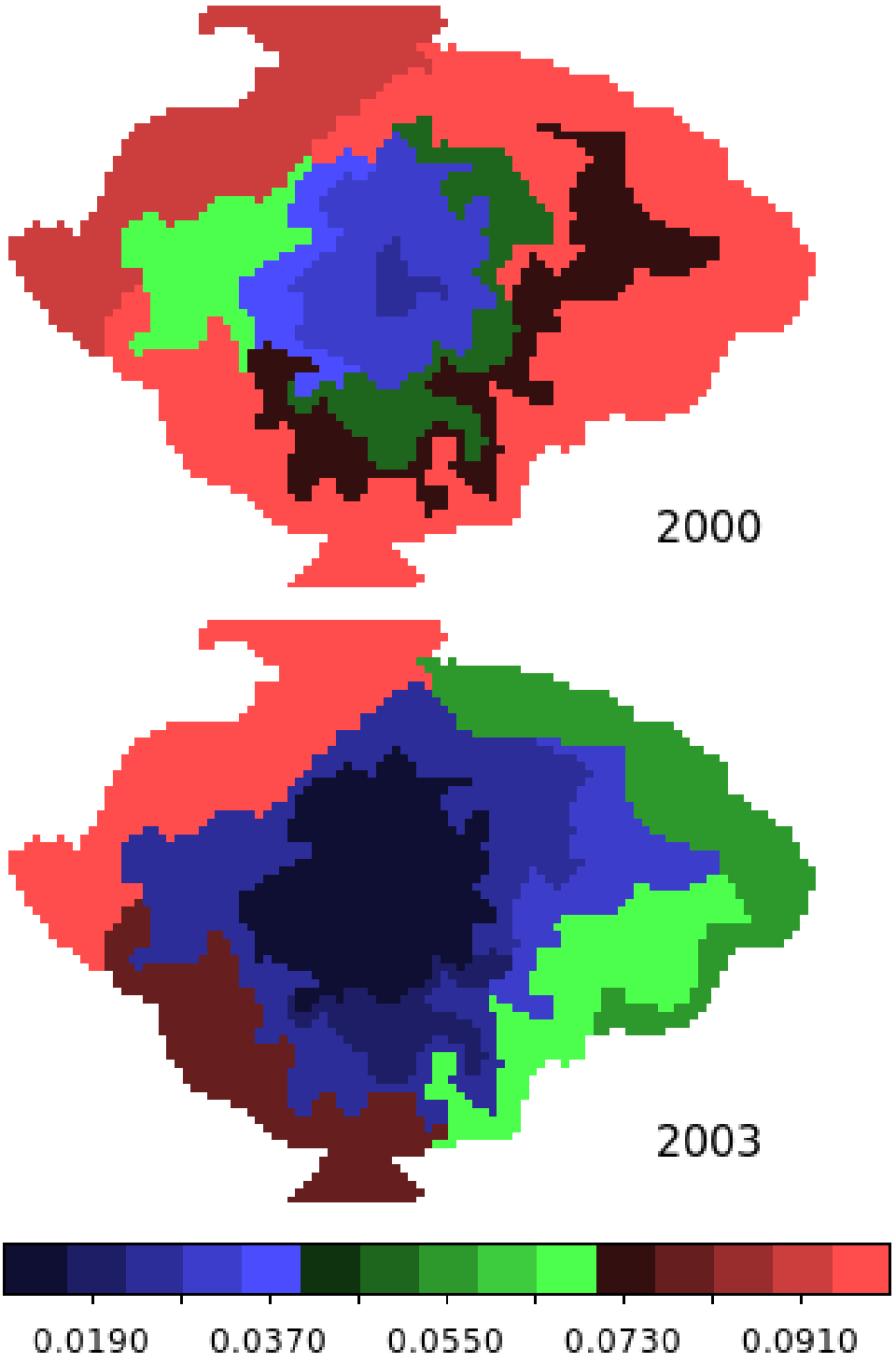

Figure 8.25: $1-\sigma$ error values of the photon index associated with the fits shown in Figure 8.23.

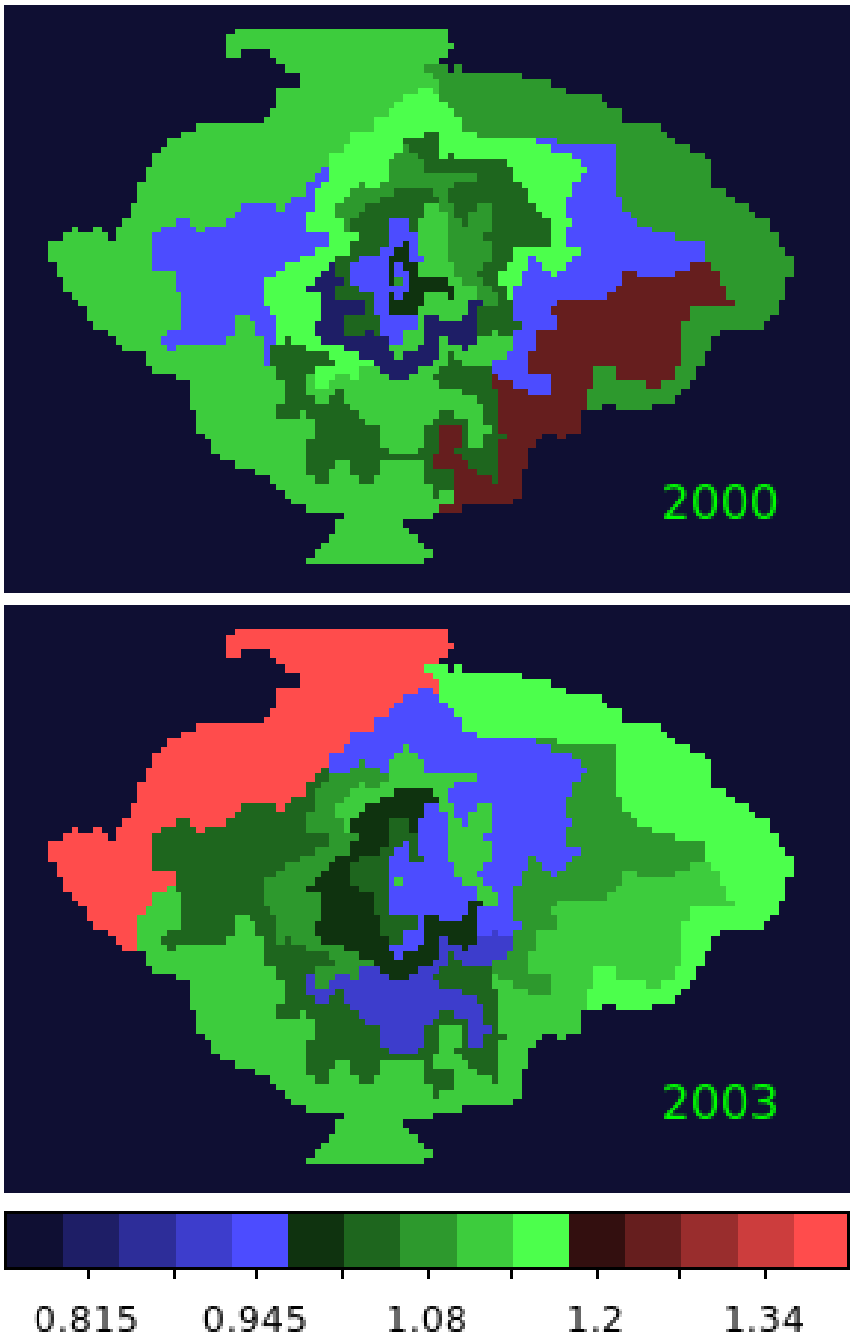

Figure 8.26: Reduced chi-squared values of the fits shown in Figure 8.23.

variability is intrinsic to the sources.

8.3.1 Pileup

Pileup occurs when multiple photons are received within the readout time of the detector. These are indistinguishable from a single photon with the sum of the energy. Of our sources, Kes 75, G11.2–0.3 and G54.1+0.3 each has a pulsar which suffers from pile-up. Methods of correcting for pileup require extracting spectra from a region covering the entire point spread function in order to correct for the effect. Our bins surrounding the point source do not meet this requirement, we therefore leave analysis of the central region to traditional methods and other studies, and focus instead on the extended nebular emission which is not piled up.

8.3.2 Contamination

The response of *Chandra* has changed over its lifetime due to the build up of contaminants (Plucinsky et al., 2018). This is modelled and accounted for by the standard CIAO processing. To further explore whether the time-dependent results we find are intrinsic to the sources, we compare the observations of Kes 75 which span 2000 – 2016 to the results without the contamination correction applied. Kes 75 was chosen for this analysis over G21.5–0.9 which has a similar span of observations, since the contamination correction has been modelled on the emission from the PWN within G21.5–0.9 and therefore is not a suitable candidate for this analysis.

Spectra were extracted from the same regions used to generate the spectral maps shown in section 8.2.3 but without the contamination correction applied. The column

density was fixed to the value used with the standard processing map (the best fit value found from fitting the PWN spectrum). This spectral map was then subtracted from the initial result to look for systematic changes. Figure 8.27 shows the result. The spectra are consistent with small differences well within error ranges for the 2000 observation, however by 2006 the differences are all positive as the uncorrected contamination leads to a harder spectrum. This systematic hardening continues to grow through the 2016 observations.

If we assume the column density is constant, we derive the best fit value from fitting the PWN spectra from each period with a tied column density, while allowing the photon index to vary. These values are listed as the constant values in Table 8.2. Without the contamination correction applied we find a larger value of the column density. The effect of this on the spectral maps is shown in Figure 8.28. The larger absorption value forced by the increasing contamination leads to a softer derived spectral index in the non-corrected 2000 observation (and hence the negative difference value). The 2016 observation shows a consistent positive difference as the increasing contamination artificially hardens the non-corrected observations.

Next we try fitting with different values of the column density. Each value is found from fitting the PWN spectrum processed with the corresponding contamination correction. The data without the correction finds a systematically higher value for the column density (Table 8.2). Comparing photon index values we find no systematic differences (Figure 8.29). The photon index values remain close to those found from the contamination corrected data. The contamination is therefore consistent with an increase in absorption (as expected) and if handled correctly will not affect the

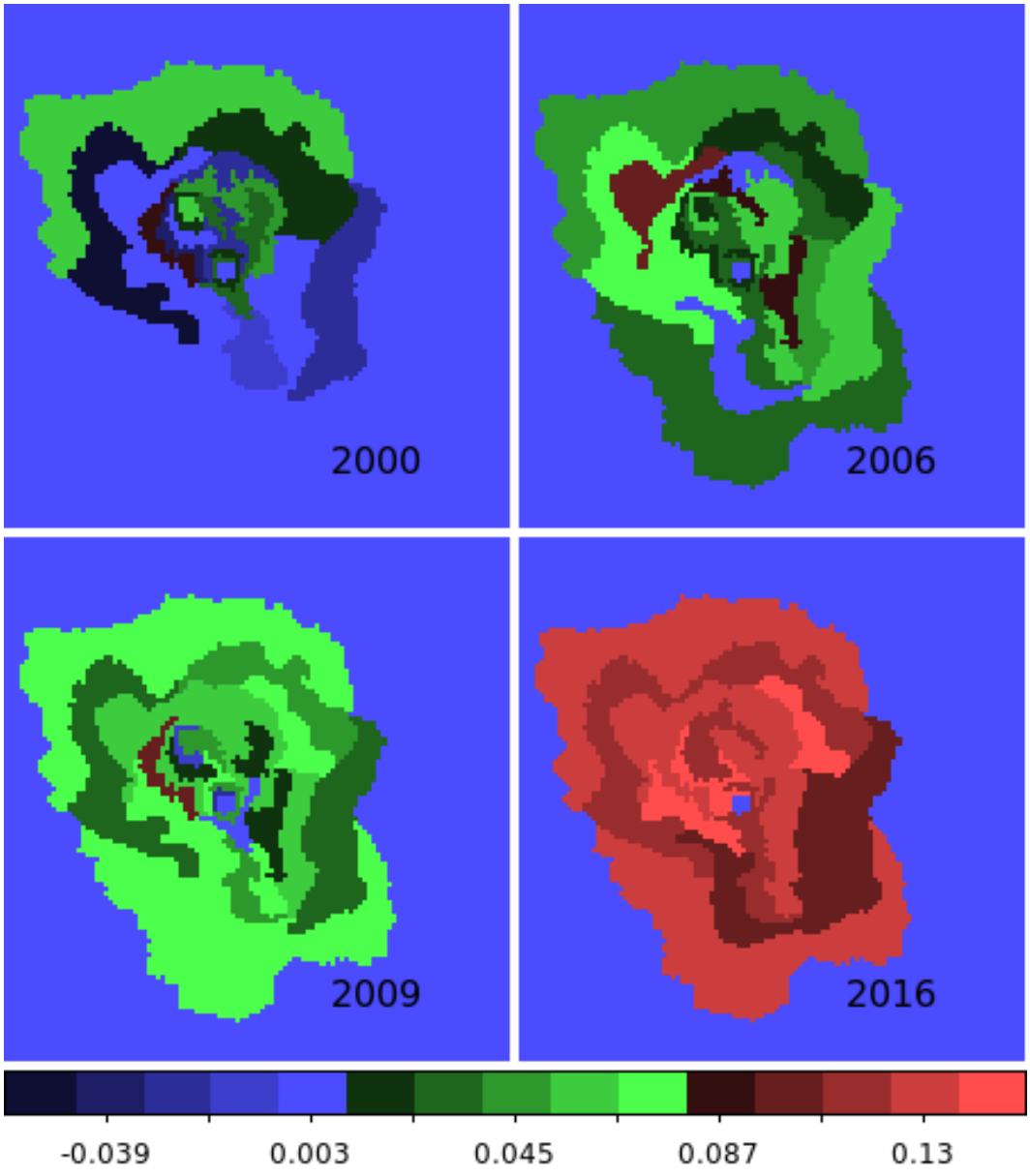

Figure 8.27: Kes 75 difference images calculated from photon index fits from the standard processing including the contamination model subtracted by fits from data without the contamination correction applied. Both fits use the same column density value which was obtained from fitting the PWN spectrum extracted using the standard processing. The early observations are consistent while the later observations have become systematically harder.

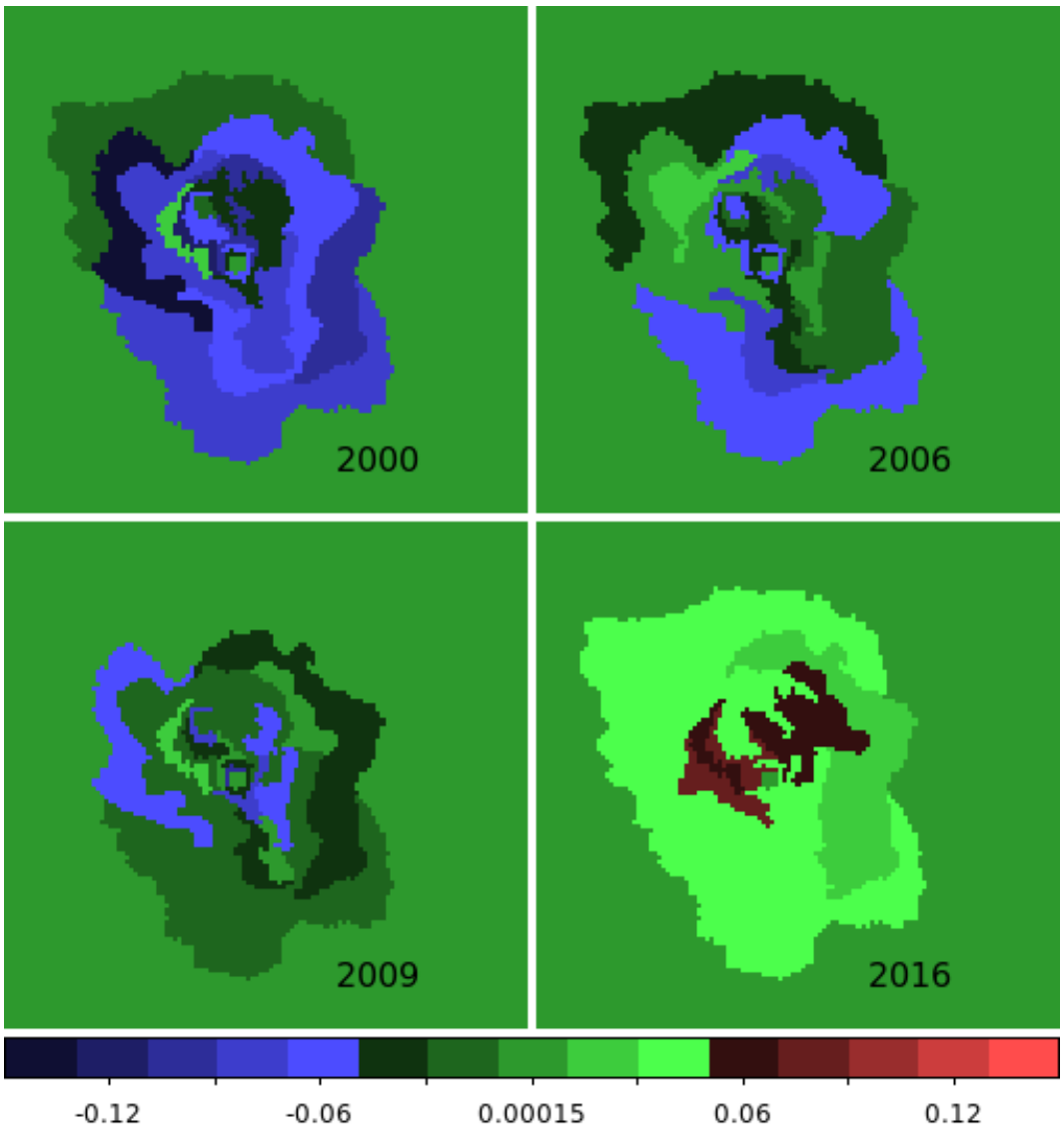

Figure 8.28: Difference images calculated from spectral maps using the constant values of the column density from Table 8.2. The spectral map created from the data without the contamination correction applied was subtracted from the spectral map created using the standard processing.

	Corrected	No Correction
2000	5.08 (4.95–5.22)	5.14 (5.01–5.28)
2006	5.12 (5.06–5.18)	5.27 (5.21–5.33)
2009	5.26 (5.13–5.41)	5.46 (5.32–5.60)
2016	5.32 (5.22–5.44)	5.78 (5.69–5.86)
Constant	5.18 (5.14–5.23)	5.43 (5.38–5.47)

Table 8.2: Values of the column density in units of 10^{22} cm^{-2} for the Kes 75 PWN found from fitting data corrected for the ACIS contamination compared to the data without the correction applied. The constant fit is a simultaneous fit of all the observations assuming a constant column density while allowing the normalization and power-law index to vary between observations.

ability to measure intrinsic changes in a source's photon index.

8.3.3 Instrumental variances

An understandable concern is whether the variability we find is intrinsic to the source or an instrumental variance. To address this, we process two observations taken days apart where we assume no changes should be visible. The observations 6686 and 7338 of Kes 75 from 2006 on June 7th and 9th respectively were used to create individual spectral maps. Looking for differences between the two maps we find no significant changes (see Fig. 8.30).

8.3.4 Analysis Methods

Our analysis introduces several choices which may affect the results. One obvious choice is the signal limit parameter within *Contbin* which alters the number of counts required per region, and therefore defines the resulting region size. The variability we see appears to happen on the scale of a few arcseconds. Increasing the region

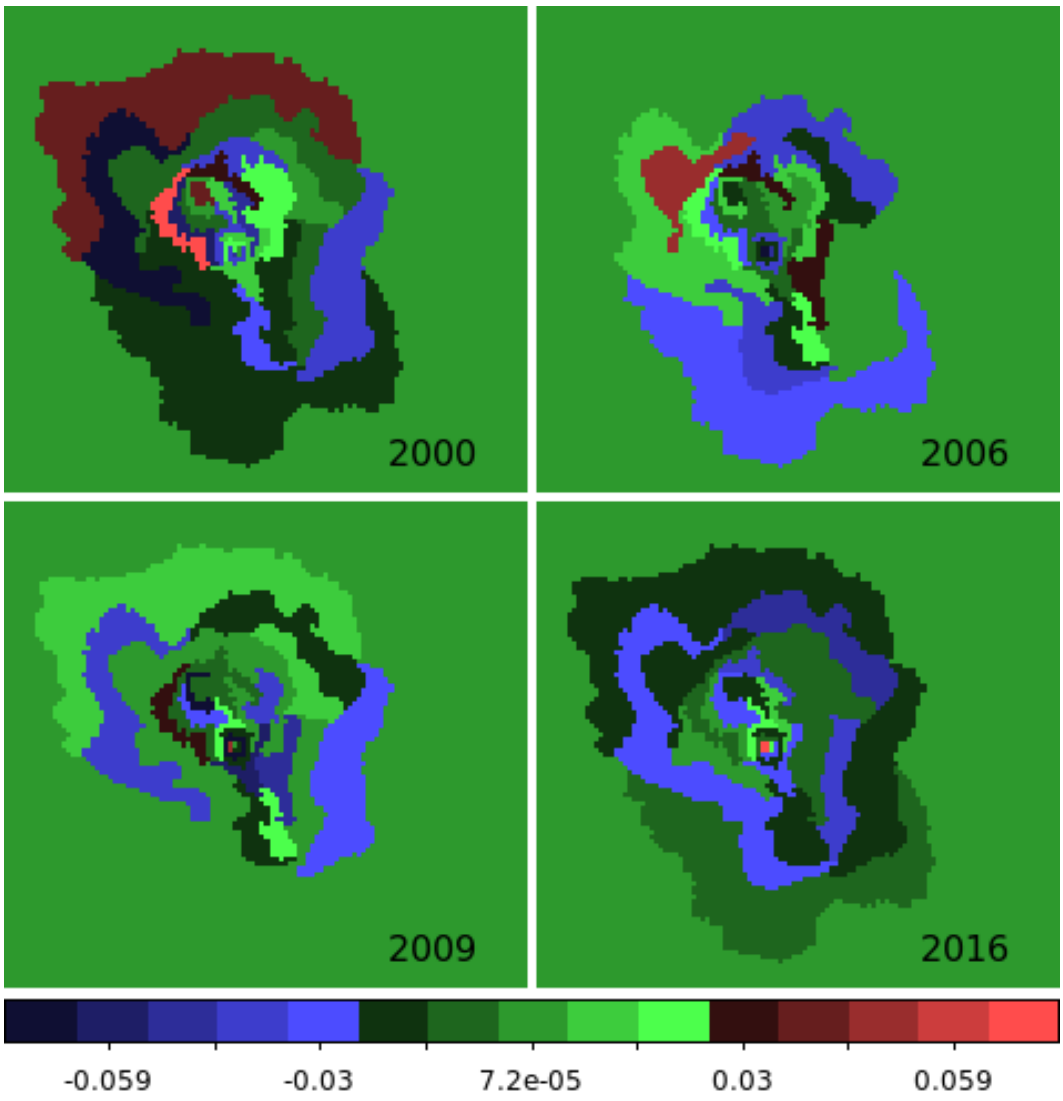

Figure 8.29: Kes 75 difference images calculated from photon index fits from the standard processing including the contamination model subtracted by fits from data without the contamination correction applied. Each fit uses different values of the column density, obtained by fitting the pwn spectrum extracted using the method specific processing method (the values in Table 8.2). The spectra without the contamination correction applied find a systematically higher value for the absorption and the photon index values remain consistent throughout the observation periods.

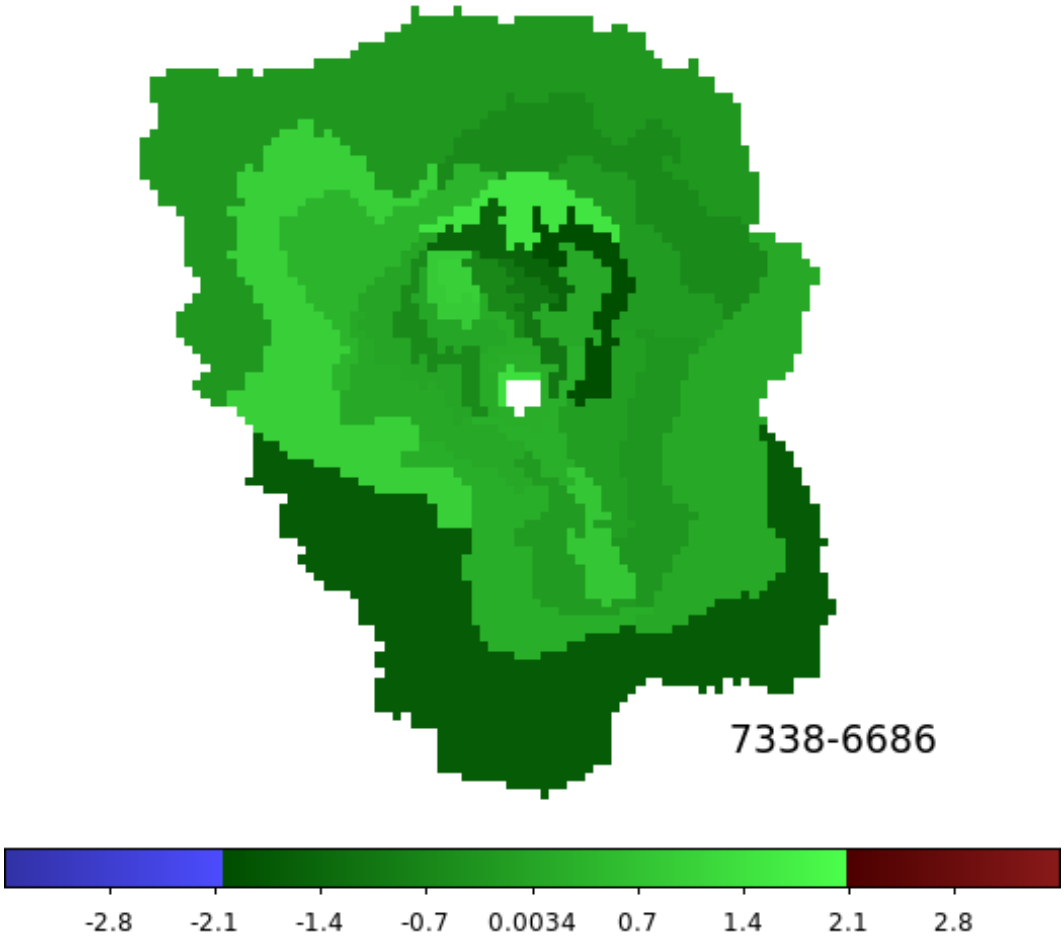

Figure 8.30: Significance image of the differences between the spectral maps of Kes 75 from observations in 2006 on June 7 (Obs id: 6686) and June 9 (Obs id: 7338). No significant differences are found.

size much above this has the effect of smoothing out any variability. When we increase the region size sufficiently we no longer see variability and we return to the previous result of PWNe being remarkably stable on large scales. Optimising the region size to produce the best statistics while retaining evidence of variability is complicated by the entanglement of the typical brightness profile of young PWNe and the *Contbin* algorithm. PWNe are brightest in the centre close to the pulsar and decrease in brightness to the edge of the nebula. As a result *Contbin* generates smaller regions close to the pulsar with regions growing larger with distance. In order to examine the effect of region size and statistics we extract spectra circles of increasing size centred on the region to the north of the pulsar in G21.5-0.9 which showed significant hardening between 2000 and 2005 (Figure 8.5). For each circle size we compare the difference in photon index and its significance between the 2000 and 2005 observations. We find the significance increases to a maximum for a radius of $3''$ and then decreases for larger radii. This roughly matches the size of the *Contbin* region and the number of spectral counts (~ 450) per observation. A second choice is the freezing of the column density parameter across the nebula. We examined the effect of allowing a frozen column density to vary between observations in section 8.3.2 however, another possibility is allowing the parameter to vary over individual regions. While we do not expect the column density to vary significantly over the few tens of arcseconds scale of the remnants we studied, we examine the effect of freeing this parameter in our fits of Kes 75. When we look for significant changes between the 2006 and 2016 observations we lose the significant changes in the southern jet, however the region to the north of the pulsar remains as a region of significant softening. 3C58 is an exception as this remnant spans more than 6

arcminutes along its major axis. We note however that the variability we observe occurs in regions near the pulsar spanning $\sim 1'$. A final choice is our threshold for significance. For the number of regions per remnant we have used, it is reasonable to find one or two regions which meet this limit. The observations we have used are all archived. They were not proposed with the goal of studying spectral changes between small scale unknown features. Our analysis relies on the comparison of two or more observation periods and to constrain the errors to a sufficient level to make a meaningful comparison both observations need to be of sufficient length and quality. However it is worth noting we find similarities between the regions we label as significant and previous variability studies. The plume of variable emission to the north of the pulsar in G21.5–0.9 (Section 8.2.3) appears in the same location as wisp like features seen in brightness images (Matheson & Safi-Harb (2010); Guest et al. (2019)). The jets in Kes 75 where we see changes have been observed to vary in brightness (Reynolds et al. (2018)). With future proposed observations of sufficient depth, higher significance levels of variability will be required.

8.3.5 Alternative binning methods

A previous examination of adaptively binned spectral maps was presented in Kargaltsev et al. (2017). Using a weighted Voronoi tesselations (WVT) method they analyze among others the sample of remnants we have studied here. While they simultaneously fit all available observations of each target, their analysis provides an opportunity to contrast the different binning methods. The regions generated by the WVT method do not follow the surface brightness for thin or elongated features

such as the southern jet in Kes 75 unless the brightness coupled with the length of observation allows for the regions to be smaller than the observed features. For fainter targets with thin features the WVT method does not utilize the imaging resolution of *Chandra*, as the generated regions effectively smooth these features into their surroundings. For the case of Kes 75 this results in an artificial softening of the southern jet. Our spectral map of Kes 75 shows the jet feature in isolation from its surroundings. *CONTBIN* will fail in situations where the spectral index varies dramatically along a thin faint feature. In this scenario the feature will be binned as a single region such that the resulting spectrum will represent a spatially averaged value.

8.4 Conclusions

Spectral maps are a powerful tool which has been under-utilised by the X-ray observing community to study the physics of pulsar wind propagation. We find variability in G21.5–0.9 in the form of hardening and softening of features resembling an outflow from the pulsar, hardening of the region surrounding the pulsar in 3C 58, hardening of the jets post outburst in Kes 75 followed by softening to return to the pre-outburst state. We find marginal evidence of variability in G11.2–0.3 and G54.1+0.3 which require longer observations to confirm. Examining effects such as the contamination build up on the ACIS detector, we find that this should introduce a systematic hardening which can not explain our observations which show both hardening and softening. Similarly, no significant variability is observed between sufficiently long pairs of observations separated by a few days. More and deeper

observations of these and other pulsar wind nebulae are needed to enlarge the sample and improve the statistics. As well, modelling and comparisons with 3D MHD simulations are required to understand the origins of this newly revealed form of variability. This is beyond the scope of this paper and will be the subject of future follow-up work.

Acknowledgements

This research was supported by the Natural Sciences and Engineering Research Council of Canada (NSERC), and made use of the SAO/NASA Astrophysics Data System and the University of Manitoba's High-Energy Catalogue of Supernova Remnants (SNRcat[1], Ferrand & Safi-Harb (2012)). We thank Eric V. Gotthelf and Craig Heinke for comments.

[1]http://snrcat.physics.umanitoba.ca/

Chapter 9

Summary and Future Work

This thesis has presented the results of targeted X-ray observations of PWNe with the goal of identifying the missing thermal emission from the SNR shell, study the transport of the pulsar wind, and examine variability on year to year timescales. Here we summarise our results, and place them in context with the continued work of the community. We acknowledge the importance of the next generation of X-ray observatories and explore exciting opportunities for future work in both observations and simulations.

9.1 G21.5–0.9

G21.5–0.9 is the textbook example of a young composite SNR. The pulsar lies in the centre of a spherical PWN which in turn is surrounded by a faint circular shell. By combining all available *Chandra* observations, we presented the deepest spatially resolved spectroscopic study to date. The emission from the limb-brightened shell segment is found to require a two-component model describing primarily non-thermal

emission with a smaller thermal contribution. We use the results of this fit combined with the imaging analysis to calculate the density of the emitting plasma, the required shock velocity, and resulting kinetic energy. We find a low density indicating the expansion is into a bubble possibly blown by the progenitor. The low temperature of $kT \sim 0.2$ keV may be explained by a non-equilibrium state of the electrons and ions as expected for a dynamically young shock. The derived kinetic energy of 3×10^{49} erg is significantly smaller than the 10^{51} erg canonical supernova energy. Future observations by eg. AXIS (section 9.4.1) with improved sensitivity will constrain the thermal emission from the limb-brightened shell allowing for a better estimate of the explosion energy.

We studied the propagation of the pulsar wind with radial profiles. The spherically symmetric MHD model of KC84 leads to a cutoff radius beyond which a particle of a given energy cannot radiate. This leads to a rapidly rising spectral index which does not match our observations. We fit the radial profile with a diffusion model from Tang & Chevalier (2012). We achieved an adequate fit using a constant magnetic field $B = 130\mu G$ and diffusion coefficient $D = 2.1 \times 10^{27} \mathrm{cm}^2 \mathrm{s}^{-1}$ reflecting spatially averaged values in the nebula.

The component fits of the limb and knot have since been used by the *Hitomi* collaboration (Aharonian et al. (2018); Section 9.4.1) to find a spectral break in the PWN emission. The PWN emission is best described by a broken power-law with indices $\Gamma_1 = 1.74$ and $\Gamma_2 = 2.14$ above and below the break at 7.1 keV. With our radial profile fits (Section 6.3.5), the *Hitomi* collaboration found that the radial softening can not explain the break, and over predicts the emission in the hard X-ray

band. Models for the multi-wavelength emission from radio through γ-ray based on synchrotron cooling and diminishing energy injection from the pulsar are able to fit the radio, infrared, and γ-ray emission, they are unable to fit the break energy and X-ray spectrum. A separate population of radio emitting particles with a different injection source may be required. Such as electrons from the supernova ejecta which have been accelerated by turbulence in the PWN.

The *Hitomi* observation also led to the discovery of narrow absorption lines at 4.2345 keV and 9.296 keV. These are not seen in the *Hitomi* observations of the Crab nebula or other *Hitomi* targets, and were therefore determined to be of astrophysical origin. Cyclotron resonance was ruled out as a potential source as the ratio of energies is not the 1:2 expected from harmonics. Future observations with *XRISM* or *Colibri* (Sections 9.4.1 & 9.4.1) will confirm the existence of these lines and determine their origin. If X-ray pulsations are detected, the phase resolved spectroscopy will also determine the origin of the lines as intrinsic to the pulsar or arising from the surrounding nebula.

9.2 CTB 87

CTB 87 is an evolved PWN without a shell observed at any wavelength. Unlike the symmetric remnant G21.5–0.9 in which the radio and X-ray emission are coincident, the X-ray emission from CTB 87 is offset from the radio and displays a cometary morphology with diffuse emission trailing back towards the radio centre. We presented the results of a deep XMM-Newton observation, finding no evidence of thermal emission from a shell. We constrain the density of the surrounding medium by

placing upper limits on the undetected level of thermal emission. We place a limit of $n \sim 0.05$ cm^{-3}, and favour expansion into a low density bubble. The pulsar has not yet left the nebula to encounter the ISM pressure and density, and the morphology is therefore due to the interaction of the pulsar velocity with a reverse shock.

We presented the first spectral map of CTB 87 and compared with the spectral map predicted from a 2D axisymmetric hydrodynamic numerical simulation based on the parameters from our X-ray analysis. The simulated spectral map reproduces the large scale nested shell-like morphology of softening spectral index with distance from the pulsar and elongation away from the direction of motion. It does not reproduce the extended emission to the south, however this is expected from a simple 2D axisymmetric simulation. Any attempt to replicate this feature would require a full 3D treatment, which evolving to the age of CTB 87 becomes extremely computationally expensive and unfeasible at this time.

9.3 Spectral Maps

Variability in the emission from PWNe has been occasionally seen in the form of brightening during outbursts and the motion of wisp like features. The overall averaged emission profile however remains remarkably stable. PWNe are therefore used as calibration targets for X-ray missions. When dealing with faint features, observations taken many years apart are often merged or fit simultaneously to improve statistics.

Comparing the spectral maps generated from observations taken at various time intervals, we found that they evolve on timescales of less than a year. Spectral maps

of G21.5–0.9 led to the discovery of variability resembling an outflow where a plume of emission to the north of the pulsar develops a harder spectrum before softening again. The corresponding brightness images (Figure 6.12) show wisp like features which appear to move outwards, however they are not localised to the plume and do not show the obvious variability apparent in the spectral maps.

This variability is not unique to G21.5–0.9. We discover similar variability in 3C58 and Kes 75, while the fluctuations detected in G54.1+0.3 and G11.2–0.3 will require further observations to confirm.

We examine instrumental effects such as the contamination build up on *Chandra's* ACIS detector and find this produces systematic variability inconsistent with our results. Comparing observations of Kes 75 taken days apart we find no significant differences in the spectral maps. We therefore identify the evolution of the spectral maps on longer timescales as intrinsic to the PWN emission rather than instrumental or statistical variations.

9.4 Future Work

9.4.1 Observations

The success of the *Chandra X-ray Observatory* and *XMM-Newton* working in tandem has revolutionised the field of X-ray astronomy and PWNe in particular. Both instruments have been pushed to their technical limits over the past 20 years and continue to provide new insight into the field of supernova remnants. The community strives to build on the success of these observatories and the next generation of

detectors have already been launched or are on the way. Here we will highlight a few which have applications to PWNe and SNR science.

Hitomi and XRISM

In February 2016 *Hitomi* was launched, carrying among other instruments a micro-calorimeter to provide high energy resolution soft X-ray observations. Unfortunately, the satellite was lost within 5 weeks during the calibration phase. However, the few observations returned showed the importance of such a device. One of the initial calibration targets observed was G21.5–0.9. While the soft X-ray spectrometer on board *Hitomi* was unable to spatially resolve the different components we fit in Chapter 6, our results were used as an input model to show that an observed spectral break was not due to this radial softening but intrinsic to the particle spectrum (Aharonian et al. (2018)). This observation also hinted at two absorption lines not seen previously. These lines are not found in the observations of the Crab nebula, and therefore can not be simply an instrumental artefact. *XRISM* is a recovery mission which will carry a micro-calorimeter, however it will not have the hard X-ray imaging and soft γ-ray detector capabilities of *Hitomi*. It is a joint NASA/JAXA mission with ESA and CSA participation scheduled to launch in 2022.

Colibri

Colibri[1] is a Canadian proposed X-ray mission. The initial design for a high throughput detector capable of handling count rates up to 10 KHz with individual photon

[1] http://www.colibri-telescope.ca/index.html

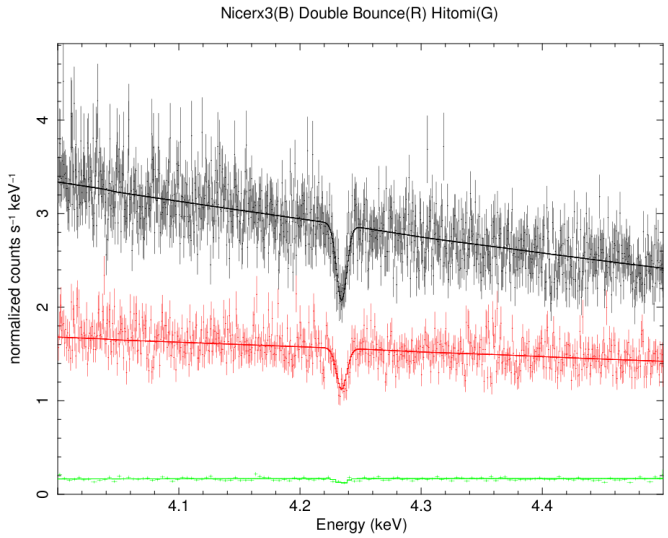

Figure 9.1: Simulation of one of the absorption lines observed from G21.5-0.9 with *Hitomi* (Section 9.1) as they would be seen by a 100 ks observation with two possible *Colibri* configurations (black and red) compared to that observed with *Hitomi* (green).

energy resolution of < 1 eV at 2 keV (Heyl et al. (2019)). With this high throughput, *Colibri* will be able to study emission from the brightest neutron stars without the pileup issues faced by other detectors. The high resolution and sensitive X-ray spectroscopy (Figure 9.1) will provide insight into the radii and equation of state of neutron stars through the Doppler broadening of emission lines from their surface, and ideally provide the ability to study in depth their atmospheric composition.

Athena and AXIS

The Advanced Telescope for High ENergy Astronomy (*Athena*[2]) was selected by ESA within its cosmic visions program for continued development and study as one of the large class mission candidates and would be scheduled for launch in the 2030s. The aim is for $\sim 5''$ pixels with 2.5 eV energy resolution over a field of view of 5 arcminutes, and a 2nd wide field imager with a field of view of 40 arcminutes with < 130 eV energy resolution at 6 keV (Nandra et al. (2013)). The Advanced X-ray Imaging Satellite (*AXIS*[3]) is a proposed NASA probe which aims to be an improved *Chandra* with better imaging resolution ($\sim 0.3''$ and $10\times$ higher count rates with lower detector background (Mushotzky et al. (2019); Safi-Harb et al. (2019)) and would be ideal for furure studies of PWNe.

9.4.2 Data Analysis

Before the arrival of the next generation of X-ray observatories, there is still much to be learned from new and existing *Chandra* and *XMM-Newton* observations. Deep targeted observations of the regions surrounding naked PWNe such as CTB 87 with *XMM-Newton* may reveal the missing shells. The variability we find in PWNe from comparing archived observations of selected remnants can be studied in detail with continued observations taken at periodic intervals to study the timescale of the variability. The Crab nebula and RCW 89 are bright PWNe which have a wealth of archived *Chandra* observations ready for analysis, while other PWNe such as CTB 80

[2] https://www.the-athena-x-ray-observatory.eu/
[3] http://axis.astro.umd.edu/

have only been observed once and another observation will allow the study of long term variability.

The improved collecting area of the next generation of X-ray observatories would be a leap forward in itself, coupled with the high energy and spatial resolution capabilities this will allow deeper searches for missing shells in less observing time, and resolve fine structures in PWN morphology. The large collecting area will mean better statistics allowing for spectral maps with smaller binned regions to achieve the previous signal to noise. This may reveal details on the formation of wisp like features, the role of magnetic reconnection in pulsar winds, and the nature of spectral index variability.

9.4.3 Simulations

Only recently have 3-D numerical simulations of PWNe become possible (eg. Del Zanna et al. (2018); Porth et al. (2016)). They are computationally expensive and only a few simulations have been run to an evolved state. Comparing similarly binned simulated spectral maps generated for comparable timescales as our observations will provide insight into whether the variability we observe may be generated by turbulent flow in the nebula, if variable injection from the pulsar is required, or an unknown process is responsible.

Chapter 10

Concluding Remarks on the Nature of Pulsar Winds and Their Environment

10.1 Isolated PWNe

We have shown that environment into which a SNR expands has a drastic impact on its appearance and evolution. Low density bubbles blown by the progenitor and nearby stars lead to faint or hidden shells. Deep X-ray observations are required to find the faint thermal emission from young SNRs. This emission may be masked by a more dominant non-thermal component, and the dynamical evolution time depends strongly on the density of the ambient medium. More evolved systems benefit from multi-wavelength observations which may reveal shells which have entered the radiative phase and are no longer visible in X-ray.

10.2 Models of Pulsar Wind Propagation

The angular resolution offered by the *Chandra X-ray Observatory* has revealed fine structure in PWNe only possible to replicate with multi-dimensional MHD models. The emission from the outer nebula can not be explained with the 1-D MHD model of Kennel & Coroniti (1984b) in which all particle paths are equivalent and the spectral index rises rapidly with distance. Higher dimensional MHD models allow for turbulent mixing of particles with different paths and emission history such that the simulated spectral maps closely match observations. Diffusion offers an alternative solution. A 1-D diffusion model is able to adequately fit the emission from the outer regions of a symmetric PWN, however it fails to reproduce the inner structure. We find that a combination of both models is likely required to reproduce all features apparent in PWNe.

10.3 Variability in PWNe

Spatially averaged emission from PWNe is remarkably stable. We have shown that resolved spectral maps, however, reveal significant hidden variability on a year to year timescale. This newly discovered variability opens an additional new avenue for future observations, and simulations to test theories for the transport of the particles and fields comprising PWNe.

Bibliography

Abdo A. A., et al., 2007, ApJ, 658, L33

Abdo A. A., et al., 2010, ApJS, 188, 405

Abdo A. A., et al., 2013, ApJS, 208, 17

Abeysekara A. U., et al., 2018, ApJ, 861, 134

Acero F., et al., 2015, ApJS, 218, 23

Acero F., et al., 2016, ApJS, 224, 8

Ackermann M., et al., 2013, ApJS, 209, 34

Ackermann M., et al., 2016, ApJS, 222, 5

Aharonian F., et al., 2018, PASJ, 70, 38

Ajello M., et al., 2017, ApJS, 232, 18

Aliu E., et al., 2014, ApJ, 788, 78

Amato E., Salvati M., Bandiera R., Pacini F., Woltjer L., 2000, A&A, 359, 1107

Arnaud K. A., 1996, in Jacoby G. H., Barnes J., eds, Astronomical Society of the Pacific Conference Series Vol. 101, Astronomical Data Analysis Software and Systems V. p. 17

Arnaud, K. and Gordon, C. and Dorman, B. 2018, HEASARC Astrophysics Science Division NASA/GSFC, 12.10.1

Arons J., 2012, Space Sci. Rev., 173, 341

Bandiera R., Bocchino F., 2004, Advances in Space Research, 33, 398

Becker R. H., Kundu M. R., 1976, ApJ, 204, 427

Becker R. H., Szymkowiak A. E., 1981, ApJ, 248, L23

Begelman M. C., 1998, ApJ, 493, 291

Bevington P. R., 1969, Data reduction and error analysis for the physical sciences. McGraw-Hill, New York, NY

Bevington P. R., Robinson D. K., 2003, Data reduction and error analysis for the physical sciences; 3rd ed.. McGraw-Hill, New York, NY, https://cds.cern.ch/record/1305448

Bietenholz M. F., Bartel N., 2008, MNRAS, 386, 1411

Bietenholz M. F., Matheson H., Safi-Harb S., Brogan C., Bartel N., 2011, MNRAS, 412, 1221

Blackburn J. K., 1995, in Shaw R. A., Payne H. E., Hayes J. J. E., eds, Astronomical Society of the Pacific Conference Series Vol. 77, Astronomical Data Analysis Software and Systems IV. p. 367

Blondin J. M., Chevalier R. A., Frierson D. M., 2001, ApJ, 563, 806

Blumer H., Safi-Harb S., McLaughlin M. A., 2017, ApJ, 850, L18

Bocchino F., Warwick R. S., Marty P., Lumb D., Becker W., Pigot C., 2001, A&A, 369, 1078

Bocchino F., van der Swaluw E., Chevalier R., Bandiera R., 2005, A&A, 442, 539

Bocchino F., Bandiera R., Gelfand J., 2010, A&A, 520, A71

Borkowski K. J., Lyerly W. J., Reynolds S. P., 2001, ApJ, 548, 820

Borkowski K. J., Reynolds S. P., Roberts M. S. E., 2016, ApJ, 819, 160

Camilo F., Lorimer D. R., Bhat N. D. R., Gotthelf E. V., Halpern J. P., Wang Q. D., Lu F. J., Mirabal N., 2002, ApJ, 574, L71

Camilo F., Ransom S. M., Gaensler B. M., Slane P. O., Lorimer D. R., Reynolds J., Manchester R. N., Murray S. S., 2006, ApJ, 637, 456

Camus N. F., Komissarov S. S., Bucciantini N., Hughes P. A., 2009, MNRAS, 400, 1241

Chandra IPI Teams 2018, The Chandra Proposers' Observatory Guide. Chandra X-ray Center, `http://cxc.harvard.edu/proposer/POG/html/index.html`

Chevalier R. A., Gull T. R., 1975, ApJ, 200, 399

DeLaney T., Gaensler B. M., Arons J., Pivovaroff M. J., 2006, ApJ, 640, 929

Del Zanna L., Olmi B., 2017, in Torres D. F., ed., Astrophysics and Space Science Library, Vol. 446, Modelling Pulsar Wind Nebulae. Springer, p. 215

Del Zanna L., Amato E., Bucciantini N., 2004, A&A, 421, 1063

Del Zanna L., Volpi D., Amato E., Bucciantini N., 2006, A&A, 453, 621

Del Zanna L., Pili A. G., Olmi B., Bucciantini N., Amato E., 2018, Plasma Physics and Controlled Fusion, 60, 014027

Dogel' B. A., Ilyasov Y. P., Kaidanovskii N. L., Kokurin Y. L., Kuz'min A. D., Salomonovich A. E., Sorochenko R. L., Udal'tsov V. A., 2012, Radio Astronomy Studies at the Lebedev Physical Institute. Springer Netherlands, Dordrecht, pp 1–60, doi:10.1007/978-94-007-2834-9˙1, https://doi.org/10.1007/978-94-007-2834-9_1

ESA: XMM-Newton SOC 2019, XMM-Newton Users Handbook. XMM-Newton SOC, https://xmm-tools.cosmos.esa.int/external/xmm_user_support/documentation/uhb/

Elwood B. D., Murphy J. W., Diaz M., 2017, preprint, (arXiv:1701.07057)

Ferdman R. D., Archibald R. F., Gourgouliatos K. N., Kaspi V. M., 2018, ApJ, 852, 123

Ferrand G., Safi-Harb S., 2012, Advances in Space Research, 49, 1313

Fruscione A., et al., 2006, in Proc. SPIE. p. 62701V, doi:10.1117/12.671760

Furst E., Handa T., Morita K., Reich P., Reich W., Sofue Y., 1988, PASJ, 40, 347

Gaensler B. M., Slane P. O., 2006, ARA&A, 44, 17

Gavriil F. P., Gonzalez M. E., Gotthelf E. V., Kaspi V. M., Livingstone M. A., Woods P. M., 2008, Science, 319, 1802

Gelfand J. D., Slane P. O., Temim T., 2014, Astronomische Nachrichten, 335, 318

Goldreich P., Julian W. H., 1969, ApJ, 157, 869

Gotthelf E. V., Vasisht G., Boylan-Kolchin M., Torii K., 2000, ApJ, 542, L37

Gotthelf E. V., Helfand D. J., Newburgh L., 2007, ApJ, 654, 267

Gratton L., 1972, Ap&SS, 16, 81

Green D. A., 2014, Bulletin of the Astronomical Society of India, 42, 47

Guest B. T., Safi-Harb S., Tang X., 2019, MNRAS, 482, 1031

Gupta Y., Mitra D., Green D. A., Acharyya A., 2005, Current Science, 89, 853

Helfand D. J., Collins B. F., Gotthelf E. V., 2003, ApJ, 582, 783

Hester J. J., 2008, ARA&A, 46, 127

Hester J. J., et al., 2002, ApJ, 577, L49

Hewish A., Bell S. J., Pilkington J. D. H., Scott P. F., Collins R. A., 1968, Nature, 217, 709

Heyl J., et al., 2019, BAAS, 51, 491

Hughes J. P., Rakowski C. E., Decourchelle A., 2000, ApJ, 543, L61

Hussein M., Shalchi A., 2014, ApJ, 785, 31

Jackson J. D., 1999, Classical Electrodynamics, 3rd edn. Wiley, New York, NY

Joye W. A., Mandel E., 2003, in Payne H. E., Jedrzejewski R. I., Hook R. N., eds, Astronomical Society of the Pacific Conference Series Vol. 295, Astronomical Data Analysis Software and Systems XII. p. 489

Jun B.-I., 1998, ApJ, 499, 282

Kargaltsev O., Pavlov G. G., 2008, in Bassa C., Wang Z., Cumming A., Kaspi V. M., eds, American Institute of Physics Conference Series Vol. 983, 40 Years of Pulsars: Millisecond Pulsars, Magnetars and More. pp 171–185 (arXiv:0801.2602), doi:10.1063/1.2900138

Kargaltsev O., Klingler N., Chastain S., Pavlov G. G., 2017, in Journal of Physics Conference Series. p. 012050 (arXiv:1711.02656), doi:10.1088/1742-6596/932/1/012050

Kaspi V. M., Roberts M. E., Vasisht G., Gotthelf E. V., Pivovaroff M., Kawai N., 2001, ApJ, 560, 371

Kennel C. F., Coroniti F. V., 1984a, ApJ, 283, 694

Kennel C. F., Coroniti F. V., 1984b, ApJ, 283, 710

Kilpatrick C. D., Bieging J. H., Rieke G. H., 2016, ApJ, 816, 1

Kirk J. G., Lyubarsky Y., Petri J., 2009, in Becker W., ed., Astrophysics and Space Science Library, Vol. 357, Neutron Stars and Pulsars. Springer, p. 421

Kolb C., Blondin J., Slane P., Temim T., 2017, ApJ, 844, 1

Komissarov S. S., Lyubarsky Y. E., 2003, MNRAS, 344, L93

Kothes R., 2013, A&A, 560, A18

Kothes R., 2016, in Supernova Remnants: An Odyssey in Space after Stellar Death. p. 46

Kothes R., Reich W., Foster T., Byun D.-Y., 2003, ApJ, 588, 852

Kumar H. S., Safi-Harb S., 2008, ApJ, 678, L43

Li X.-H., Lu F.-J., Li Z., 2008, ApJ, 682, 1166

Liu Q.-C., Chen Y., Chen B.-Q., Zhou P., Wang X.-T., Su Y., 2018, ApJ, 859, 173

Longair M. S., 2003, Theoretical Concepts in Physics. Cambridge University Press

Longair M. S., 2011, High Energy Astrophysics. Cambridge University Press

Lu F. J., Wang Q. D., Aschenbach B., Durouchoux P., Song L. M., 2002, ApJ, 568, L49

Lu F.-W., Gao Q.-G., Zhu B.-T., Zhang L., 2017, MNRAS, 472, 2926

Marshall H. L., Tennant A., Grant C. E., Hitchcock A. P., O'Dell S. L., Plucinsky P. P., 2004, in Flanagan K. A., Siegmund O. H. W., eds, Proc. SPIEVol. 5165, X-Ray and Gamma-Ray Instrumentation for Astronomy XIII. pp 497–508 (arXiv:astro-ph/0308332), doi:10.1117/12.508310

Marshall F. E., Guillemot L., Harding A. K., Martin P., Smith D. A., 2016, ApJ, 827, L39

Matheson H., Safi-Harb S., 2005, Advances in Space Research, 35, 1099

Matheson H., Safi-Harb S., 2010, ApJ, 724, 572

Matheson H., Safi-Harb S., Kothes R., 2013, ApJ, 774, 33

Mignone A., Bodo G., Massaglia S., Matsakos T., Tesileanu O., Zanni C., Ferrari A., 2007, The Astrophysical Journal Supplement Series, 170, 228

Mignone A., Zanni C., Tzeferacos P., van Straalen B., Colella P., Bodo G., 2012, ApJS, 198, 7

Minter A. H., Camilo F., Ransom S. M., Halpern J. P., Zimmerman N., 2008, ApJ, 676, 1189

Morrison R., McCammon D., 1983, ApJ, 270, 119

Morton T. D., Slane P., Borkowski K. J., Reynolds S. P., Helfand D. J., Gaensler B. M., Hughes J. P., 2007, ApJ, 667, 219

Murray S. S., Slane P. O., Seward F. D., Ransom S. M., Gaensler B. M., 2002, ApJ, 568, 226

Mushotzky R. F., et al., 2019, arXiv e-prints, p. arXiv:1903.04083

Nandra K., et al., 2013, arXiv e-prints, p. arXiv:1306.2307

Ng C.-Y., Slane P. O., Gaensler B. M., Hughes J. P., 2008, ApJ, 686, 508

Nolan P. L., et al., 2012, ApJS, 199, 31

Nomoto K., Sparks W. M., Fesen R. A., Gull T. R., Miyaji S., Sugimoto D., 1982, Nature, 299, 803

Nynka M., et al., 2014, ApJ, 789, 72

Olmi B. & Bucciantini N., 2019, MNRAS, submitted for publication

Olmi B., Del Zanna L., Amato E., Bandiera R., Bucciantini N., 2014, MNRAS, 438, 1518

Olmi B., Del Zanna L., Amato E., Bucciantini N., 2015, MNRAS, 449, 3149

Olmi B., Del Zanna L., Amato E., Bucciantini N., Mignone A., 2016, Journal of Plasma Physics, 82, 635820601

Özel F., Freire P., 2016, ARA&A, 54, 401

Pacholczyk A. G., 1970, Radio astrophysics: Nonthermal processes in galactic and extragalactic sources. Freeman, San Francisco

Pavlov G. G., Kargaltsev O. Y., Sanwal D., Garmire G. P., 2001, ApJ, 554, L189

Pence W. D., Chiappetti L., Page C. G., Shaw R. A., Stobie E., 2010, A&A, 524, A42

Piddington J. H., 1957, Australian Journal of Physics, 10, 530

Plucinsky P. P., Bogdan A., Marshall H. L., Tice N. W., 2018, in Space Telescopes and Instrumentation 2018: Ultraviolet to Gamma Ray. p. 106996B (arXiv:1809.02225), doi:10.1117/12.2312748

Porth O., Komissarov S. S., Keppens R., 2013, MNRAS, 431, L48

Porth O., Komissarov S. S., Keppens R., 2014, MNRAS, 438, 278

Porth O., Vorster M. J., Lyutikov M., Engelbrecht N. E., 2016, MNRAS, 460, 4135

Rees M. J., Gunn J. E., 1974, MNRAS, 167, 1

Reynolds S. P., 2008, ARA&A, 46, 89

Reynolds S. P., Borkowski K. J., Gwynne P. H., 2018, ApJ, 856, 133

Roberts M. S. E., Tam C. R., Kaspi V. M., Lyutikov M., Vasisht G., Pivovaroff M., Gotthelf E. V., Kawai N., 2003, ApJ, 588, 992

Ruderman M. A., Sutherland P. G., 1975, ApJ, 196, 51

Rybicki G. B., Lightman A. P., 1986, Radiative Processes in Astrophysics. Wiley-VCH

Safi-Harb S., 2012, in Aharonian F. A., Hofmann W., Rieger F. M., eds, American Institute of Physics Conference Series Vol. 1505, American Institute of Physics Conference Series. pp 13–20 (arXiv:1210.5406), doi:10.1063/1.4772215

Safi-Harb S., 2016, in Supernova Remnants: An Odyssey in Space after Stellar Death. p. 49

Safi-Harb S., Harrus I. M., Petre R., Pavlov G. G., Koptsevich A. B., Sanwal D., 2001, ApJ, 561, 308

Safi-Harb S., Amato E., Gotthelf E. V., Katsuda S., Sasaki M., Uchiyama Y., Tsuji N., Guest B., 2019, BAAS, 51, 317

Sanders J. S., 2006, MNRAS, 371, 829

Seward F. D., Charles P. A., 2010, Exploring the X-ray Universe. Cambridge University Press

Seward F. D., Tucker W. H., Fesen R. A., 2006, ApJ, 652, 1277

Shalchi A., ed. 2009, Nonlinear Cosmic Ray Diffusion Theories Astrophysics and Space Science Library Vol. 362, doi:10.1007/978-3-642-00309-7.

Shan S. S., Zhu H., Tian W. W., Zhang M. F., Zhang H. Y., Wu D., Yang A. Y., 2018, ApJS, 238, 35

Shklovskii I. S., 1953, Akademiia Nauk SSSR Doklady, 90, 983

Slane P., Chen Y., Schulz N. S., Seward F. D., Hughes J. P., Gaensler B. M., 2000, ApJ, 533, L29

Slane P., Helfand D. J., van der Swaluw E., Murray S. S., 2004, ApJ, 616, 403

Smith R. K., Brickhouse N. S., Liedahl D. A., Raymond J. C., 2001, ApJ, 556, L91

Stephenson F. R., 1971, QJRAS, 12, 10

Sturrock P. A., 1971, ApJ, 164, 529

Sun X. H., Reich P., Reich W., Xiao L., Gao X. Y., Han J. L., 2011, A&A, 536, A83

Tang X., Chevalier R. A., 2012, ApJ, 752, 83

Taylor G., 1950a, Proceedings of the Royal Society of London Series A, 201, 159

Taylor G., 1950b, Proceedings of the Royal Society of London Series A, 201, 175

Taylor A. R., et al., 2003, AJ, 125, 3145

Temim T., Slane P., Reynolds S. P., Raymond J. C., Borkowski K. J., 2010, ApJ, 710, 309

Temim T., Slane P., Kolb C., Blondin J., Hughes J. P., Bucciantini N., 2015, ApJ, 808, 100

Terrier R., Lebrun F., Renaud M., Bykov A., Sturner S., 2004, in Schoenfelder V., Lichti G., Winkler C., eds, ESA Special Publication Vol. 552, 5th INTEGRAL Workshop on the INTEGRAL Universe. p. 501

Tian W. W., Leahy D. A., 2008, MNRAS, 391, L54

Torii K., Tsunemi H., Dotani T., Mitsuda K., 1997, ApJ, 489, L145

Torres D. F., Cillis A., Martín J., de Oña Wilhelmi E., 2014, preprint, (arXiv:1402.5485)

Truelove J. K., McKee C. F., 1999, The Astrophysical Journal Supplement Series, 120, 299

Tsujimoto M., et al., 2011, A&A, 525, A25

Vasisht G., Aoki T., Dotani T., Kulkarni S. R., Nagase F., 1996, ApJ, 456, L59

Verbiest J. P. W., Weisberg J. M., Chael A. A., Lee K. J., Lorimer D. R., 2012, ApJ, 755, 39

Warwick R. S., et al., 2001, A&A, 365, L248

Weiler K. W., Panagia N., 1978, A&A, 70, 419

Weisskopf M. C., et al., 2000, ApJ, 536, L81

Wilms J., Allen A., McCray R., 2000a, ApJ, 542, 914

Wilms J., Allen A., McCray R., 2000b, ApJ, 542, 914

Wilson A. S., 1972, MNRAS, 160, 355

Wilson A. S., Weiler K. W., 1976, A&A, 53, 89

Yang H., Chevalier R. A., 2015, ApJ, 806, 153

Yatsu Y., Asano K., Kawai N., Yano Y., Nakamori T., 2013, ApJ, 773, 25

Younes G., et al., 2016, ApJ, 824, 138

Zajczyk A., et al., 2012, A&A, 542, A12

de Jager O., Djannati-Atai A., 2009, in Becker W., ed., Astrophysics and Space Science Library, Vol. 357, Neutron Stars and Pulsars. Springer, p. 451

de Jager O. C., Ferreira S. E. S., Djannati-Ataï A., 2008, in Aharonian F. A., Hofmann W., Rieger F., eds, American Institute of Physics Conference Series Vol. 1085, American Institute of Physics Conference Series. pp 199–202, doi:10.1063/1.3076638

de Rosa A., Ubertini P., Campana R., Bazzano A., Dean A. J., Bassani L., 2009, MNRAS, 393, 527

van der Swaluw E., Downes T. P., Keegan R., 2004, A&A, 420, 937